

https://dspace.org/

Light scattering by superionic LaF3 and LaF3 (BaF2) compound

Anghel, Catalin Anton Marion

1996
http://hdl.handle.net/10539/22166

Downloaded from a DSpace repository. https://dspace.org/

List of Tables

1.1 Members of tysonite family 8

4.1 Properties of LaF_3 102

4.2 Migration energies 102

4.3 Brillouin tensors for a hexagonal crystal 112

4.4 Rayleigh ratios appropriate to this experiment 112

4.6 Brillouin spectra of LaF_3 (5 mol % BaF_2) 116

4.7 Elastic constant C_{11} for LaF_3 (2.5 mol % BaF_2) 118

4.8 Elastic constant C_{11} for LaF_3 (5 mol % BaF_2) 119

4.9 Typical Raman spectra of pure LaF_3 125

4.10 Simulated Raman spectra for pure LaF_3 126

4.11 Linewidths of the A_{1g} phonon in pure LaF_3 128

4.12 The Raman shifts in pure LaF_3 131

4.13 Typical Raman spectra of LaF_3 (2.5 mol % BaF_2) 132

4.14 Simulated Raman spectra for LaF_3 (2.5 mol % BaF_2) 133

4.15 The Raman shift in LaF_3 (2.5 mol % BaF_2) 134

4.16 Linewidths of the phonon in LaF_3 (2.5 mol % BaF_2) 135

4.17 Results of Raman and Brillouin experiments for pure LaF_3 . . . 137

4.18 Results of Raman and Brillouin experiments for doped LaF_3 . . 138

4.19 FWHM for A_{1g} modes in pure and doped LaF_3 139

3.2 Brillouin scattering arrangement II 61

3.3 Raman scattering arrangement 62

3.4 Laser transition scheme 64

3.5 Multipassing schemes 71

3.6 Burleigh electronically scanning procedure 74

3.7 Jarrell Ash monochromator 78

3.8 Sandercock tandem interferometer 83

3.9 Vacuum optical furnace 86

3.10 Encapsulated crystal 93

3.11 Crystal encapsulation system 93

4.1 Possible LaF_3 hexagonal cells 99

4.2 Simplified structure of LaF_3 100

4.3 Scattering geometries for the LaF_3 samples 111

4.4 Brillouin spectra of LaF_3 (2.5 mol % BaF_2) I 114

4.5 Brillouin spectra of LaF_3 (2.5 mol % BaF_2) II 115

List of Figures

1.1 Schematic light scattering spectra 17

1.2 Survey of the Brillouin results for pure LaF_3 19

1.3 Survey of the Raman results for pure and doped BaF_2 21

1.4 Schematic representation of ionic conductivity 24

1.5 Ionic conductivity of different superionic conductors 25

1.6 Heat capacity measurements for β-PbF_2 and LaF_3 29

2.1 The geometry of a light scattering measurement 37

2.2 Dispersion curves 39

2.3 First-order photon-phonon scattering diagrams. 40

2.4 Coordinate system for a hexagonal crystal 48

3.1 Brillouin scattering arrangement I 60

4.2.1 Structural properties 98

4.2.2 Transport properties 101

4.3 Experimental procedures 105

4.3.1 Crystal preparation 105

4.3.2 Brillouin scattering studies 107

4.3.3 Results and discussion 113

4.3.4 Raman scattering studies 121

4.3.5 Results and discussion 124

4.3.6 Comparison of Brillouin and Raman results 136

5 Conclusions and recommendations **141**

5.1 Conclusions 141

5.2 Recommendations 143

2.4.1 The normal modes and Raman activity 52

2.4.2 Selection rules 53

2.4.3 Raman shift and linewidth 54

3 Experimental apparatus and techniques **58**

3.1 The optical systems 59

3.1.1 The laser 63

3.1.2 Fabry-Perot Interferometer: General characteristics . . . 67

3.1.3 The Raman monochromator 77

3.1.4 Auxiliary optical system 79

3.2 Vacuum optical furnace 85

3.3 Crystal preparation 89

3.4 Experimental procedures 94

4 Thermal disorder in pure and doped LaF_3 **96**

4.1 Introduction 96

4.2 Literature review on LaF_3 97

1.4.3 Ionic conductivity 22

1.4.4 Nuclear magnetic resonance 27

1.4.5 Specific heat 28

1.4.6 Ultrasonics 30

1.4.7 Neutron scattering 31

1.4.8 EXAFS 32

1.5 Motivation for this research 33

2 Theoretical background of light scattering and elasticity 34

2.1 Introduction 34

2.2 Light scattering theory 35

2.3 Brillouin scattering in crystals 42

2.3.1 Theory of elasticity 43

2.3.2 Solutions of Christoffel's equation 46

2.3.3 Brillouin tensors 49

2.4 Raman scattering in crystals 51

Contents

1 Introduction and general survey 1

1.1 Superionic conductors 2

1.2 Types of ionic solids 5

1.3 Theoretical models for superionic conductors 7

1.3.1 Static Equilibrium Simulation 10

1.3.2 The Monte Carlo Method 12

1.3.3 The Molecular Dynamics Method 13

1.3.4 Interionic potentials 14

1.4 Experimental techniques for superionic conductors 15

1.4.1 Brillouin scattering 16

1.4.2 Raman scattering 20

Acknowledgments

I am deeply grateful to my supervisor, Professor J.D. Comins, for his guidance and direction throughout the entire research project. I thank him for the time he has given to reading and discussing drafts of this dissertation. As Head of the Physics Department, I am also grateful to him for the facilities of this department.

I thank Professor M.J.R. Hoch, the former Head of the Physics Department, for his kind help on numerous administrative issues.

I am grateful to Professor P.E. Ngoepe of the University of the North for his help, assistance and useful discussions during this project.

I am also grateful to Professor A.V. Chadwick of the University of Kent (UK) for donating us the doped crystals used in this work.

I thank Professor F.R.L. Schöning for useful discussions regarding crystallography.

I would like to convey my sincere thanks to all the members of our research group. Special thanks go to Dr. P.M. Mjwara for his aid, assistance and helpful discussions. I acknowledge the assistance of Mr. P.R. Stoddart in running the Sandercock tandem-interferometer.

I am also grateful to the following people: Mrs. J.M. Salemi, our x-ray technician; the staff of the Glassblowing Department, Messrs. B.N. Fairbrother and S. Gannon; the staff of the mechanical workshop, Messrs. P.J. van der Schyff, E.M Bergh, H.W Stopforth and T.M. Slattery; the staff of the electrical workshop, Messrs. A. Voorveldt and S. Fripp, who all contributed to practical aspects of the experiments.

I record with appreciation the financial support of the Foundation for Research and Development, Pretoria, through the comprehensive grant of Professor J.D. Comins. I am grateful to the University of the Witwatersrand for the award of a Senior bursary. I am also indebted to the Soros Foundation for a travel grant.

I am much indebted to my wife, Carmen, for her cheerfulness, encouragement and support during the difficult moments of this project.

Abstract

The purpose of this investigation was to study the superionic phase transition in pure and doped LaF_3 crystals.

The superionic transition was studied by Brillouin and Raman scattering techniques. This approach provided an effective means of correlation the change in the elastic constants and the broadening and shifting of Raman bands, thereby enabling an examination of various mechanisms which could lead to generation of disorder.

This work reports the first Brillouin scattering measurements in LaF_3 doped with 2.5 and 5 mol % BaF_2 and first Raman scattering measurements above phase transition in LaF_3 and LaF_3 doped with 2.5 mol % BaF_2.

By studying the change in the phase transition temperatures with increasing BaF_2 dopant concentration, these measurements have added new information about the mechanism of the superionic transition. The combined results of these experiments showed that the superionic phase transition temperature decreases substantially for relatively low concentrations of BaF_2 dopant.

Declaration

I declare that this dissertation is my own, unaided work. It is being submitted for the Degree of Master of Science in the University of the Witwatersrand, Johannesburg. It has not been submitted before for any degree or examination in any other University.

C.A.I. Anghel

5th day of February 1996

Light Scattering by Superionic LaF_3 and LaF_3 (BaF_2) Compounds

Cătălin Anton Ilarion Anghel

Degree awarded with distinction on 22 May 1996

A dissertation submitted to the Faculty of Science, University of the Witwatersrand, Johannesburg, in fulfilment of the requirements for the degree of Master of Science.

Johannesburg 1996

low 1984) codes. Successful defect calculations have been carried out on LaF_3 using these codes by Ngoepe *et al.* (1990) and will be outlined in Chapter 4.

1.3.2 The Monte Carlo Method

The principles of statistical mechanics predict that for a system of N particles in thermal equilibrium at temperature T, the probability of finding the configuration in which the positions are $\vec{r}_1 \ldots \vec{r}_N$ is

$$P(\vec{r}_1, \ldots, \vec{r}_N) = (Q_N N!)^{-1} e^{[-U(\vec{r}_1 \ldots \vec{r}_N)/k_B T]}, \tag{1.3}$$

where U is the potential energy as a function of configuration, Q_N is the configurational partition function and k_B is Boltzman's constant. The Monte Carlo method, as developed by Metropolis *et al.* (1953), provides a means of generating a large sample of configurations in which the frequency of occurrence of the configurations is close to that given in Eq. 1.3 (Wood *et al.* 1976, Valleau 1977). Given this sample, it is then possible to calculate any quantity which can be expressed as an average over positions of the ions. For example, the average spatial distribution of the ions in a fast ion conductor can be estimated by counting the frequency with which the ions occupy various volume elements in the unit cell. The method also yields results for thermodynamic functions such as internal energy, pressure, *etc.* However, dynamical quantities, such as diffusion coefficients, are in principle impossible to obtain, since these characterize the time evolution of the system, which is not describe by

It has been recognized since the early work of Mott and Littleton (1938) that the energy of defects in ionic crystals is dominated by the dielectric response of the lattice to the effective charge on the defect. This means that it is important to take into account the relaxation of the lattice at large distances from the defect. In order to do this, the crystal is divided into two regions: an inner region, which contains the defect itself and a set of its neighbours and an outer region which contains the remaining ions. In the outer region, the response of the lattice is represented by the dielectric polarisation $\vec{P}$, which is approximated by the macroscopic formula

$$\vec{P}(\vec{r}) = \frac{1}{4\pi}\left(1 - \frac{1}{\epsilon_0}\right)\frac{Q\vec{r}}{r^3}, \tag{1.2}$$

where Q is the net electric charge on the defect, ϵ_0 is the dielectric constant and $\vec{r}$ is the displacement from the defect. In the inner region, the configuration of the system is represented explicitly by the positions of the ions. The energy of the system and the forces on the ions for a given configuration are calculated using assumed interionic potentials which act between the ions in the inner region and between these ions and those in the outer region. The ions in the inner region are then relaxed iteratively to the equilibrium configuration, in which the forces are zero. These principles have been employed for calculations of defect formation and migration energies using powerful and general computer programs called HADES (Norgett 1974, Catlow 1980, Catlow and Mackrodt 1982) and CASCADE (Leslie 1983) codes. In addition, calculations of the cohesive properties of perfect lattice structures have been performed using PLUTO (Catlow and Norgett 1978) and METAPOCS (Cat-

study fast ion conductors. The first kind, which consists of static equilibrium simulation, allows one to calculate the energy of given configurations of ions corresponding to states of relaxed mechanical-equilibrium; this approach is mainly useful for treating a perfect lattice containing isolated defects, but, as will be noted below, is often relevant to the study of fast ion conduction. The second approach aims to provide a statistical-mechanical simulation of the material at non-zero, and generally, high temperatures; there are two entirely different techniques here, which are called the Monte Carlo and the molecular dynamics methods. The first of these yields only the probability of finding the system in various configurations, and contains no dynamical information. The molecular dynamics method gives a full representation of time evolution of the system in a state of thermal equilibrium. Being a dynamical method, this kind of simulation has the power to calculate the transport properties which are of central interest in fast ion conduction.

1.3.1 Static Equilibrium Simulation

The aim of static equilibrium simulation is to determine the fully relaxed equilibrium configuration and the associated energy of a defective lattice. This kind of calculation has been performed mainly for isolated point defects or defect clusters (Catlow and Mackrodt 1982), but is readily extended to periodically repeating arrays of defects and to linear or planar defects (Puls and Norgett 1976, Catlow and Mackrodt 1982). The principles of the method will be summarized for the case of an isolated defect.

which the focus is on the movement primarily of one particle (i. e. the defect) or a very few particles (e. g. the interstitials) with associated relaxations and following movements of its immediate neighbours. Which defect movements are likely is then a question of the form of the energy surfaces in the space spanned by the displacement vectors of these atoms involved in the movements. Clearly, movements corresponding to passage over regions of exceptionally high energy will be very infrequent since the necessary fluctuations in energy will be very rare. The dependence of jump rate on energy barrier and temperature as deduced from the application of classical statistical mechanics has the well known Arrhenius form (Vineyard, 1957):

$$w = \nu e^{-g_m/kT}. \tag{1.1}$$

Here g_m is the Gibbs free energy of activation (for conditions of constant T and P), which can be decomposed into entropy and enthalpy terms in the usual way.

Much of solid-state theory is based on the assumption that the ions are regularly arranged in space and that their motions are nearly harmonic. The dramatic break-down of these assumptions in the case of fast ion conductors means that the simple theoretical methods used for describing the thermodynamic, structural and dynamical properties of normal solids are not generally applicable. Because of this, computer simulation is now the preferred method of constructing detailed theoretical models of superionic conductors.

There are two broad kinds of simulation method which have been used to

Compound	a (Å)	c (Å)
LaF_3	7.190	7.367
CeF_3	7.114	7.273
PrF_3	7.061	7.218
NdF_3	7.021	7.196
β -SmF_3	6.956	7.120
β -EuF_3	6.916	7.091
β -HoF_3	6.833	6.984
β -TmF_3	6.763	6.927
AcF_3	7.410	7.550
UF_3	7.181	7.348
NpF_3	7.129	7.288
PuF_3	7.093	7.254
AmF_3	7.068	7.245
$CaThF_6$	6.985	7.189
$SrThF_6$	7.159	7.342
$BaThF_6$	7.429	7.535
$PbThF_6$	7.275	7.410
$SrUF_6$	7.120	7.305
$BaUF_6$	7.403	7.471
$PbUF_6$	7.245	7.352
$BiO_{0.1}F_{2.8}$	7.072	7.323
$CaF_2 \cdot 4YF_3$	6.770	6.980
SmH_3	6.551	6.779
GdH_3	6.460	6.710
TbH_2	6.409	6.658
DyH_3	6.359	6.615
HoH_3	6.308	6.560
ErH_3	6.272	6.526
TmH_3	6.234	6.489
LaH_3	6.163	6.443
YH_3	6.360	6.659

Table 1.1: Members of the tysonite family. a and c represent the lattice parameters (After Mansmann 1965)

Jaroszkiewicz and Strange 1985), this prompting the present work concerned with these type *III* fast-ion conductors. Such materials (pure and doped LaF_3) are discussed in this dissertation. LaF_3 is representative of the ionic trivalent halides with the tysonite structure (trigonal P3c1 class), members of this family being presented in Table 1.1.

1.3 Theoretical models for su rionic conductors

Underlying a great deal of the theory of the defect solid state is the idea that defects, namely vacancies and interstitials, make a sequence of individual thermally activated jumps from one lattice site to another. These jumps are relatively infrequent by the standards of lattice vibration periods and generally involve sufficiently large local fluctuations in energy that successive jumps are dynamically uncorrelated with one another. In kinetic treatments it is generally assumed that vacancies move directly only between neighbouring lattice sites and that interstitials correspondingly jump between neighbouring interstitial sites -though this case may be more complicated for two reasons. One is the occurrence of certain less obvious structures, the second is the operation of "indirect" or "interstitial" modes of displacement in which the interstitial moves by pushing a neighbouring atom off its normal lattice site into another interstitial position and itself taking the site so vacated. By these assumptions the potentially many-particle problem has been reduced to one in

Type *II*: These materials achieve a high conductivity rate in a continuous manner. Their high ionic conductivity is associated with good mechanical properties and their performance is close to that of the best alkaline electrolytes. Na Super Ionic Conductor compounds (NASICON) and β-alumina are representative of this type of fast-ion conductors (Chandra 1981, Collin and Boilot 1989).

Type *III*: These materials are characterized by a diffuse phase transition associated with a gradual increase in the conductivity. The immobile sublattice is the same in the low and high temperature phases and the disordering in the mobile sublattice occurs gradually with increasing temperature. Fluorite structured compounds have a prominent position in this class (Catlow 1989). An anomaly in the specific heat was observed in these compounds (e.g. CaF_2, $SrCl_2$) at the transition temperature T_c, which in these cases is $\approx 0.8 T_M$, where T_M is the melting temperature. This anomaly in the specific heat is associated with the development of limited disorder on the anion sublattice, being a current conclusion that less than 10 % of the sublattice is disordered (Catlow *et al.* 1978, Comins *et al.* 1990) The simplicity of the structure and bonding in fluorites made them ideal systems for fundamental theoretical and experimental studies of superionicity (Lidiard 1974, Hayes 1978, Chadwick 1983, Hutchings 1984, Comins *et al.* 1990).

Fluorides with fluorite structure and tysonite structure (e.g. rare earth fluorides) exhibit relatively high F^- ion conductivities (Vashishta *et al.* 1979). In comparison with the fluorites there have been few studies of ionic transport in the tysonite fluorides (Chadwick *et al.* 1979, Schoonman *et al.* 1980,

1.2 Types of ionic solids

From the crystallographic point of view a perfect crystal of an ionic compound would be an insulator (Lidiard 1957). The presence of defects or disorder is a necessity to sustain significant ionic transport. The two types of defects mostly responsible for ion transport in superionic solids are Schottky and Frenkel defects. In Schottky defects positive and negative ions leave their normal sites to create vacancies and eventually residing at internal or external surfaces while in Frenkel defects an ion moves to an interstitial position leaving a vacancy at its lattice site. Some possible transport mechanisms involving these defects are illustrated by Chadwick (1994).

There are different schemes of classification of superionic conductors based on various theories (Rice and Roth 1972, Chandra 1981, Pardee and Mahan 1975, Boyce and Huberman 1979). The most appropriate classification for the purpose of this work is made according to the nature of the transition to the superionic state (Pardee and Mahan 1975, Boyce and Huberman 1979). Following this scheme, ionic solids are of three types:

Type *I*: These are both cation and anion superionic conductors in which the superionic state is achieved through a first order phase transition of the conductivity. A change in the lattice symmetry occurs at the transition temperature; in addition to the disordering of the mobile ion sublattice, the rearrangement of the immobile ion sublattice is usually present. AgI is the most studied fast-ion conductor in this class (Chandra 1981).

electrolytes need low electronic conductivity to avoid leakage losses. Third, for electrodes for batteries and fuel cells both high electronic conductivity and high ionic conductivity are desirable.

High power density, high energy density and reliability are essential if energy-storage systems involving fast ion conductors are to be competitive. In addition, one also hopes for structural integrity, for low weight, for stable conductivity not limited by degradation, and for immunity to environmental factors like oxygen or water vapour. It is especially useful if the device will operate at room temperature, but will survive heating on charging or discharging.

These general requirements mean that any ionic conductor worth serious consideration should have $\sigma_{ionic} \geq 0.1\Omega^{-1}cm^{-1}$, that is, have a diffusion constant $D \geq 10^{-6}cm^2/sec$, and an activation energy for ion conductivity of 0.1 eV or less. These ideals are rarely met, although there are candidates with properties close enough to justify large technical investments.

In addition to the present applications of solid electrolytes, one of the interesting applications is likely to be concerned with the development of certain circuits or devices which may be used in new kinds of computers such as biocomputers in which ionic transport phenomena will play an important role (Takahashi 1989).

may be regarded as a study of disorder (Catlow 1994).

Although there are materials which show both high electronic and high ionic conductivity simultaneously, the emphasis here will be on materials with negligible electronic conductivity.

Superionic conductors are attracting much attention because of their unique transport properties based on the high mobility of ionic defects and/or on the tolerance of the structure for high levels of disorder, which may be generated both intrinsically, i.e. at high temperatures, or extrinsically, by doping or deviation from stoichiometry.

With regard to the diffusion or conduction behaviour, superionic conductors have some characteristic properties: (1) very high values and a small temperature dependence of the diffusion constant D and the ionic conductivity σ; (2) very small values of D_o and σ_o. This implies small values of the defect formation and migration energies.

Apart from scientific curiosity, three major technical requirements demand materials with high ionic conduction (Hooper 1978). First, there are ion monitors in which the presence of a low concentration of some species is measured electrochemically as a voltage across a suitable electrolyte. The important features are discrimination and low electronic conductivity, to avoid dissipating the potential generated in driving an electronic current. Indeed, for electrochemical monitors there is no need to draw a current at all. Second, high ionic conductivity can be valuable in electrolytes for batteries and fuel cells. These

is the electromagnetic field, essentially because of the long range of electromagnetic interactions which gives rise to a large variety of phenomena (Birnbaum 1985). This is in many cases a severe complication in treating the response of the system, even if linear response theory has been applied in studying both absorption and light scattering equations in the limit of small applied fields. In spite of this, light scattering spectroscopy has been increasingly used in the last fifty years to study the dynamics of dense systems. Phenomenological and microscopic theories have therefore been developed in parallel with the experimental findings, in order to obtain the maximum possible information.

In this chapter a survey of fundamental and applied aspects of the field is presented. The chapter covers the theoretical tools required for the study of superionic conductors as well as a brief description of the experimental techniques needed for analysis, particularly applied to pure and doped LaF_3.

1.1 Superionic conductors

In general, ionic solids have values of the electrical conductivity σ immediately below the melting temperature T_m about four orders of magnitude smaller than in the melt. However, some types of ionic solids have values of σ in the crystalline state comparable with that in the melt and are referred to as superionic (or fast-ion) conductors or solid electrolytes. This high value of σ is a consequence of extensive disorder in a component sublattice of the solid and, looked at from a fundamental point of view, the study of superionic conductors

Chapter 1

Introduction and general survey

The study of defects and disorder in solids is a central top'c in solid state science. Up to now no general theories exist in achieving a satisfactory description of atomic motion in those solids which do not exhibit translational invariance of the microscopic properties. Spectroscopic data are valuable for obtaining a better insight into the problem and a large effort had been made by experimentalists in order to improve the number and the quality of their results.

The difficulties connected with the interpretation of experimental data on disordered solids can be easily understood if one notes that, even in ordered dense many-particle systems, a correct interpretation of the experimental data is sometimes a difficult task. This is particularly true when the external probe

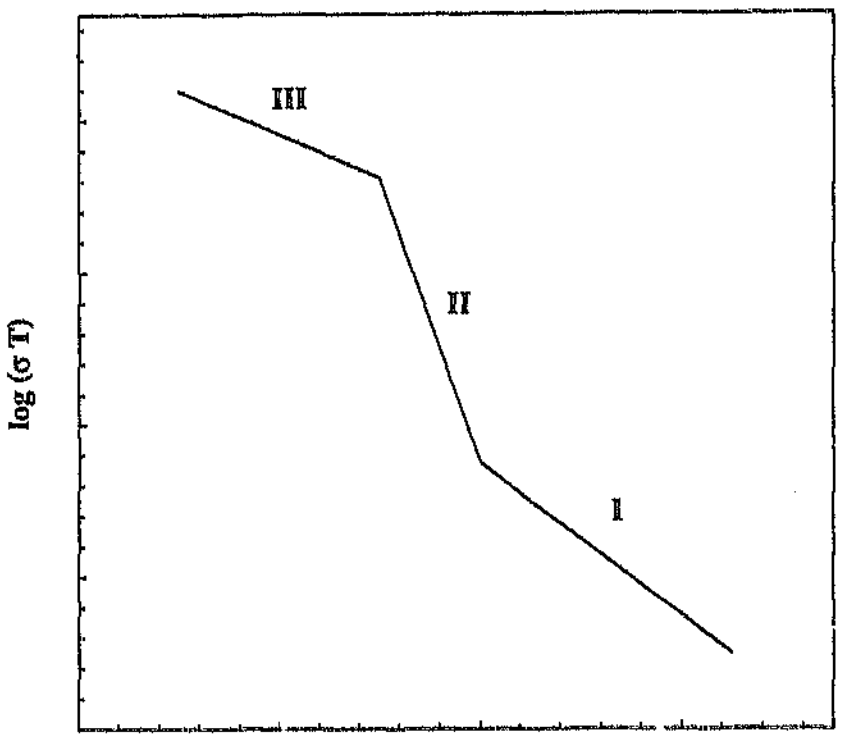

Figure 1.4: Schematic representation of the dependence of ionic conductivity on temperature

characterized by a relatively large value of n ($\gtrsim$ 1 per cent).

Crystals contain defects such as vacancies and interstitials (Section 1.2) and these provide mechanisms for ionic movement. The temperature dependence of the ionic conductivity is given by the Arrhenius relationship:

$$\sigma = (\frac{\sigma_0}{T})e^{-\frac{E_A}{kT}}, \tag{1.7}$$

where E_A is the activation energy and is composed of two parts, E_F determined by the energy of formation of a defect, and E_M, its activation energy for motion. Usually, a plot of $\log \sigma T$ against $\frac{1}{T}$ has three regions with different slopes as schematically shown in Figure 1.4.

At low temperatures, conductivity arises from defects existing in the crystal because of the presence of impurities, so that E_A is determined primarily by the activation energy for motion only (Hayes 1982). Region II is the region of intrinsic conductivity in which σ is dominated by defects created thermally in the lattice and there is a higher activation energy involving both the energy of creation and of motion. Basically, for superionic conductors, region II terminates with a specific heat anomaly associated with the order-disorder transition (Fig. 1.5). Region III then represents a highly-disordered crystalline state with a relatively low E_A, determinated largely by E_M.

For noninteracting defects, the conductivity σ is related to the diffusion coefficient D_σ for the mobile charge-carrying species through the Nernst-Einstein

found activation energies for the motion of the interstitial fluoride ions in BaF_2 doped with LaF_3 in various concentrations.

In the present work the Raman technique has been utilized to characterize the diffuse phase transition in pure LaF_3 and LaF_3 doped with 2.5 mol % BaF_2.

Earlier work of Liarokopis *et al.* (1985) has reported the temperature dependence of peak positions and halfwidths of the first order Raman spectrum of pure LaF_3 up to 800 K. In this project, Raman measurements have been performed to much higher temperatures ($\approx$1400 K) covering the range of the diffuse phase transition in pure and doped LaF_3 for the first time. These results will be outlined in Chapter 4.

1.4.3 Ionic conductivity

Ionic conductivity, σ, in pure and doped LaF_3 has been the subject of much work (Chadwick *et al.* 1979, Schoonman *et al.* 1980, Roos *et al.* 1983, 1984a, 1984b, 1984c).

For a single mobile species, the conductivity, σ, is given by:

$$\sigma = n\mu(Ze), \tag{1.6}$$

where n is the concentration of the mobile species per unit volume, μ is the mobility of the ionic species, and Ze is the ionic charge. Superionics are

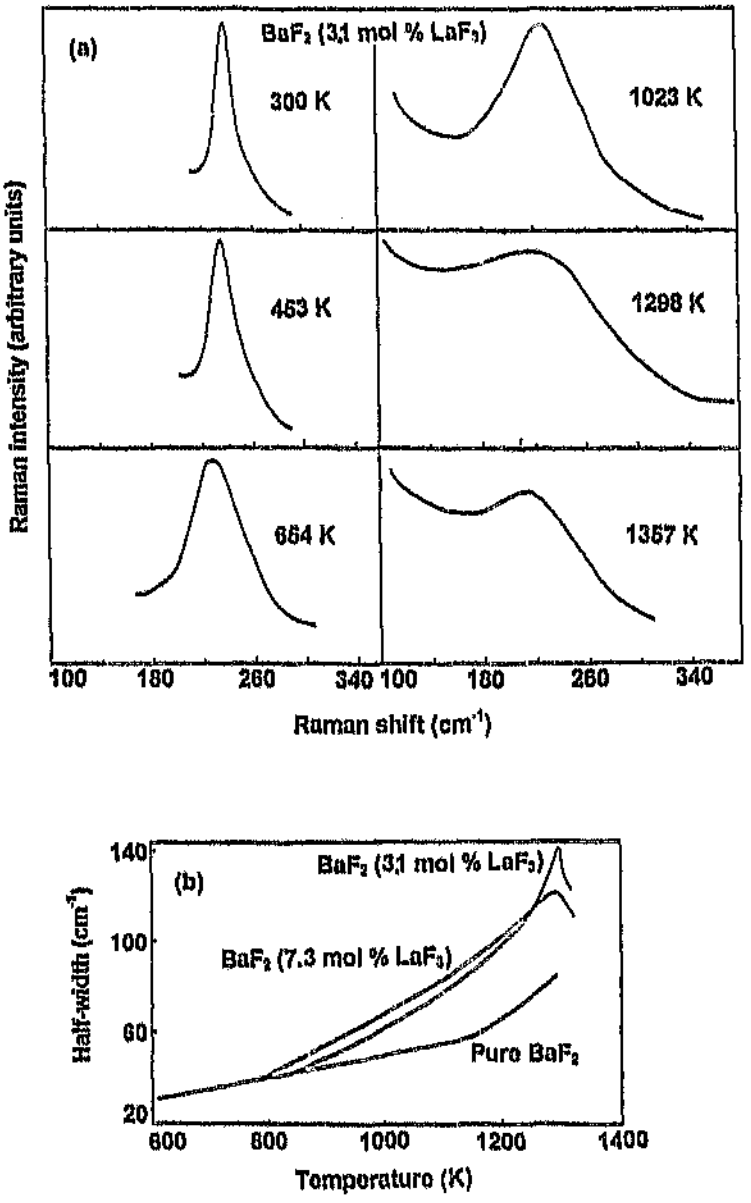

Figure 1.3: (a) Behaviour of the T_{2g} Raman line in BaF_2(3.1 mol % LaF_3). (b) The results for the width of Raman line in pure and doped BaF_2. (After van der Marel and den Hartog 1982)

Brillouin techniques. The theoretical background will be outlined in Chapter 2, and the experimental details will be presented in Chapter 3.

1.4.2 Raman scattering

Raman spectroscopy has widely and frequently been used to investigate structural and diffuse phase transitions in different types of materials. It has proved to be a very useful tool for studying the dynamic properties which occur at phase transitions associated with the anionic or cationic sublattices (Mead and Wilkinson 1977, Habbal *et al.* 1978, Elliot *et al.* 1978, Teeters and Frech 1982, van der Marel and den Hartog 1982, Heyns and de Waal 1992).

Each elementary Raman scattering event involves the destruction of a photon of frequency ω_i, incident from a light source, the creation of a scattered phonon of frequency ω_s, and the creation or destruction of an optical phonon of frequency ω (Fig. 1.1).

The Raman spectrum of a crystal depends on its symmetry as will be presented in Chapter 2. Defects induce modifications of the crystal excitation spectrum and from the removal of the selection rule for crystal momentum conservation allow the direct observation of new modes. Such modes include the broadening of the A_{1g} and E_g peaks in the spectrum of LaF_3 which are associated with anharmonicity and disorder (Giarokapis *et al.* 1985). A similar behaviour is noted for the T_{2g} mode in crystals with fluorite structure. Studying the linewidths of T_{2g} mode (Fig. 1.3), van der Marel and den Hartog (1982) have

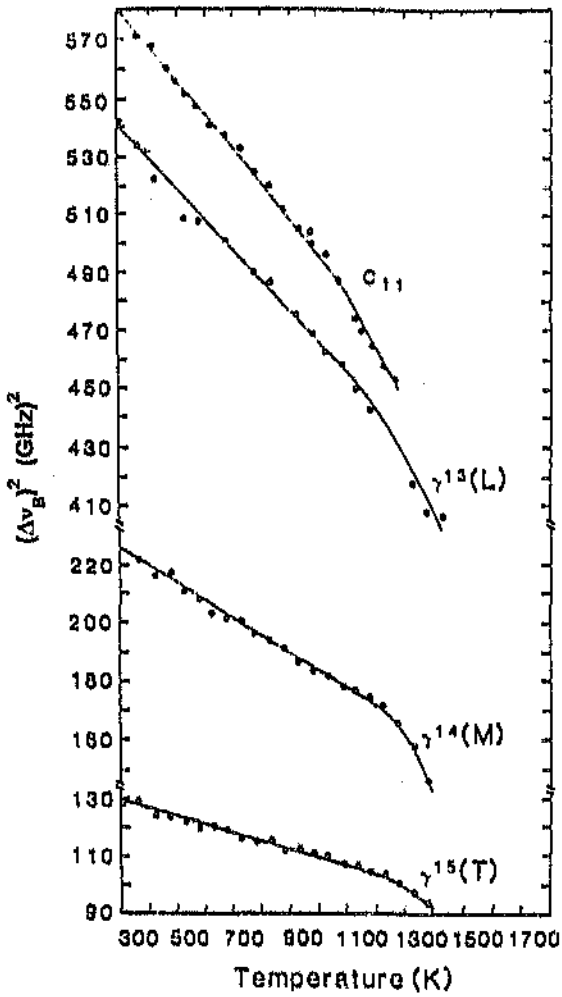

Figure 1.2: The behaviour of different combinations of elastic constants of LaF_3 with temperature (After Ngoepe *et al.* 1986)

does not vary significantly in order to change effectively these frequencies. Botha *et al.* (1993), however, describe an optical interferometry method based on a laser Jamin interferometer for determining the behaviour of the refractive index as a function of temperature. Using an optical flat, the laser beam is split into two parallel beams, one above the other, and directed through an optical furnace which has inside the encapsulated crystal. The crystal is placed in the path of one of two beams. When the two beams are superimposed on a screen, an interference pattern appears. The difference in the optical path depends on the length and the refractive index of the crystal, and so heating of the crystal causes the interference pattern to alter. The lattice parameter is found from classical X-ray measurements.

Much of the effort up to now has related to bulk waves in transparent single crystals. In the context of superionic conductors, Figure 1.2 shows the behaviour of different combinations of elastic constants for LaF_3 with temperature using the Brillouin technique (Ngoepe *et al.* 1986). These kinds of investigations are providing invaluable information on phase transitions and other physical processes in solids.

Increasingly Brillouin scattering is being used to address problems of technological relevance, such as the properties of fast ion conductors (Comins *et al.* 1990), subsurface damage induced by polishing (Mendik *et al.* 1992), the elastic properties of diamond and other thin-film coatings and semiconductor heterostructures (Dil 1982, Nizzoli and Sandercock 1990).

The results reported in Chapter 4 are based on a combination of Raman and

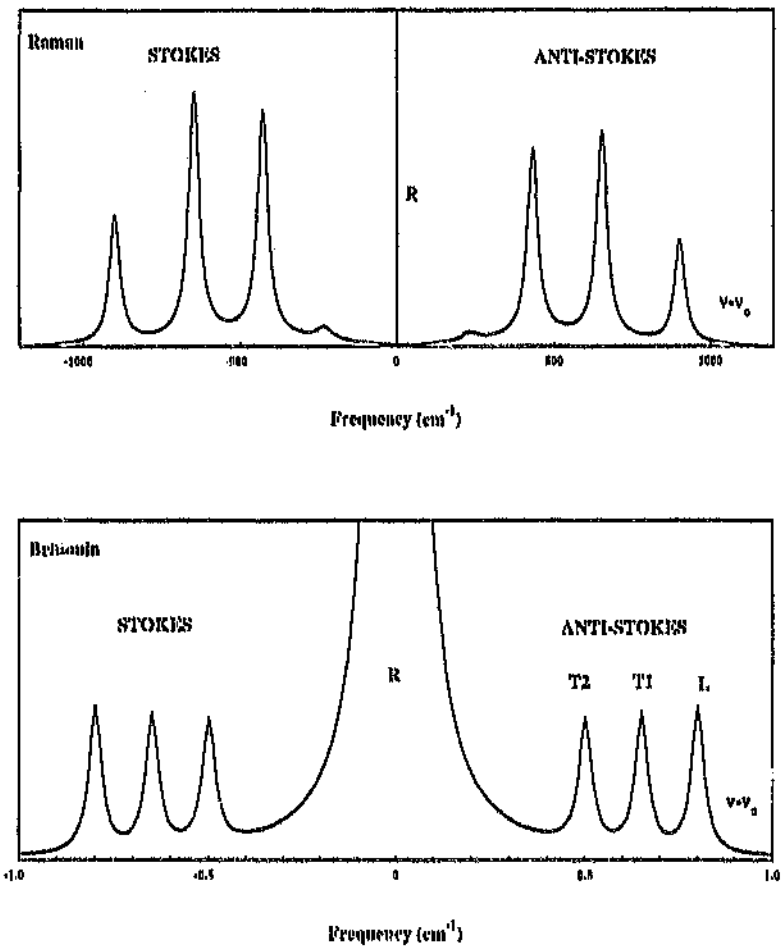

Figure 1.1: Schematic light scattering spectra with 2 stages of resolution: (a) Raman scattering in the 10-1000 cm^{-1} range. (b) Brillouin scattering in the 0.05-1 cm^{-1} range. L, T1 and T2 refer to the longitudinal, first transverse and second transverse peaks associated with Stokes and anti-Stokes events. The elastically scattered (Rayleigh) peak is designated by R.

1.4.1 Brillouin scattering

In Brillouin scattering, light is scattered by thermally excited long wavelength acoustic phonons, and the frequency shift is measured for various scattering geometries to obtain the phase velocity of acoustic waves in different directions. For each scattering geometry, under certain selection rules which will be reviewed in Chapter 2, there are maximum 3 Stokes and 3 anti-Stokes components as shown schematically in Figure 1.1 with frequency shifts (Reissland 1973):

$$\Delta\nu_B = \frac{2nv_n}{\lambda_0}\sin\frac{\theta}{2}, \tag{1.5}$$

where n is the refractive index of the medium, v_n are the three directionally dependent acoustic phase velocities, λ_0 is the wavelength of the incident light, and θ is the scattering angle. These velocities are functions of the bulk elastic constants, and this has led to Brillouin scattering becoming one of the more important methods for measuring the anisotropic elastic constants of crystals (Every 1994).

This method has the advantage that it can be used on specimens of the order of few mm in size or less, under variable conditions of pressure, temperature and magnetic field, *etc.*

According to Eq. 1.5 , it is necessary to know the refractive index and the lattice parameter in order to calculate the elastic constants. Usually, high temperature measurements merely report acoustic-mode frequencies as an approximation to the behaviour of the elastic constants, because the factor ρ/n^2

of the electronic charge clouds and the London dispersion energy. In order to achieve a fully satisfactory description of dielectric properties, it is necessary also to take account of the electronic polarizability of the ions. This is generally done using the shell model of Dick and Overhauser (1958), in which each ion is represented as a charge core and shell coupled by a harmonic spring.

The parameters of the potentials may be obtained either by quantum mechanical calculation (Kim and Gordon 1974, Mackrodt and Steward 1979) or by empirical fitting to bulk crystal properties (Vashishta and Raman 1978), or by a combination of the two (Catlow *et al.* 1977).

While there is no problem in using the full shell-model description in static equilibrium simulations (Catlow and Mackrodt 1982), it demands heavy computational labour in molecular dynamics calculations (Sangster and Dixon 1976), which have almost always been performed using the rigid-ion model.

1.4 Experimental techniques for superionic conductors

Various techniques are employed to study superionic conductors. The important features of the main techniques used in the present project, Brillouin and Raman scattering, will be outlined. This will be followed by a brief review of other methods, which have assisted in interpreting the present results.

that for every time step the force on every ion be calculated by summing the contributions from all the other ions. In the initial period of evolution, the system relaxes to thermal equilibrium. This period is of no use for calculating experimental observables, since it retains memory of the special initial conditions. In addition, it is generally necessary in this phase to add or subtract energy in order to bring the system to the required temperature. Once thermal equilibrium has been established, the system is allowed to evolve undisturbed long enough for a satisfactory quantity of information to be generated: for example if it is wished to calculate a diffusion coefficient, a reasonably large number of elementary diffusive events must be allowed to occur. The position and velocities of all the ions in the course of the simulation are stored for purpose of analysis (Sangster and Dixon 1976).

1.3.4 Interionic potentials

Whatever simulation method is used, the validity of the interionic potential is of crucial importance. Fortunately, a large body of evidence suggests that a rather simple functional form for the potentials is entirely adequate for a wide range of ionic materials (Catlow and Mackrodt 1982). The form commonly assumed for the energy of interaction $V_{\alpha\beta}$ between ions of types α and β consists of three terms:

$$V_{\alpha\beta} = z_\alpha z_\beta \frac{e^2}{r} + A_{\alpha\beta} exp(-\frac{r}{\rho_{\alpha\beta}}) - \frac{C_{\alpha\beta}}{r^6}, \qquad (1.4)$$

which represent respectively the Coulomb energy, the repulsion due to overlap

the probability function P.

1.3.3 The Molecular Dynamics Method

The satisfactory calculation of dynamical quantities demands that the time evolution of the system is simulated. This is what the molecular dynamics method does (Rahman 1964, Erpenbeck *et al.* 1976, Sangster *et al.* 1976) . It is known from Boltzmann's H-theorem that if a many-body system is started in any reasonable initial condition and allowed to evolve freely according to Newton's equations of motion, it will attain the most disordered state characteristic of thermal equilibrium. In this state, it should resemble rather closely, both in its structural and its dynamical properties, the real material studied experimentally, provided only that the forces between the ions are modelled realistically. In practice, there is another proviso, which is that one can handle a large enough number of ions to reproduce the properties of the bulk material.

The course of a molecular dynamics simulation is typically as follows. A certain number of ions (typically a few hundred) is taken in a box in some initial configuration (that of the perfect crystal, for instance) and with random velocities; in order to eliminate surface effects, this basic system is periodically repeated. The system is then made to evolve in time under the action of the assumed interionic potentials. For numerical purposes, the differential equations of motion are approximated by finite difference equations, with some characteristic time step length Δt . The implementation of these equations requires

the incident electric field induces an oscillating dipole of the same frequency at each point along its path. Each oscillating dipole radiates energy in all directions. Thus, the net field at any point in space is the vector sum of the induced dipole fields. In this calculation, the dielectric medium is considered a continuum (Chu, 1974). Classically, each lattice vibration $\{\vec{K}, \omega\}$ perturbs the dielectric constant ϵ so that

$$\epsilon = \epsilon_0 + \sum \epsilon_{K\omega} \exp i(\vec{K} \cdot \vec{r} - \omega t) = \epsilon_0 + \delta\epsilon. \tag{2.1}$$

The scattered electric field $\vec{E}_s$ can be computed by summing the induced dipole fields reaching a particular point in such a way so as to include the relative phase between waves originating from spatially separated points in a scattering volume.

Using this approach, when a field $\vec{E}^i(\vec{r}, t) = \vec{E}^i_0 e^{\vec{k}_i \cdot \vec{r} - \omega_i t}$ (Fig.2.1) is incident on a crystalline medium, the far-field scattered amplitude at a point r' is readily found to be of the form (Cummins, 1969):

$$\vec{E}^i_s = -\frac{\omega_s^{\pm 2}}{4\pi\epsilon r'^3} \frac{E_0 \sin\phi}{R_0} \epsilon^{\pm}_{K\omega} \exp[i(\vec{k}_s^{\pm} \cdot \vec{r}' - \omega_s^{\pm} t)] \int_V \exp[i(\vec{k}_i \pm \vec{K} - \vec{k}_s^{\pm}) \cdot \vec{r}'] dV', \tag{2.2}$$

where

$$\omega_s^{\pm} = \omega_0 \pm \omega_K$$

$$\vec{k}_s^{\pm} = \frac{\omega_s^{\pm}}{c} \hat{s} = \frac{\omega_0 \pm \omega_K}{c} \hat{s}. \tag{2.3}$$

The volume integral in Eq. 2.2 gives a δ-function in $(\vec{k}_i \pm \vec{K} - \vec{k}_s)$ which

and deepened the range of materials properties accessible to measurements by light scattering spectroscopy.

This chapter covers the common ground of Brillouin and Raman scattering. The main goals are to obtain the basic formulas, in order to assist in the interpretation of the results in Chapter 4. Elasticity will also be reviewed in order to explain the Brillouin spectra.

2.2 Light scattering theory

Brillouin and Raman effects involve the inelastic scattering of an incident photon beam with a material so that elementary excitations (phonons, polaritons, plasmons, *etc.*) are created or annihilated, therefore causing a change in the photon frequency.

In superionic conductors, the light is scattered by phonons and this theoretical case will be outlined in the present chapter.

The quantity linking light scattering theory and experiments is the scattering cross section. The magnitude of the scattered intensity is determined by a variety of factors. Only the main results will be quoted, a full account on this subject being the subject of standard texts such as London (1973) and Hayes and London (1978).

When a beam of linearly polarized light is passed through a dielectric medium,

Chapter 2

Theoretical background of light scattering and elasticity

2.1 Introduction

A fundamental problem of solid state physics is to interpret the macroscopic behaviour of crystals in terms of the constants characterising the lattice structure and the mutual interactions between pairs of atoms of the crystal. Light scattering spectroscopy is a feasible method to achieve this task. Much of the formal theory of light scattering is common to all varieties of measurement. Its value as a tool for investigating the properties of matter, however, was fully realized only with the interpretation and observation of inelastic light scattering by Brillouin and Raman in 1920s. The invention of the laser has extended

1.5 Motivation for this research

The desirability of extending knowledge of the type of transition, the defect species involved, the nature and configuration of defect interactions, the mobility of defects and the extent of disorder at and above the superionic transition to pure and doped LaF_3 has prompted the present light scattering studies.

From the experimental point of view, the results of Brillouin and Raman studies will be used to analyse different superionic mechanisms proposed in the literature.

The conclusions of this research program will add new information about the onset of disorder for this class of superionic conductors.

the study of Cheetham *et al.* (1975) did not in itself completely discriminate between the P3c1 and P6$_3$cm space groups. However, all the indirect evidence pointed to P3c1 as the most favourable space group.

1.4.8 EXAFS

Extended X-ray Absorption Fine Structure (EXAFS) is relatively a new technique which reflects local structural ordering within condensed materials, being able to detect subtle changes in the local structural environment of specific atom types. Therefore, it is potentially useful in the study of disorder in ionic solids (Catlow 1985).

The variation of a crystal's X-ray absorbance as a function of incident X-ray energy at and beyond the absorption edge is measured in these experiments. Extracting quantitative information from EXAFS data usually involves the calculation of a theoretical spectrum from a proposed structure. For this reason computer simulations are used as complementary techniques to provide very detailed models of the local structural environment of particular atoms.

These two combined techniques were successfully used by Catlow *et al.* (1985) to prove the existence of different types of clusters in crystals with fluorite structure.

and noted small anomalies in their data.

1.4.7 Neutron scattering

The diffraction of neutrons by crystals has been the subject of much experimental and theoretical studies since 1940s. Thermal neutrons have a de Broglie wavelength of the order of the interatomic spacing in crystals and energies of the order of the energies of the lattice vibrations so that they can be used in diffraction studies. A distinction between the coherent and incoherent scattering of neutrons is made. Coherent inelastic scattering of thermal neutrons is of particular interest since from a study of the energy change of the scattered neutrons for a given momentum transfer the phonon dispersion curve, the relation between the frequencies of modes of a given polarization and wave vector $\vec{K}$ can be obtained. Incoherent inelastic scattering is also of considerable interest, since the energy distribution of the scattered neutrons is related to the frequency spectrum of the crystal.

Neutron scattering experiments can monitor the relative position of the ions in a given crystal. Short-lived structures known as clusters which modify the vibrational properties of a crystal were proposed for fluorites by Hutchings *et al.* (1984) using these techniques.

De Rango *et al.* (1960) and Cheetham *et al.* (1975) performed neutron scattering on LaF_3. The first group suggested the space group $P\bar{6}cm$, while the second proposed the space group $P\bar{3}c1$ as results of their analyses. In fact,

1.4.6 Ultrasonics

This is the most widely used approach for determining the elastic stiffness constants of anisotropic solids and the variation of these constants with temperature, pressure, *etc* (Every 1994). It is accurate to describe it as a family of techniques, which have in common that they involve the transmission of plane acoustic waves in various (usually high symmetry) directions through the solid, and the determination of the elastic stiffness constants from the measured phase velocities of these waves. Pulsed as well as continuous wave methods are used. The generation and detection is usually done with piezoelectric transducers which couple through faces of the sample which are cut normal to the required propagation directions. By making use of reflection, a single transducer can serve as both source and detector. Some approaches use buffer rods to filter out misleading echoes.

There have been numerous approaches developed that by means of phase interference or pulse overlap allow high accuracy to be achieved, particularly with regard to the measurement of changes in elastic constants with temperature and pressure *etc*. Among these techniques are a double pulse phase comparison method developed by Williams and Lamb (1958), and a pulse superposition method developed by McSkimin (1961).

Over the years there has been a considerable amount of work done on fluorite crystals using these methods (Manasreh and Pederson 1984, 1985). The first sound velocity data for LaF$_3$ have been reported by Krischer (1968). Aliev *et al.* (1984) measured the acoustic mode velocities between 250 and 410 K

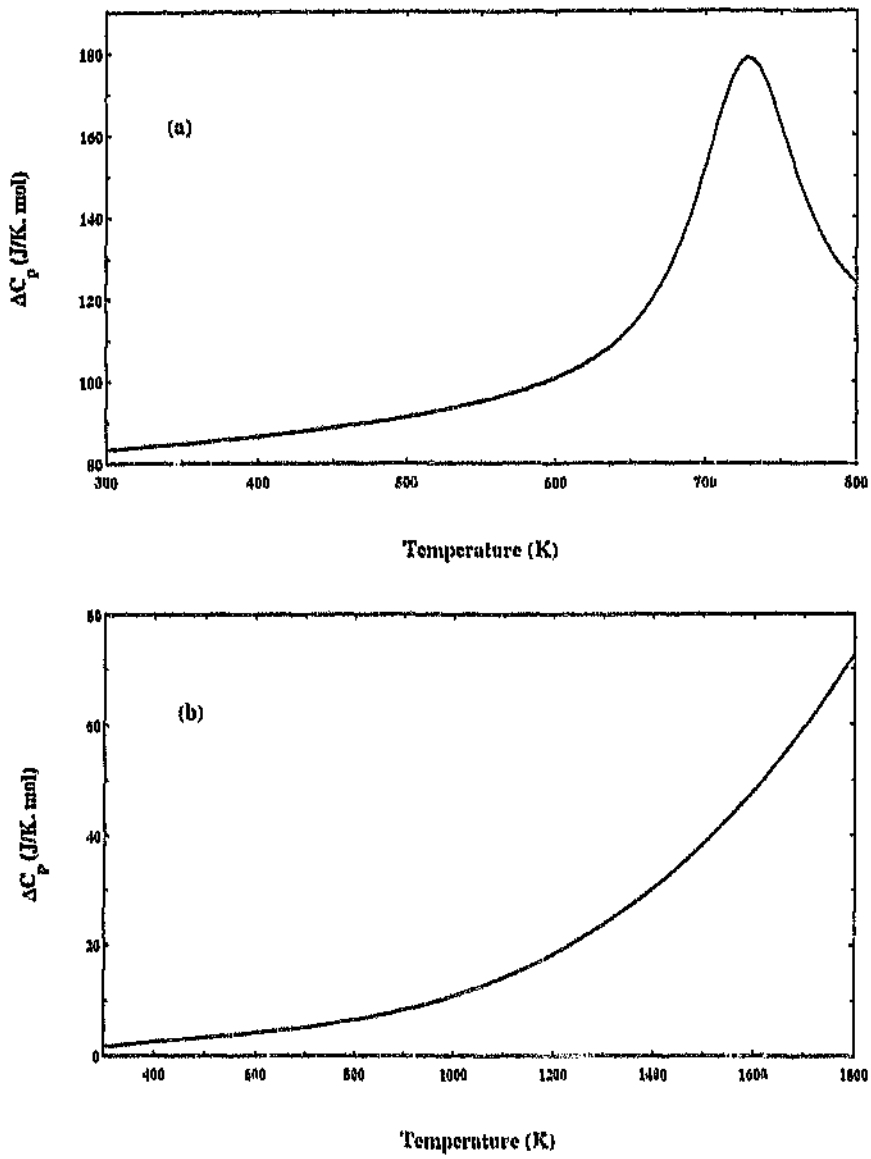

Figure 1.6: (a) The isobaric specific heat, C_p, of β-PbF_2 (after Schroter and Nolting 1980) (b) The difference between the experimental and Debye heat capacities ΔC_p for LaF_3 as a function of temperature.
(After Lyon *et al.* 1978)

high gyro-magnetic ratio which means the NMR signal is large. The one disadvantage of the technique is that the samples must have a low concentration of paramagnetic impurities, since they will cause relaxation and mask the effects of diffusion (Hogg *et al.* 1977, Gordon and Strange 1978). The precision of an NMR data point is around ±10% and parameters are obtained from Arrhenius energies.

Several NMR studies on LaF_3 have been made at temperatures below T_c and will be outlined in Chapter 4.

1.4.5 Specific heat

The analysis of the isobaric specific heat, C_p, data of solids is one of the oldest methods of showing the existence of point defects and of providing estimates of the thermodynamic parameters for defect formation (Lidiard 1957, Chadwick and Glyde 1977). Close to the melting point C_p for fluorite compounds rises rapidly above the value, C_{po}, expected for a perfect, defect-free crystal (Figure 1.6a). The latter is usually obtained by extrapolation of the low-temperature data points. The peak of the anomaly normally defines the transition temperature to the superionic state (Catlow *et al.* 1978). Another type of behaviour was observed for LaF_3 by Lyon *et al.* 1978 (Figure 1.6b). This study will be reviewed and used to explain the behaviour of pure LaF_3 in Chapter 4.

presented in Chapter 4.

1.4.4 Nuclear magnetic resonance

An alternative method of obtaining information on the ionic transport in materials is nuclear magnetic resonance (NMR). This is a powerful technique which, in addition to providing a microscopic probe of the material, presents some advantages over bulk conductivity measurements in superionic conductors (Whittingham and Silbernagel 1977, Richards 1979). It can be used on single-crystal, polycrystalline and powdered samples, although more information can be obtained from studies on oriented single crystals. NMR also works well on both electronically conducting and insulating materials. As a result, it provides a means of measuring the ionic contribution to the conductivity when the electronic component is non-negligible. In addition, since NMR monitors all the ions of a given element in a material, it can distinguish between cases where the conductivity is dominated by ionic motion along the surface of the sample, along grain boundaries or through the bulk of the materials. Since NMR does not depend on the jump distance, however, it cannot easily distinguish between a local motion and the long range motion needed for good DC ionic conductivity. On the other hand, it provides a direct measure of the ionic hopping rate without a knowledge of the jump distance.

NMR is in principle an excellent method for studying fluorine ion motion in fluorides. The ^{19}F isotope is of 100% natural abundance, has spin $\frac{1}{2}$ and has

relation (Hayes 1982):

$$\sigma = \frac{D_\sigma n(Ze)^2}{kT} \sim \frac{\nu l^2\, n(Ze)^2}{6 \quad kT}, \tag{1.8}$$

where n and Z are defined as in Equation 1.6 and ν^{-1} is the time it takes an ion to hop an average distance l.

The Haven ratio, H_R, was introduced to classify diffusion mechanisms when tracer diffusion measurements for independent and identifiable tracer atoms are made and can be corroborated with ionic conductivity experiments (Haven, 1978). H_R is defined as the ratio of the tracer diffusion coefficient to the diffusion coefficient obtained from ionic data. In general each diffusion mechanism has a unique theoretical value for H_R and consequently careful measurements of H_R have proved valuable in identifying diffusion mechanisms.

Although many studies have been directed towards the collection of experimental data, the models proposed for ionic conductivity in LaF_3 are subject of much controversy (Jordan and Catlow 1987) because of the high experimental error caused by many factors which adversely affect the measured data. A main disturbing factor is the reactivity of LaF_3 towards oxygen and water vapour which interferes strongly in the experimental characterization of the ionic transport (Chadwick *et al.* 1979). The main conclusion of these analyses is that the gross features of ionic conductivity can be explained in terms of the defect interactions.

The ionic conductivity studies on LaF_3 assist in the interpretation of the data

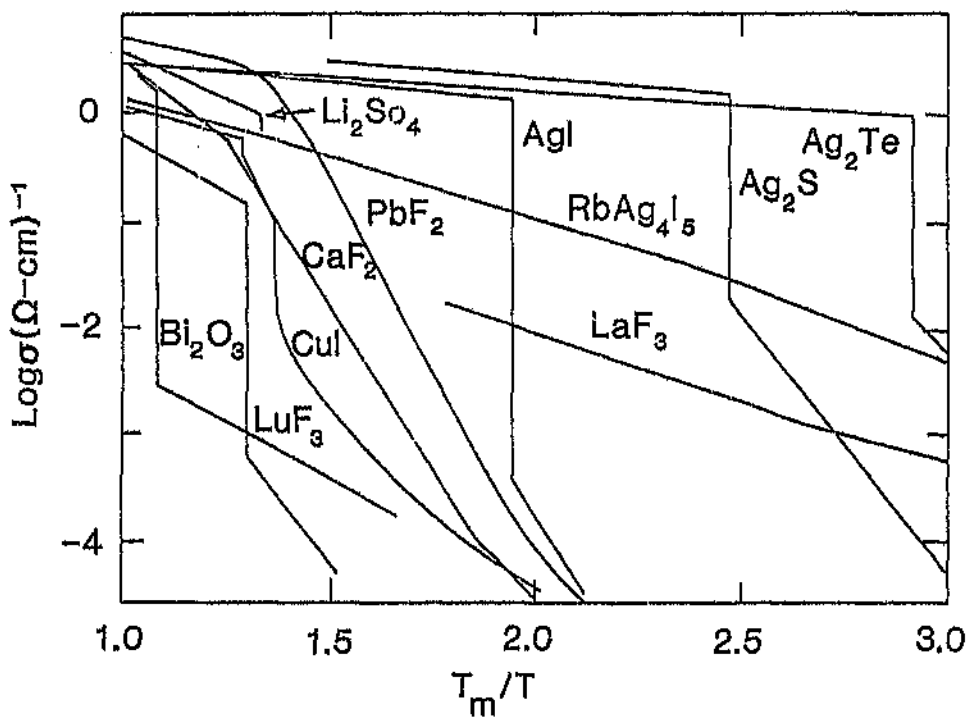

Figure 1.5: Ionic conductivity of different superionic conductors. T_m is the melting temperature of these materials (After Boyce and Huberman 1979).

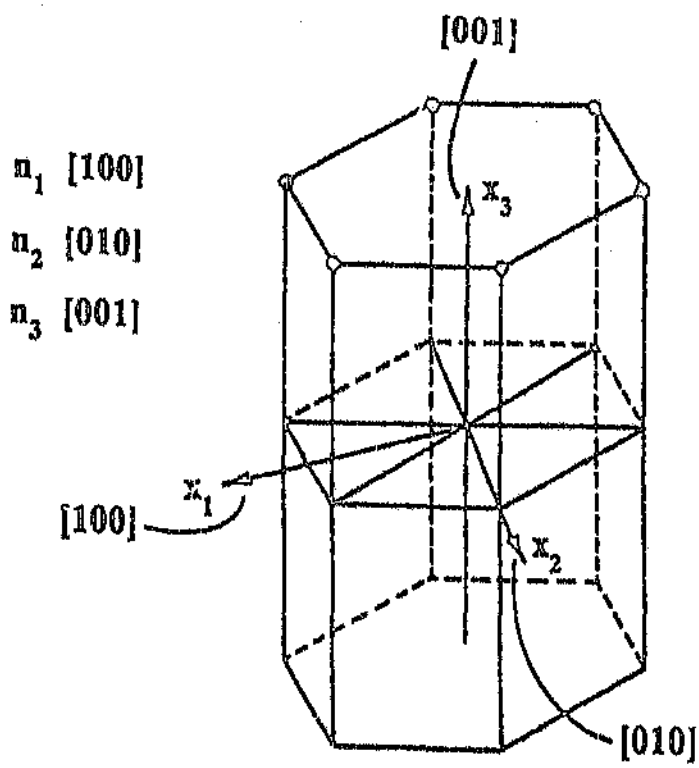

Figure 2.1: Coordinate system for a hexagonal crystal using orthogonal axes (After Truell *et al.* 1969)

$$[(C_{13}+C_{44})n_1n_3]u_1^0+[(C_{13}+C_{44})n_2n_3]u_2^0+$$

$$[C_{44}(n_1^2+n_2^2)+C_{33}n_3^2-\rho v^2]u_3^0=0. \tag{2.11}$$

Using the coordinate scheme of Figure 2.1, it is seen that wave transmission along the x_1 axis is given by $n_1=1$, $n_2=n_3=0$. This set of conditions yields the equations:

$$(C_{11}-\rho v^2)u_1^0=0,$$

$$[\frac{1}{2}(C_{11}-C_{12})-\rho v^2]u_2^0=0,$$

$$(C_{44}-\rho v^2)u_3^0=0, \tag{2.12}$$

which means that a compressional wave propagating along x_1 axis will have a velocity given by

$$\rho v^2_{[100]}=C_{11}, \tag{2.13}$$

and transverse waves propagating along x_1 will have velocities given by

$$\rho v^2_{[100]}=C_{44}, \tag{2.14}$$

with polarization in the x_3 or [001] direction, or

$$\rho v^2_{[100]}=\frac{1}{2}(C_{11}-C_{12}), \tag{2.15}$$

with polarization in the x_2 or [010] direction.

choose $\vec{K}$, and solve Eq. 2.10 for the three velocities v_μ (μ=1,2,3). For each v_μ the three displacement vectors $\vec{u}_i^0$ can then be found from the equations of motion.

The $\vec{u}_\mu$ may be computed directly if the elastic constants are known. Conversely, the elastic constants may be deduced from measurements of the velocity using ultrasonic methods, or equivalently from measurements of the Brillouin shifts.

2.3.2 Solutions of Christoffel's equation for hexagonal crystals

Solutions of Christoffel's equation for a hexagonal crystal will now be considered. In the hexagonal system there are five independent elastic constants: $C_{11} = C_{22}$; C_{12}; $C_{13} = C_{23}$; C_{33}; $C_{44} = C_{55}$; $C_{66} = \frac{1}{2}(C_{11} - C_{12})$. Using equation 2.9 together with the elastic constant scheme leads to the following three equations:

$$[C_{11}n_1^2 + \frac{1}{2}(C_{11} - C_{12})n_2^2 + C_{44}n_3^2 - \rho v^2]u_1^0 + [\frac{1}{2}(C_{11} + C_{12})n_1n_2]u_2^0 +$$

$$[(C_{13} + C_{44})n_1n_3]u_3^0 = 0,$$

$$[\frac{1}{2}(C_{11} + C_{12})n_1n_2]u_1^0 + [\frac{1}{2}(C_{11} - C_{12})n_1^2 + C_{11}n_2^2 + C_{44}n_3^2 - \rho v^2]u_2^0 +$$

$$[(C_{13} + C_{44})n_2n_3]u_3^0 = 0,$$

$11 \rightarrow 1$; $22 \rightarrow 2$; $33 \rightarrow 3$; $23,32 \rightarrow 4$; $13,31 \rightarrow 5$; $12,21 \rightarrow 6$.

Thus, the matrix of constants for a trigonal crystal (classes 32, 3m, $\bar{3}$m) may be written (Pollard 1977):

$$\begin{pmatrix} C_{11} & C_{12} & C_{13} & C_{14} & 0 & 0 \\ C_{12} & C_{11} & C_{13} & -C_{14} & 0 & 0 \\ C_{13} & C_{13} & C_{33} & 0 & 0 & 0 \\ C_{14} & -C_{14} & 0 & C_{44} & 0 & 0 \\ 0 & 0 & 0 & 0 & C_{44} & C_{14} \\ 0 & 0 & 0 & 0 & C_{14} & \frac{1}{2}(C_{11} - C_{12}) \end{pmatrix}$$

The elastic constant matrix for a hexagonal crystal (all classes) is as follows:

$$\begin{pmatrix} C_{11} & C_{12} & C_{13} & 0 & 0 & 0 \\ C_{12} & C_{11} & C_{13} & 0 & 0 & 0 \\ C_{13} & C_{13} & C_{33} & 0 & 0 & 0 \\ 0 & 0 & 0 & C_{44} & 0 & 0 \\ 0 & 0 & 0 & 0 & C_{44} & 0 \\ 0 & 0 & 0 & 0 & 0 & \frac{1}{2}(C_{11} - C_{12}) \end{pmatrix}$$

This last matrix of elastic constants is relevant to LaF_3 for reasons to be discussed in Chapter 4.

In any given crystal class, beginning with a suitably reduced set of C_{ij}, one can

constants.

Equation 2.7 was first published by Christoffel in 1877 and has since been discussed by numerous authors (Love 1944, Musgrave 1970, Every 1980).

One seeks plane-wave solutions

$$u_i = u_i^0 e^{iK_i x_i - \omega t}, \tag{2.8}$$

Taking $\omega^2/K^2 = v^2$, and considering the unit vector $\vec{n} = (n_1, n_2, n_3)$ normal to the wavefront, the equation of motion 2.7 becomes:

$$c_{ijkl} u_l^0 n_k n_j = \rho v^2 u_i^0. \tag{2.9}$$

Equation 2.9 is a solution of the Christoffel equation if

$$\det \left| c_{iklm} n_k n_l - \rho v^2 \delta_{im} \right| = 0. \tag{2.10}$$

For each crystal class, the number of elastic constants c_{iklm} are restricted by symmetry and many of them vanish identically which considerably simplifies the solution of the secular equation. For the most general anisotropic body, the number of independent elastic constants is 21. Depending on the crystallographic class, there are 7 or 6 independent constants for a trigonal system. The number of elastic constants is 5 for a hexagonal crystal. It is customary to use an abbreviated notation (sometimes referred to as Voigt's notation) in place of the full tensor notation. The following scheme is adopted:

spectrum is restricted to a very small spectral region less than 1 cm^{-1}.

Since the long wavelength acoustic modes involve in-phase motion of all the atoms in the unit cell, the atomic displacement are nearly constant over distances on the order of ≈100 unit cells, so that one may discuss these modes in terms of an elastic continuum Debye model. In this case, the relations of Eqs. 2.4 are readily derived by considering Bragg scattering from a sound wave and computing the resultant Doppler shift. Brillouin(1922) was the first to use this approach and showed that the frequency shifts were given by Eq. 1.5.

Prior to discussing the Brillouin tensors, a brief review of elasticity is undertaken.

2.1 Theory of elasticity

All solid bodies are characterized by their ability to carry longitudinal as well as transverse elastic waves. The velocities of propagation of these waves are different in different directions and are determined by the elastic constants of the solid. Therefore, in order to analyse the Brillouin spectra, the normal acoustic modes of the crystal must be known.

From the classical theory of elasticity (Landau and Lifshitz 1970), the equations of motions are:

$$\rho \ddot{u}_i = c_{iklm} \frac{\partial^2 u_m}{\partial_{x_k} \partial_{x_l}}, \tag{2.7}$$

where $\vec{u}=(u_1,u_2,u_3)$ is the local displacement vector, and c_{iklm} are the elastic

selection rules, however, can be found directly from the symmetry properties of the crystal (Loudon 1964, 1965).

2.3 Brillouin scattering in crystals

Brillouin (1922) predicted that there would be components in the spectrum of light scattered by liquids and solids whose frequency would be shifted from that of the incident light by interaction with thermally excited sound waves in the scattering medium. This effect was first observed by Gross (1930) who was using a mercury discharge lamp as the source of exciting light. With the advent of the gas laser, Brillouin scattering experiments acquired an ideal source of excitation and since the first reported experiment by Benedek and Fritsch (1966) there has been continued interest in this technique. As can be seen in Figure 2.2, the three branches for which $\omega \to 0$ as $K \to 0$ start off with constant slope, the range of K in the dispersion curve (first Brillouin zone) being typically $\sim 10^8$ cm^{-1}. In the light-scattering regime ($\vec{K} \sim 2\times10^5\ cm^{-1}$) the acoustic dispersion is given by the relation

$$\omega_\mu(\vec{K}) = v_\mu(\vec{K})K, \qquad \mu = 1,2,3. \tag{2.6}$$

In this case the index μ, commonly called the polarization index, denotes the possibility of one longitudinal and two transverse acoustic modes of the medium associated with the wave vector $\vec{K}$. Because the frequencies of acoustical modes are very much smaller than those due to optic modes, the Brillouin

are not involved in light scattering so that the momentum conservation law is effectively exact (Dil 1982).

The momentum selection rules $\left|\vec{K}\right| = \left|\vec{k}_s - \vec{k}_i\right|$ restrict first order light scattering spectroscopy to a very small fraction of the modes lying close to the center of Brillouin zone. In second order scattering light is scattered by 2 phonons, and Eqs. 2.4 apply to the sum of momenta and energy for the 2 phonons together. Second order scattering arguments have been used by Klemens (1966) in order to explain inelastic scattering by phonons. This model will be presented in Sec 2.4.3.

Various quantities have been introduced to represent the intensity of the components in the scattered spectrum. A very useful quantity is the Rayleigh ratio, or differential cross section per unit volume. For incident light polarized in a direction β, and scattered light polarized in the direction α,

$$R_{\alpha\beta} = \frac{1}{V}\frac{d\sigma}{d\Omega} = \frac{r^2 I_s^\alpha}{V I_i^\beta}, \tag{2.5}$$

where V is the scattering volume from which light is being collected and r is the distance from the scattering volume to the detector. The Rayleigh ratio has the dimensions of an inverse length.

For Brillouin scattering $R_{\alpha\beta}$ can be specified completely in terms of macroscopic parameters of the crystal as it will be shown in Section 2.3.3.

For Raman scattering, the computation of the magnitude $R_{\alpha\beta}$ ($\approx 10^{-9}$ cm^{-1}) is extremely complicated and has only been considered in a few cases. The

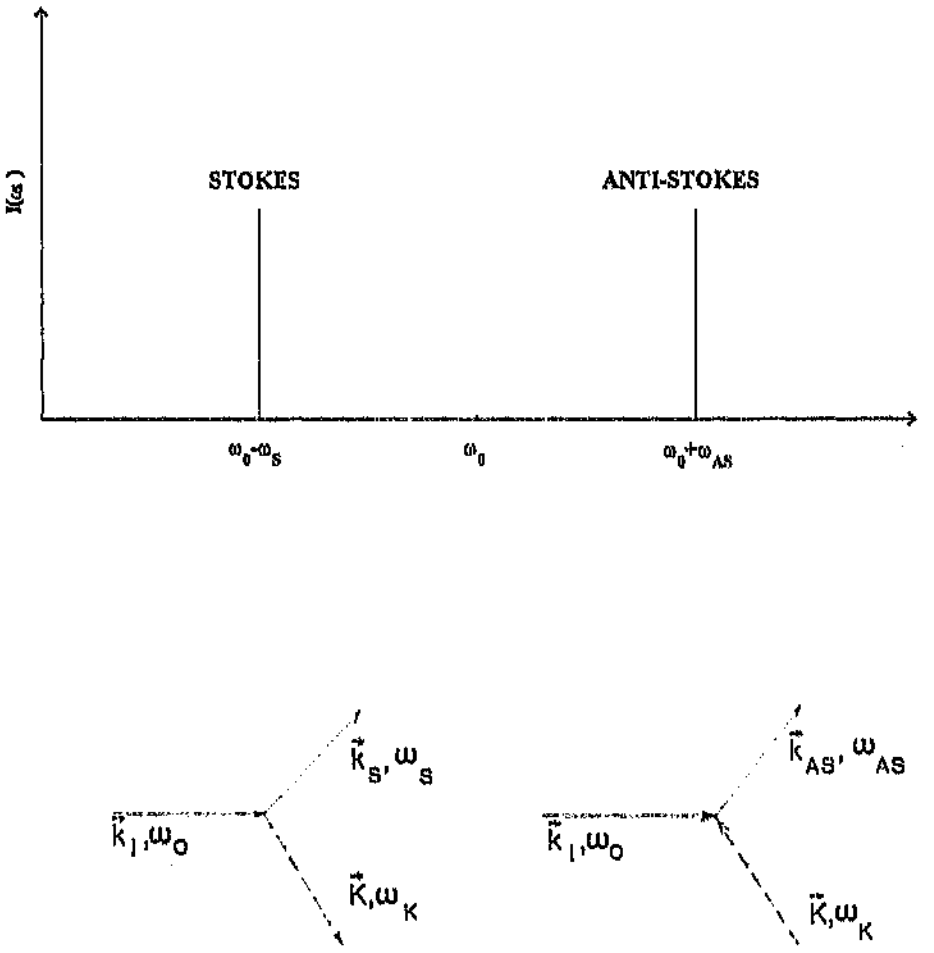

Figure 2.3: First-order photon-phonon scattering diagrams.

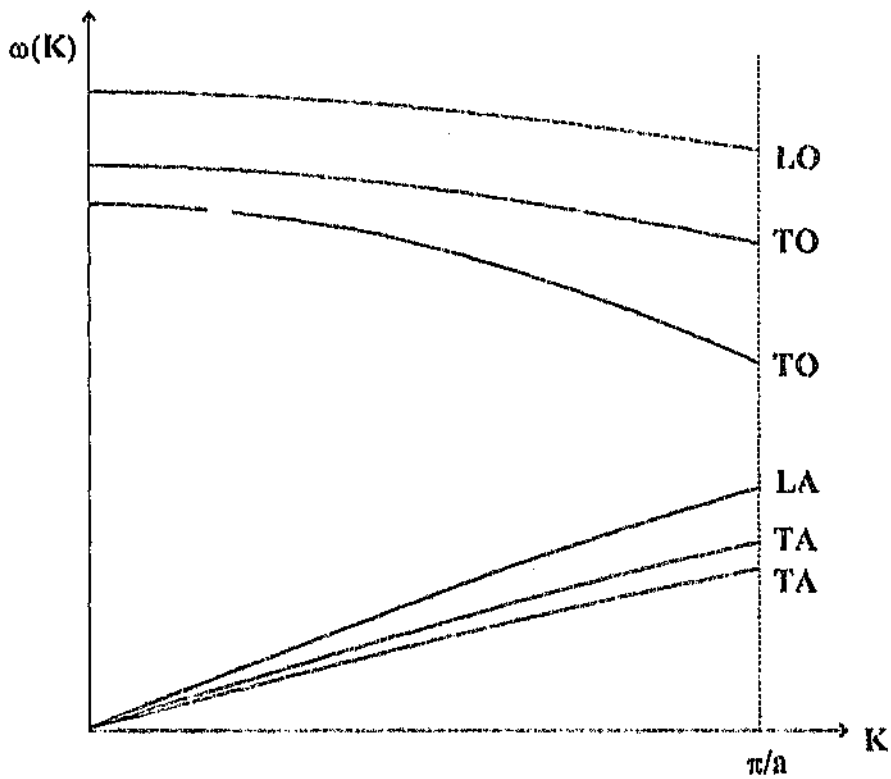

Figure 2.2: Schematic dispersion curves for lattice vibrations showing optical and acoustic branches in the first Brillouin zone for a particular direction.

imposes wave vector conservation. Thus, of $3Ns$ normal modes in a crystal, kinematically only $3s$ of them (one from each branch) can produce scattering of light of frequency ω_o in any given direction θ. The scattered field will thus consists of components at $\omega_o \pm \omega_K$ where ω_K are the $3s$ frequencies at which a vertical line at $\left|\vec{K}\right| = \left|\vec{k}_i - \vec{k}_s\right| \approx 2\left|\vec{k}_i\right| \sin\frac{1}{2}\theta$ intersects the $3s$ branches of the dispersion curve (Fig.2.2). The same results are readily obtained from the second-quantified theory of lattice dynamics (Born and Huang 1962). Each normal mode $\{\vec{K},\omega\}$ is described in terms of a number of quanta (phonons) of energy $\hbar\omega$ and crystal-momentum $\hbar K$. A light scattering event is produced by the creation or annihilation of a phonon as indicated in Fig. 2.3. Conservation of energy and momentum between the photons and phonons yields:

$$\omega_s = \omega_o - \omega_K$$

Stokes event,

$$\vec{k}_s = \vec{k}_i - \vec{K},$$

(2.4)

$$\omega_s = \omega_o + \omega_K$$

Antistokes event.

$$\vec{k}_s = \vec{k}_i + \vec{K}$$

The momentum conservation law is not absolute because the Hamiltonian of the crystal is not invariant under all translations, but only under translations through discrete lattice vectors. However the cases where momentum is not conserved (Umklapp processes), very important in electron or x-ray scattering,

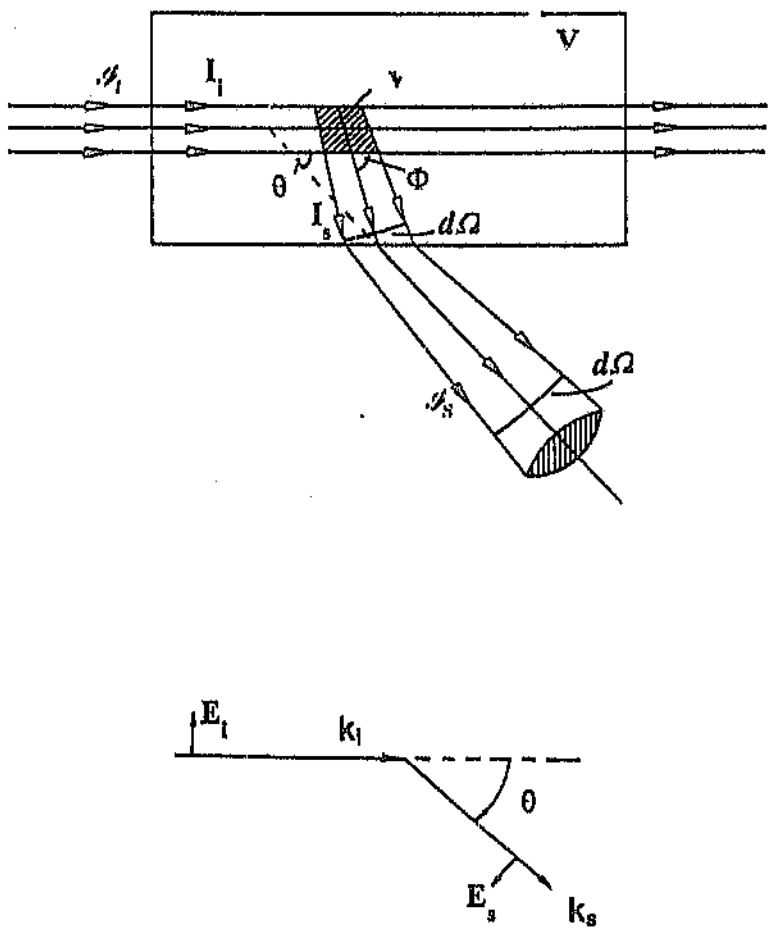

Figure 2.1: The geometry of a light scattering measurement
(After Hayes and London, 1978)

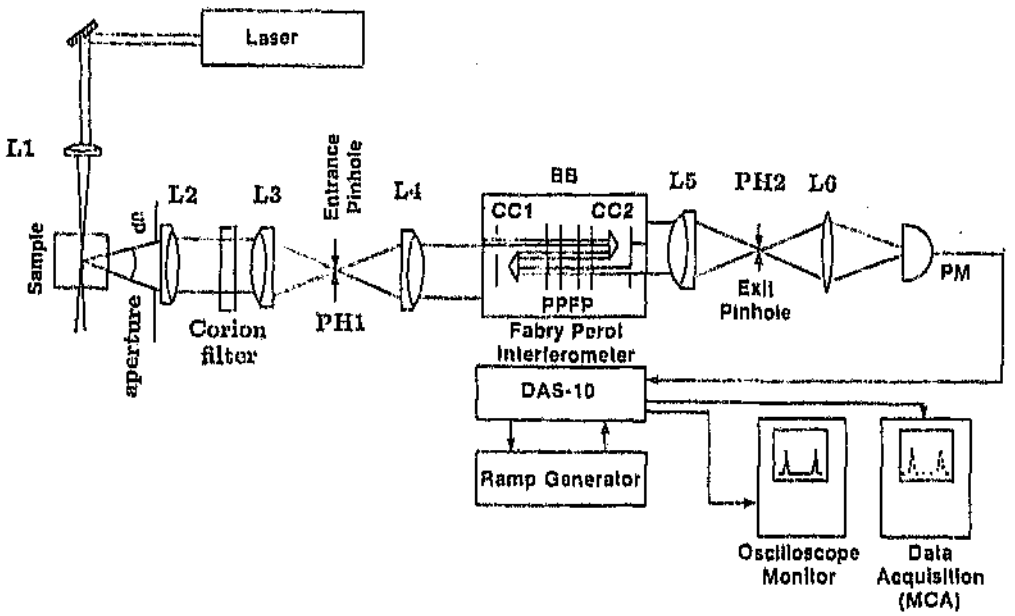

L1-L6	lenses	**PPFP**	plane parallel Fabry-Perot
CC1-CC2	corner cubes		interferometer
BB	light-tight housing	**DAS-10**	data acquisition stabilization system
PM	photomultiplier tube	**MCA**	multichannel analyser

Figure 3.1: Experimental arrangement for Brillouin measurements using the Burleigh 3-pass spectrometer

3.1 The optical systems

A light scattering optical system consists basically of the laser, a spectrometer, the focussing, collection and filtering systems, the collimator and the detection system.

Three optical systems were used in this project. The schematic diagrams of the complete experiments are shown in Fig. 3.1, Fig. 3.2, and Fig. 3.3. The two Brillouin systems used have several features in common but have different operational principles for the respective interferometers. One system uses a classical Burleigh 3-pass Fabry-Perot interferometer, the other a state-of-the-art Sandercock 6-pass tandem Fabry-Perot interferometer, the latter also employing an acousto-optical chopper to minimise the Rayleigh peak.

The optical equipment was mounted and aligned on special spectroscopic tables. The mechanical stability of this tables must be such that the image of the focal spot at the sample never misses the spectrometer's entrance, slit or pinhole. Two massive s were designed in our lab and were made from concrete. The other table was bought from Newport (USA) being a research grade high performance spectroscopic table and was used to support the Sandercock tandem interferometer. These tables isolated the optical systems from floor vibrations in the range of 50 to 200 Hz. Furthermore, the delicate Sandercock tandem interferometer was mounted on a compact modular dynamic antivibration system offering dynamical isolation against all six translational and rotational vibrations in the range of 1 Hz to 100 Hz. In this system, the inertial feedback is used via electromagnetic transducers to provide not only

Chapter 3

Experimental apparatus and techniques

This Chapter describes the apparatus used in this work and the techniques employed to measure Brillouin and Raman scattered light by superionic conductors at high temperatures. The optical systems are presented in Section 3.1. The vacuum optical furnace used for heating samples to high temperatures follows in Section 3.2. The sample preparation system is outlined in Section 3.3.

some time ago.

Different mechanisms of broadening will be analysed in Chapter 4 in order to explain the extra-broadening which occurs at phase transition in pure and doped LaF_3.

nite peaks rather than delta-function singularities which are shifted relative to those predicted in the harmonic approximation at the temperature under consideration. At higher temperatures, the anharmonicity of the potential will lead to increased phonon-phonon interactions that result in scattering and shorter lifetimes of these optical phonons with a concomitant increase in the population of acoustical phonons. Hence, the effects of energy shift and width will be functions of temperature. This problem has, in the past, been the subject of extensive theoretical (Maradudin and Fein 1962, Cowley 1965, Klemens 1966) and experimental (Temple and Hathaway 1973, Balkanski *et al.* 1983) studies. The most commonly used model assumes decaying of the phonon with harmonic frequency ω_0 to two and three phonons of frequencies $\omega_0/2$ and $\omega_0/3$, respectively. The relevant expression for the temperature (T) dependent broadening of the Raman lines is (Balkanski *et al.* 1983):

$$\gamma(T) = \gamma_0 + A(n_2 + \frac{1}{2}) + B[(n_3 + \frac{1}{2})^2 + \frac{1}{12}], \tag{2.24}$$

where n_2 and n_3 are the phonon occupation numbers at $\omega_0/2$ and $\omega_0/3$, A and B are positive constants and γ_0 is a term representing a residual broadening due to lattice imperfections. An expression similar to Eq 2.24 describes the frequency shift:

$$\delta\omega = C'(n_2 + \frac{1}{2}) + D[(n_3 + \frac{1}{2})^2 + \frac{1}{12}] + \frac{2D - 3C'}{6}, \tag{2.25}$$

where C' and D are non-negative constants. In spite of recent progress and interest in the two-phonon spectra of solids, the theory of these processes continues to be an open problem as already pointed out by Cardona (1975)

the possible destructive interference and lead to a combined cross section that is N times the single-atom cross section. This simple theory explains only the elastic light scattering.

Raman scattering is an inelastic process because energy is exchanged between the photon and the crystal. As predicted by harmonic theory the scattered Raman spectrum should consist of a number of pure lines or delta-function peaks superposed on a continuous background. The peaks correspond to the so-called one phonon processes in which the photon excites or de-excites a single phonon in passing through the crystal; the location of the peaks follows from conservation equations 2.4 for energy and momentum. The background of the inelastic spectrum is produced by the multi-phonon processes in which the photon excites or de-excites more than one phonon per single scattering event.

When anharmonic forces are present they will manifest in a most significant way in the above mentioned one-phonon peaks. The temperature dependence of the shift and width can be understood in terms of an oscillator that reacts to the anharmonic potential within which the atoms move. Anharmonic forces, if small, can be interpreted as causing an interaction between phonons, as a result of this phonon-phonon interaction the phonons get a finite lifetime while the energies are shifted with respect to the undisturbed values, these values being the values calculated for a harmonic lattice with parameters adjusted at the temperature under consideration, thus including the effects of thermal expansion and self energy shift that arises from phonon coupling at that temperature. As a consequence the inelastic spectrum now exhibits fi-

$\hat{e}_s$. Then the Rayleigh ratio is given by:

$$R_{e_s e_i} = A(\hat{e}_s \cdot \mathbf{T} \cdot \hat{e}_i)^2. \tag{2.22}$$

These principles were used by Bauman and Porto (1967) in order to identify the symmetry of the scattered light in the Raman spectra of LaF_3.

2.4.3 Raman shift and linewidth

Using the Lorentz model, the differential cross section for a single atom for scattering in which the electric vector $\vec{E}_s$ of the scattered light has the direction of a unit vector $\hat{e}_s$ is

$$\frac{d\sigma}{d\Omega} = \frac{r_e^2 \omega^4}{(\omega_0^2 - \omega^2)^2 + \omega^2\gamma^2}(\hat{e}_i \cdot \hat{e}_s)^2, \tag{2.23}$$

where γ is the oscillator damping constant, $\hat{e}_i$ is a unit vector parallel to $\vec{E}_i$, and the quantity r_e is the classical electron radius ($\approx 2.8 \times 10^{-15}$m). Averages of Eq. 2.23 over the two independent directions of $\hat{e}_i$ and $\hat{e}_s$, corresponding to unpolarized incident light and a detector that does not discriminate between the scattered polarizations, give the same expression for differential cross section up to a term $\frac{1}{2}(1 + \cos^2\Phi)$, Φ being the angle between incident and scattered light. The scattering by N identical atoms is obtained upon multiplication of the cross sections given above by N. Landau and Lifshitz (1980) has shown that there is no contradiction in this operation because the spatial fluctuation in the density of a random distribution of atoms diminish

does indeed have multiple components, which can be attributed according to this scheme (Bauman and Porto 1967).

2.4.2 Selection rules

The transformation properties of the Raman-active lattice vibrations may be used to construct scattering tensors relating the polarization of incident and scattered light. The Raman tensors for the trigonal point group $P\bar{3}c1$, which is the most probable description of the LaF_3 structure, are (Bauman and Porto 1967):

$$A_{1g}: \begin{pmatrix} \alpha_1 & 0 & 0 \\ 0 & \alpha_1 & 0 \\ 0 & 0 & \alpha_2 \end{pmatrix} \qquad E_g: \begin{pmatrix} \alpha_4 & \alpha_5 & \alpha_3 \\ \alpha_5 & -\alpha_4 & \alpha_3 \\ \alpha_3 & \alpha_3 & 0 \end{pmatrix}$$

The Raman scattering selection rules can be determined by the following procedure: Suppose that a given lattice vibration perturbs the polarizability, $\alpha_{\mu\nu}$. Then an incident light wave polarized in the μ-direction will produce an excess polarization P_ν in the ν-direction which will re-radiate. However, $\alpha_{\mu\nu}$ can be non-zero if and only if its representation coincides with that of the lattice vibration (Hamermesh 1962). Thus, the form of the polarizability tensors for each vibrational species of any crystal class can be deduced from the transformation properties of the appropriate bilinear form which are listed in the character tables of most group theory texts. In using these tables, one first specifies the polarization directions of the incident and scattered fields, $\hat{e}_i$ and

2.4.1 The normal modes and Raman activity

The actual calculation of the optical-mode frequencies for LaF_3 was not made in the literature, being an elaborate problem. It is possible, however, to predict a great deal about the Raman spectrum from symmetry considerations, utilizing group-theoretical techniques. The procedure is discussed in standard texts on group theory and spectroscopy (Heine 1960, Herzberg 1945) and is summarized very briefly below.

For a given crystal, one first determines how many atoms in the unit cell either remain invariant or are carried to equivalent sites by each symmetry operation of the crystal point group. These numbers are then used to construct the total displacement group D_{tot} which is finally decomposed into a set of irreducible representations of the point group. Each member of the reduced set corresponds to a normal mode of the lattice. In order to determine which mode is Raman-active, from the total displacement group, D_{tot}, one must subtract those modes which correspond to rotation and translation.

Once the symmetry species of the optical lattice modes has been determined, the following rules are used to predict if they will be active in Raman scattering. A lattice vibration is Raman-active only if its representation corresponds to one or more components of the polarizability P. For LaF_3, it is found that for point group $P\bar{3}c1$, A_{1g} transforms like x^2+y^2, z^2 and E_g like (x^2-y^2,xy); (xz,yz). Thus A_{1g} and E_g should be Raman-active. One is thus led to the conclusion that the Raman spectrum of LaF_3 should consists of five totally symmetric A_{1g} bands and twelve degenerate E_g bands. Experimentally, the spectrum of LaF_3

Equation 2.21 gives the scattering cross sections for each acoustic mode in terms of the $\mathbf{T}^{\mu}$-tensors. For scattering geometries in which sound waves propagate in high symmetry directions the structure of the $\mathbf{T}^{\mu}$-tensors is sufficiently simple such that selection rules can be deduced directly. This procedure is used to determine the elastic constants in Chapter 4.

2.4 Raman scattering in crystals

In the microscopic theory of lattice dynamics (Born and Huang 1962), the crystal is viewed as a collection of point masses held together by springs which represent the binding forces in the harmonic approximation. Calculations based on this model predict that for each $\vec{K}$, there are $3N$ modes where N is the number of atoms in the unit cell. The dispersion curves have the form indicated schematically in Fig. 2.2. The $3N-3$ optical branches with nonzero intercepts correspond to unequal motions of inequivalent atoms within each unit cell, and are thus similar to the vibrational motions of molecules. These optical modes are associated with the microscopic crystal structure and are not predicted by the classical structureless continuum theory. The optical modes behave initially as $\omega_j = \omega_j^0 - bK^2$ and for small $\vec{K}$ are practically K-independent.

Optical modes are coupled to the dielectric constant and produce components in the light scattering spectrum of solids. The frequencies of the optical modes are characteristically 100 to 1000 cm^{-1}, and the components which they produce constitute the Raman spectrum.

dielectric tensor produced by the sound wave having velocity $v_\mu(\vec{K})$:

$$[\delta\epsilon^\mu] = KuT^\mu, \tag{2.18}$$

where the element T^μ_{ij} of the tensor $\mathbf{T}^\mu$ is $\epsilon_{ii}\epsilon_{jj}$ times the combination of Pockel's coefficients, namely

$$T^\mu_{ij} = \frac{1}{2}\epsilon_{ii}\epsilon_{jj}\sum_{lm}(\hat{K}_m\hat{u}^\mu_l + \hat{K}_l\hat{u}^\mu_m)p_{ij,lm}, \tag{2.19}$$

where $\hat{K}_m$ is the unit propagation vector and $\hat{u}^\mu_l$ is the unit polarization vector of the sound wave for μ-th mode.

The Rayleigh ratio is easily derived from the excess dipole moment per unit volume $P_\mu(r) = \delta\epsilon_{\mu\nu}E^0_\nu$. The Rayleigh ratio is thus obtained in terms of the mean square displacement $< u^2 >$ which in turn is obtained by equating the mean kinetic energy per mode K to k_BT (Sandercock, 1982):

$$< u^2 >= \frac{4k_BT}{V\rho v^2_\mu K^2}. \tag{2.20}$$

The Rayleigh ratio of the μ-th acoustic mode with velocity v_μ, has the form (Hayes and Loudon, 1978):

$$R_\mu = \frac{k_BT\omega_s^4}{32\pi^2c^4\rho v^2_\mu}[\hat{e}_s\mathbf{T}^\mu\hat{e}_i]^2\frac{n_s}{n_0} = \frac{k_BT\pi^2\rho v^2_\mu}{2\lambda_s^4}[\hat{e}_s\mathbf{T}^\mu\hat{e}_i]^2\frac{n_s}{n_0} \tag{2.21}$$

where ω_s is the angular frequency, c is the vacuum velocity of light, λ_s the (vacuum) wavelength of the scattered light, n_0 and n_s are the indices of refraction of the medium for the light polarized along $\hat{e}_i$ and $\hat{e}_s$, respectively.

2.3.3 Brillouin tensors

The Brillouin spectrum of a crystal arises from fluctuations in the strain tensor η_{lm}, defined as:

$$\eta_{lm} = \frac{1}{2}\left(\frac{\partial u_l}{\partial x_m^0} + \frac{\partial u_m}{\partial x_l^0}\right). \tag{2.16}$$

The coupling of the elastic waves in a crystal to the dielectric tensor is through the Pockel's elasto-optic or photoelastic coefficients $p_{ij,kl}$ according to the equation (Nye 1960):

$$\delta\epsilon_{ij}^{\mu}(r,t) = -\epsilon_{ii}\epsilon_{jj}\sum_{lm} p_{ij,lm}\eta_{lm}^{\mu}(r,t), \tag{2.17}$$

where the Cartesian axes correspond to the principal axes of the dielectric tensor, ϵ_{ii} and ϵ_{jj} being the diagonal elements of this tensor.

The elasto-optic tensor for a trigonal crystal (classes 3m, 32, $\bar{3}$m) can be written in the 6x6 matrix notation using Voigt notation (Nye 1960):

$$\begin{pmatrix} p_{11} & p_{12} & p_{13} & p_{14} & 0 & 0 \\ p_{12} & p_{11} & p_{13} & -p_{14} & 0 & 0 \\ p_{31} & p_{31} & p_{33} & 0 & 0 & 0 \\ p_{41} & -p_{41} & 0 & p_{44} & 0 & 0 \\ 0 & 0 & 0 & 0 & p_{44} & p_{41} \\ 0 & 0 & 0 & 0 & p_{14} & \frac{1}{2}(p_{11}-p_{12}) \end{pmatrix}$$

Having solved the mechanical problem described in Sec 2.3.2 one has the strains η_{kl} for each of the three roots v_μ, and can then compute the distortion in the

The scanning of the Burleigh interferometer is achieved by means of three low expansion rods which support three piezoelectric scanning stacks. One mirror is mounted in a strain-free holder at the ends of the three scanning stacks. The second mirror is attached to the end plate of the structure in such a way that approximate alignment parallel to the first mirror may be obtained by using differential micrometer screws. Exact alignment of the mirrors is achieved by applying suitable bias voltages to the three scanning stacks. The instrument is then scanned by applying a scanning voltage simultaneously to all three scanning stacks.

In the case of the Sandercock tandem interferometer, the scanning mirrors of both interferometers (Fig. 3.5b) sit on a compound stage comprising a deformable parallelogram (for small displacements) attached to a crossed roller translational stage (for large displacement). Since the tandem interferometer uses a translational geometry, the scanning is achieved by using only one piezoelectric crystal acting between the upper plate of the rolling stage and the upper plate of the deformable parallelogram stage. The problem of synchronising the scanning of the individual FPIs is solved as they are different regions of the same mirror and therefore automatically scanned in sequence, provided that the mirrors remain accurately parallel during the scan. A large scan range, and very good static and dynamic synchronizations are very important advantages of the tandem instrument.

Piezoelectric scanning lends itself to dynamic stabilization whereby the instrument is rapidly scanned (one scan per second in these experiments) and continuously realigned to maintain correct mirror sparing and parallelism.

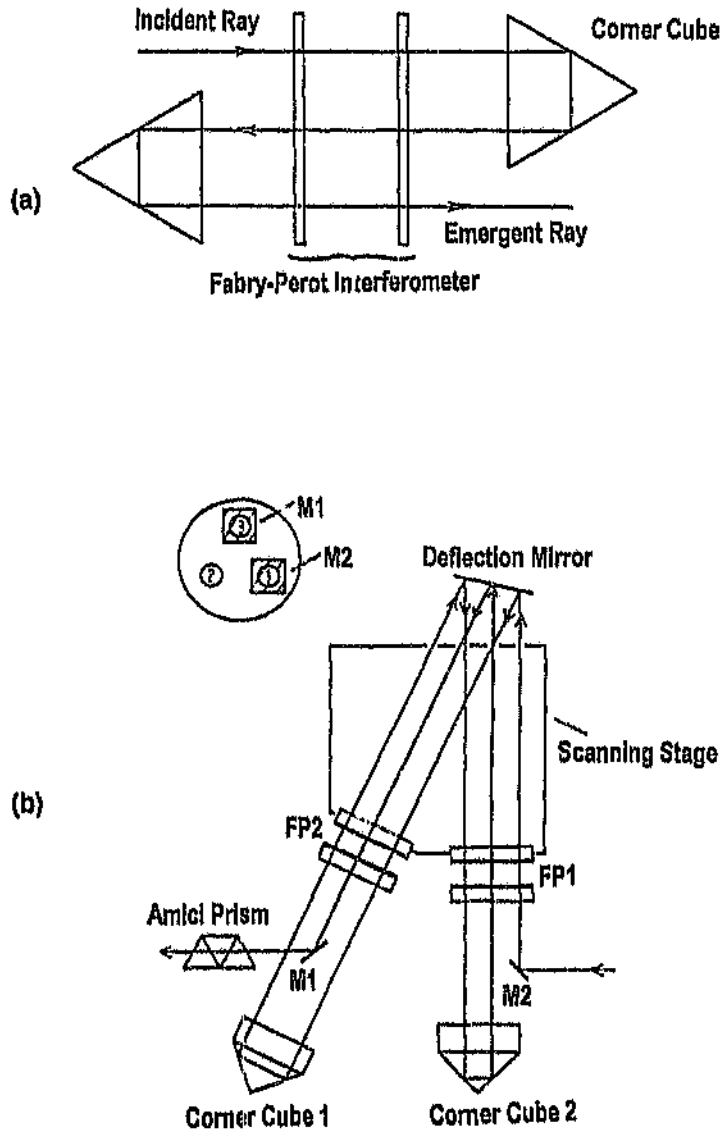

Figure 3.5: (a) Burleigh multipassing scheme (b) Tandem multipassing scheme (After Sandercock 1994)

which defines how much light may pass through the spectrometer:

$$E = S\Omega_S = \frac{\pi}{4} S\alpha^2, \tag{3.9}$$

where Ω_S is the solid angle subtended by the pinhole at the aperture stop. The product $EP = 2\pi S$ is an optical system invariant (Helmholtz-Lagrange invariant) since it is proportional to the area S of the beam. Thus, depending on the experimental goal, it is necessary to choose between high throughput or high resolution before setting up the interferometer.

A major limitation on the application of Brillouin scattering to the physics of condensed matter is the low contrast of the single pass FPI of requisite resolution. This is the inability of the FPI to detect a weak signal in the presence of one more intense (by a factor of about 10^6 to 10^8). In investigations involving crystals which may in extreme cases be opaque or at least contain static imperfections (as in the present study), the scattering from molecular processes can be dominated by a large unshifted Rayleigh peak which obscures the weak spectral components. This has been overcome by the now standard technique of multipassing (Sandercock 1970, 1975; Mock *et al.* 1987), in which the light to be analysed is passed through the FPI a number of times. For the Burleigh interferometer the multipassing scheme is indicated in Figure 3.5a. A 6-pass scheme for a tandem interferometer is presented in Figure 3.5b. Corner cube reflectors are used to return the light parallel to itself. The arrangements shown are equivalent to having three or six identical interferometers in series. The contrast of these systems is given by the product of the individual contrast; $C = (C_1)^n$.

The instrument acts as a tunable filter whose peak transmission is closed to unity over a narrow spectral interval, falling to a very low value outside this interval. Two incident signals of wavelength λ_1 and $\lambda_1 + \Delta\lambda$ will be simultaneously transmitted if

$$m\lambda_1 = (m-1)(\lambda_1 + \Delta\lambda), \tag{3.6}$$

or in other words, neighboring orders of interference are separated in frequency by

$$\Delta\nu = \frac{c}{2nd} \quad . \tag{3.7}$$

This interorder spacing is called the free spectral range (FSR). The width of the transmission peak determines the resolution of the instrument. The ratio of FSR to width is known as the finesse F. The finesse is the key measure of the interferometer's ability to resolve closely spaced lines. The finesse can be thought of as the effective number of interfering beams involved in forming the F.P. multiple-beam interference fringes (Jacquinot 1960). The major factors which limit instrumental finesse are irregularities in the mirror surface, mirror misalignment, diffraction at the mirror aperture, and absorption. In practice, the finesse is limited to values less than about 100 and this places an upper limit on the possible contrast, where the contrast C' is the ratio of maximum to minimum transmission given by

$$C' = 1 + \frac{4F^2}{\pi^2} \approx \frac{4F^2}{\pi^2} \approx 10^4. \tag{3.8}$$

Another important system parameter is the etendue E (also called luminosity)

where n is the index of refraction of the medium between mirrors and m is an integer. In most cases of practical interest, $n=1$ and the beam of light is perpendicularly incident so that $i=0$.

In practice, the interferometer possesses a finite bandwidth $\delta\lambda_s$ (full width at half-maxima) about each transmitted wavelength λ_s. The additional wavelengths are rejected only up to a certain level. The general transmission function T of the interferometer takes the form of the Airy function (Chu, 1974)

$$\mathbf{T} = \frac{\tau_o}{1 + \frac{4F^2}{\pi^2}\sin^2(\frac{2\pi nd}{\lambda}\cos i)} \quad , \tag{3.3}$$

where τ_o is the overall single-pass transmission and F is the effective single-pass finesse.

The acceptance angle δi of the interferometer is easily calculated from Eq. 3.3 and takes the form

$$\delta i = (\frac{\lambda}{2ndF})^{\frac{1}{2}}, \tag{3.4}$$

so that all rays incident on the mirrors should fall within this angle. When the lenses in the beam expander suffer from aberrations, or when the laser does not oscillate in the lowest transverse TEM_{oo} mode, all incident rays may not fall within δi.

According to Eq. 3.3 and taking $i=0$, the instrument will transmit light of wavelength λ_1 if the spacing d is such that

$$d = \frac{m\lambda_1}{2n}. \tag{3.5}$$

3.1.2 Fabry-Perot Interferometer: General characteristics

In the field of Brillouin scattering the most satisfactory instrument available for detection of the frequency shifted components is the Fabry-Perot interferometer (FPI). This instrument has a contrast as high as 10^{12} and is thus well suited for observing the Brillouin components in the presence of the central component where the Brillouin intensities are about 10^{-6}-10^{-7} of the Rayleigh peak intensity and the frequency shifts are normally in the range 100 MHz to 100 GHz (Sandercock 1975). The purpose of this section is to describe the use of the Fabry-Perot interferometer.

In order to achieve sufficiently high resolution for a Brillouin scattering measurement, a FPI is used as a scanning spectrometer. A Burleigh RC-110 and a Sandercock tandem interferometer were used in this work, as illustrated schematically in Figures 3.1 and 3.2.

A Fabry-Perot interferometer consists basically of two very flat ($\lambda/100$ or $\lambda/200$) fused-silica plates with adjacent surfaces coated to a high reflectivity ($R \geq 0.8$) and maintained in a parallel configuration a distance d plus or minus a few optical wavelengths apart.

When a parallel beam of white light is incident on this mirror pair with an angle i, only those wavelengths λ_s are transmitted that match the mirror separation d

$$m\lambda_s = 2nd\cos i, \tag{3.2}$$

ments. This mode provides the smallest beam diameter and divergence angle, and maintains the Gaussian power distribution across the beam when the beam propagates through free space or through properly desigued optical systems. The TEM_{oo} mode can be focussed to the smallest possible spot size, thus the energy density is the highest possible.

An approximate expression for the distance travelled by a light ray before it loses coherence, known as coherence length, is given by

$$L_{coh} = \frac{c}{\delta\nu}. \tag{3.1}$$

When the laser output is changed from single line to single frequency, the coherence length increase enormously. The coherence length for Spectra Physics lasers is of the order of 10 m when operated in the TEM_{oo} mode under these conditions.

transition, by two collisions with electrons. The first ionizes the atom and the second excites the ion from its ground state (E_1) either directly to the $4p$ energy level (E_3) or to E_4, from which it cascades almost immediately to $4p$. The $4p$ ions will eventually decay to $4s$ (E_2), emitting a photon either spontaneously or when stimulated to do so by a photon of equivalent energy. The wavelength of the photon depends on the specific energy levels involved, but it will be between 400 and 600 nm. The ion decays spontaneously from $4s$ to the ionic ground state, emitting a photon in the vacuum ultraviolet -about 74 nm- as it vacates the lower level of the lasing transition.

The most intense lines have wavelengths of 488 and 514.5 nm. In order to eliminate the competition between lines with a common lower level, both Spectra Physics lasers used a prism wavelength selector to restrict laser action to a single spectral line. In order to compensate for the cavity length changes, a compensated rod resonator structure is used by both lasers. The Spectra Physics model 171 laser uses quartz rods, graphite rods being used for the same purpose by the model 2020.

A Spectra Physics Model 593 intracavity etalon, which acts as a bandpass filter was inserted in the cavity of each laser to isolate a single longitudinal mode. This etalon introduces enough loss in all other modes preventing them from reaching the lasing threshold. This is necessary for Brillouin spectroscopy. The internal temperature of the etalon was regulated by a Spectra Physics 482 oven controller within 0.01 K during normal ambient temperature fluctuations.

The lowest transverse TEM_{oo} mode was used in all the scattering measure-

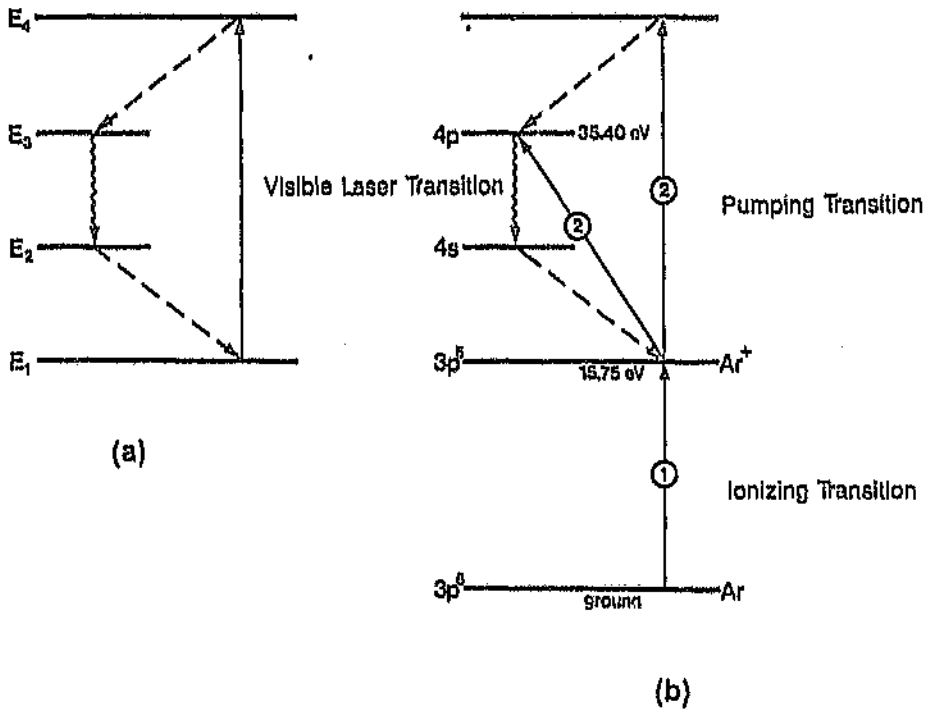

Figure 3.4: A typical four-level transition scheme (a) compared to that of visible argon (b). One collision ionizes neutral argon, and a second pumps the ion to an excited state.

isolation from building vibrations, but also isolation from vibration sources placed on the table itself. This means that the Sandercock tandem interferometer isolated by this system will remain at rest despite forces being applied to the rest of the system.

The Fabry-Perot interferometers, collection and detection systems were mounted in light-tight boxes in order to minimise parasitic light from reaching the photomultiplier tubes.

3.1.1 The laser

The laser is a very important part of the optical system because for light scattering studies one needs an intense, monochromatic, highly collimated and polarized beam of light.

In the present study two different kinds of argon-ion lasers were employed: a Spectra Physics Model 171 and a Spectra Physics Model 2020.

The laser is a device which amplifies the intensity of light by means of a quantum process known as stimulated emission. A practical laser needs a means of amplification (stimulated emission) and a means for feeding the energy back into the system to build up sustained oscillation.

An argon-ion laser operates using a four-level scheme, as depicted in Fig. 3.1. The neutral atom is pumped to the $4p$ energy level, the origin of the lasing

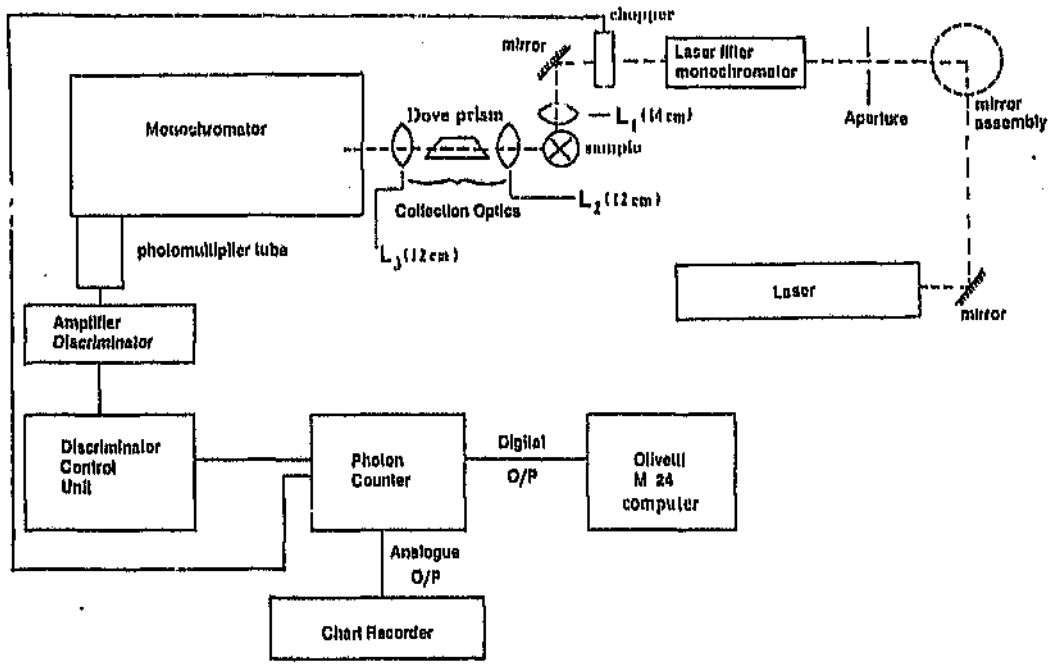

Figure 3.3: Experimental arrangement for Raman scattering measurements. L1-L3 refer to lenses.

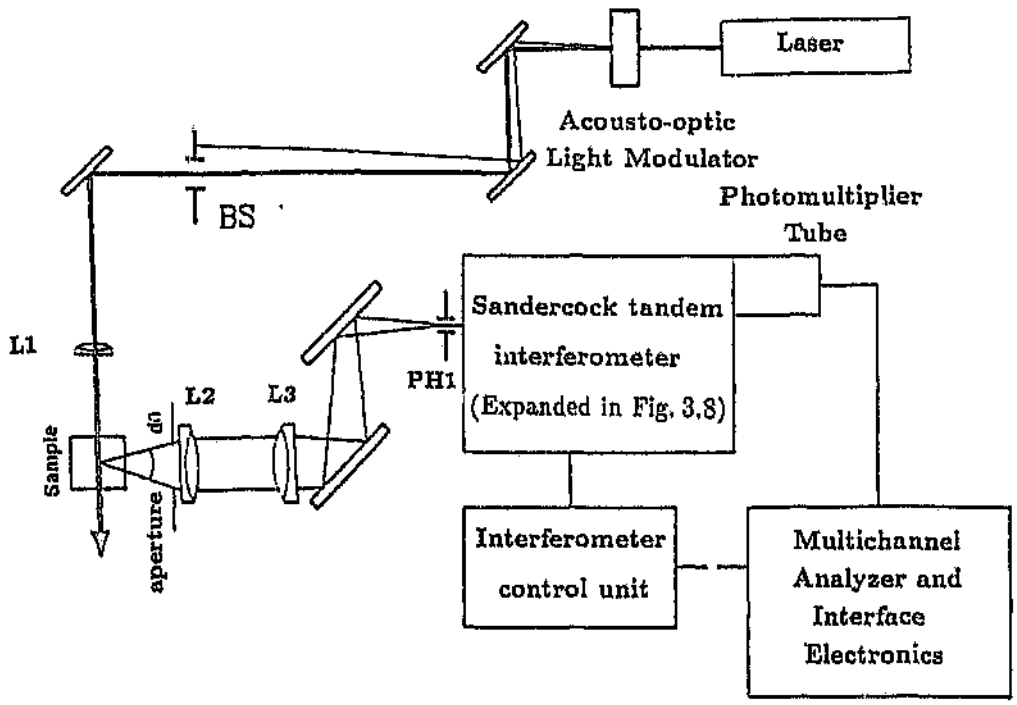

Figure 3.2: Experimental arrangement for Brillouin measurements using the Sandercock 6-pass tandem interferometer. L1-L3 refer to lenses, BS is a beam stop, and PH1 is the interferometers's entrance pinhole.

interval, the photomultiplier measures background only. During each chopper-open interval, the photomultiplier measures signal plus background. A signal supplied by the chopper to the photon counter PAR 1112 trigger circuits synchronizes the signal path switching with the light chopping action. By using two different signal counters and the subtract facility of this photon counter, the signal can be measured without the thermal background caused by heating the sample in the furnace.

The laser beam was directed onto the optical furnace window by a mirror and a 14 cm focal length lens **L1** which focusses the beam into the encapsulated crystal. The optical furnace was mounted on the optical track in a way which made possible to position the crystal properly in the beam. Light scattered at 90^0 by the crystal was collected by a lens **L2** of focal length 12 cm. As the entrance slit of the monochromator has a vertical orientation it was necessary to introduce a dove prism which rotated the beam by 90^0. The image was thereafter focussed by yet another 12 cm lens **L3** onto the entrance slit of the Jarrell Ash monochromator. This arrangement gives unit magnification at the entrance slit.

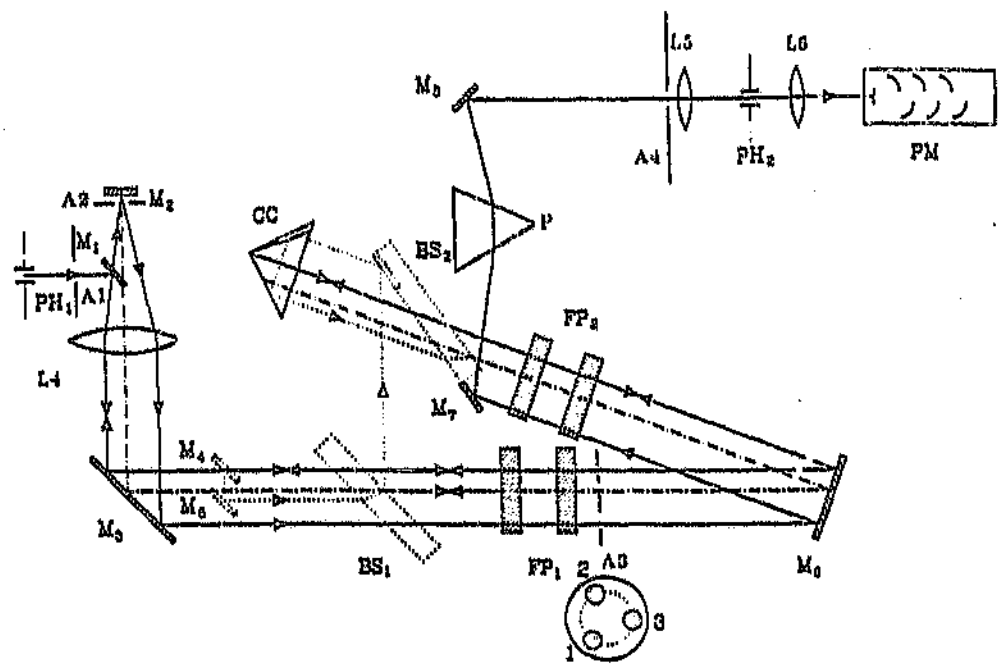

A1-A4	apertures
M1-M0	mirrors
CC	corner cube
BS1, BS2	beam spliters
PH1, PH2	pinholes
PM	photomultiplier tube
P	Prism

Figure 3.8: Optical diagram of the Sandercock tandem 6-pass Brillouin spectrometer

lens **L3** (f=120 cm) are used to raise the scattered beam to the level of the entrance pinhole **PH1** of the tandem interferometer. Instead of using two corner cubes like in Figure 3.5b, two mirrors (**M2, M3**) in connection with the apertures **A1, A2** and one corner cube (**CC**) were employed for multipassing (Figure 3.8). Low frequency Raman and the thermal radiation at high temperatures are removed by the prism **P** and the aperture **A4**. Lenses **L5, L6** and pinhole **PH2** play the same role as in the previous arrangement. The same photomultiplier tube, EMI 9789B, cooled to -15^0 C by a Products for Research housing, was used in both arrangements. The discriminated photomultiplier output pulses were fed to photon counters and re-routed to the interferometers electronics in order to provide automatically the feedback to stabilise these instruments as discussed in Section 3.1.2. The Burleigh interferometer was used in connection with a SSR Model 1140A photon counter, a Stanford SR 400 photon counter being used with the Sandercock tandem instrument. The data was accumulated by a multichannel analyser (MCA) using a Nucleus Computer Analyzer card which was mounted into an Olivetti M24 personal computer.

The Raman scattering equipment is shown in Figure 3.3. Via a system of mirrors the laser beam was raised to the level of the entrance aperture of an Anaspec 300-S continuously tunable laser filter monochromator in order to reduce unwanted plasma lines in the laser output. This output beam was chopped at 210 Hz with a Rofin MKII frequency programmable light chopper, because at temperatures above 1100 K it was found that thermal radiation obscured the Raman signals. As the chopper rotates, the light beam is repetitively interrupted at the chopping frequency. During each chopper-closed

wave vectors for the 90^0 scattering geometry is

$$\frac{dK}{K} \simeq 0.1. \tag{3.11}$$

The light beam leaving the interferometer is collected by a lens (**L5**) which focusses the beam on an exit pinhole. This pinhole is re-imaged on the sensitive area of the photomultiplier tube by another lens (**L6**).

All the lenses and pinholes were fixed on XYZ Microcontrole mounts compounded from three translational stages.

The optical system for the second Brillouin arrangement using the Sandercock instrument is similar in many aspects with the first one. The same principles were employed to design the external optics outside the interferometer.

In order to decrease the elastically scattered light, an IntraAction model 40 acousto-optic light modulator is mounted in front of the laser. The laser beam entering the sound field generated by this device is deflected at an angle proportional to the acoustic frequency and modulated by the signal amplitude applied to the piezoelectric transducer which generates the acoustic waves. By synchronizing the light modulator with the interferometer scanning, the light is modulated only during this operation. Since two beams appear due to diffraction, the undiffracted beam of light is cut off by a beam stop (**BS**).

The same kind of lenses **L1** (f=14 cm) and **L2** (f=12 cm) as in the first arrangement are used for focussing and collecting the light. Two mirrors mounted after

reduce possible low frequency Raman transitions and the thermal radiation at high temperatures. The aperture **A1** was inserted to limit the beam diameter. The beam of parallel light leaving the spatial filter contains mainly light elastically scattered from the sample. The tiny signal in which one is interested is filtered out from this elastically scattered light by the Burleigh Fabry-Perot interferometer. The contrast and finesse of this instrument is drastically improved by passing the transmitted beam sequentially through three different portions of the interferometer mirrors. This is accomplished by means of the two retro-reflecting prisms, **CC1** and **CC2** as shown in Figures 3.1 and 3.5a.

In order to ensure that the contrast of the multiple-pass instrument is not affected by the divergence of the beam leaving the spatial filter, the focal length f of **L3** and **L4**, and the diameter p_1 are chosen such that

$$\frac{p_1}{2f} \leq \delta i, \tag{3.10}$$

where δi is the acceptance angle defined in Section 3.1. The diameter of the beam of parallel light leaving the lens **L4** determines the size S of the areas selected for multipassing on the interferometer mirrors. This diameter is of the order of 10 mm.

The focal lengths of **L1** and **L2** are determined by the condition that the incident focal spot on the sample has to be imaged right on or inside the pinhole. Furthermore, the collecting lens **L2** selects the direction of observation and the solid angle Ω about it. With this arrangement, the spread in scattering

inator followed by a PAR Model 1112 Photon counter Processor. An Olivetti M24 computer captured the output data from the photon counter using an appropriate interface and software developed in our laboratory. The data was stored directly onto a hard disc converted by software from wavelength to wavenumber.

3.1.4 Auxiliary optical system

In this section the design of the optical arrangement will be outlined. In order to measure the Brillouin and Raman frequency shift, the laser beam has to be passed properly through several optical devices before and after its passage through the spectrometers. The purpose of the mirrors, lenses, pinholes and other optical equipment will be analysed.

The optical system for the Burleigh Brillouin scattering arrangement is depicted in Figure 3.1. A laser beam is focused by the lens **L1** on the encapsulated sample which is of 2-4 mm size and mounted in the optical furnace in a 90^0 light scattering arrangement. Through an interaction process, some of this incident light is scattered inelastically and collected by the lens **L2**. In order to unambiguously define the scattering volume in the sample, a spatial filter consisting of the two confocal lenses **L3** and **L4**, and a pinhole **PH1** is introduced. Between this spatial filter and the collecting lens, a Corion SP-5145-1 narrow band spike filter with a bandwidth of 1 nm for the 514.5 *nm* line (or, alternatively, a Corion SP-488-1 filter for 488 *nm* line) is used to substantially

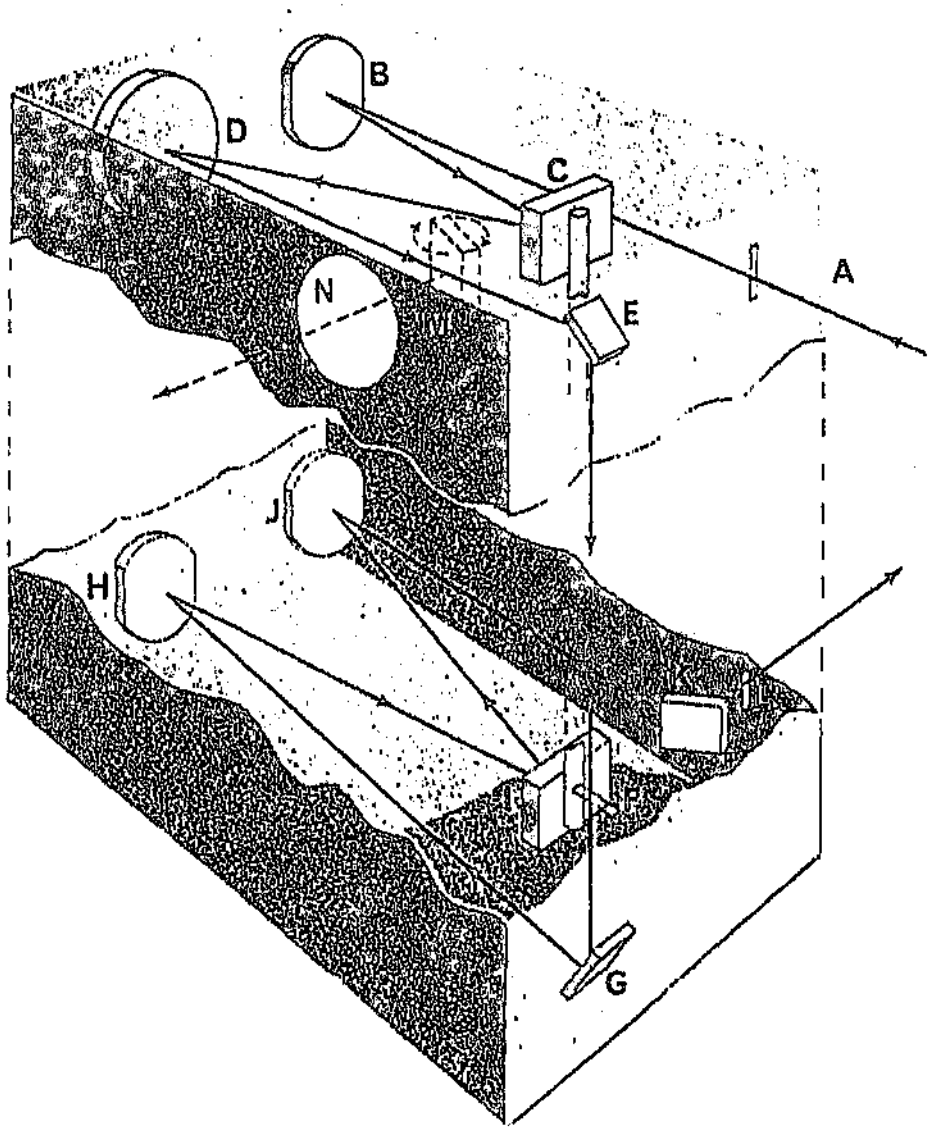

A	entrance slit	**H**	collimating mirror
B	collimating mirror	**I**	grating
C	grating	**J**	focussing mirror
D	camera mirror	**K**	45° mirror
E	45° mirror	**L**	exit slit
F	intermediate slit	**M**	swing out mirror
G	45° mirror	**N**	light path when using only upper section

Figure 3.7: Optical diagram of the Jarrell Ash monochromator. (Courtesy Jarrell Ash)

3.1.3 The Raman monochromator

A Jarrell Ash model 1m double Czerny-Turner 25-100 monochromator was employed to carry out Raman measurements at high temperatures. This model consists of two complete Czerny Turner spectrometers mounted vertically one above the other. Both gratings are mounted on the same pivot to ensure perfectly synchronized rotation. The diagram of the instrument is shown in Figure 3.7.

Light enters the monochromator at the entrance slit **A** going directly to the collimating mirror **B** from whence it is reflected as a parallel beam on to the first grating **C**. The dispersed light from **C** is reflected to mirror **D** and from there to the 45^0 mirror **E** which directs it via the horizontal intermediate slit **F** to the lower optical path. Here it is reflected from the 45^0 mirror **G** to the collimating mirror **H** to the second grating **I**. The grating reflects it to the focussing mirror **J** whence it travels to the mirror **K** which reflects it out of the instrument via the exit slit **L** to the cathode of the photomultiplier tube. The slits were all adjusted to 100 μm, this combination permitting the acquiring of spectra with a relatively good signal to noise ratio up to high temperatures. The wavelength range used was from 4910 to 5100 Å which was scanned with a speed of 5 Å/min, this speed being in the lower range of the 12 different scanning speeds available for this monochromator. The light leaving the spectrometer was detected by a Burle model C31034 A-02 photomultiplier tube with GaAs photocathode. This tube was placed in a Products for Research (USA) housing cooled to -20 C in order to reduce the thermal noise. The photomultiplier output was fed to a PAR Model 1121 Amplifier Discrim-

the finesse better than can be achieved manually.

The Sandercock tandem interferometer requires a more sophisticated form of dynamic control in order to maintain both parallel alignment of the mirrors and correct spacing. Using the same principle of comparison of two different scans as in the case of the Burleigh interferometer, but more advanced circuitry, four successive scans should be required in order to obtain error and correction signals for the two axes X and Y to maintain parallelism in a single interferometer which operates using only one piezoelectric scanning transducer and a compound translation stage. The means by which this is achieved is described at length by Sandercock (1976).

The Sandercock tandem interferometer system requires many more scans in order to obtain correction signals because now correct alignment involves adjustments about 5 axes, namely X_1, Y_1, X_2, Y_2 and ΔZ. Of these alignments the ΔZ axis which is the synchronisation axis, is the most critical and so proportionately more time is spent on stabilising this axis. The scheme employed in the Interferometer Control Unit (ICU) uses a cycle of 16 scans to achieve axis stabilisation. If stabilisation of some axes is not required it is possible to shorten the stabilisation cycle to fewer scans (Sandercock, 1994). A Z stabilizer is also employed by the ICU in order to maintain a peak at the midpoint of the scan.

normally $2\Delta N$ encompasses approximately the full width of half intensity of the reference spectral line. Ignoring statistical fluctuations inherent to photon counting detection, the presence of more counts in register A than in register B, or vice-versa, indicates a shift of the spectral peak away from being centered exactly on channel N. Before the initiation of the next sweep a digital correction is made to the zero-level of the scaler controlling the ramp in such a way as to compensate for the drift.

The procedure used for finesse stabilization is based on the fact that the maximum transmission of a spectral line by the Fabry-Perot interferometer is related to the finesse as described by Equation 3.3. During sweeps 1, 2 and 3, 4 counts are accumulated in a register whenever the channel address lies in a window $\Delta N'$ centered on channel N. This window usually encompasses less than the halfwidth points of the reference spectral line. The smaller the window width, the more sensitive the procedure is to the finesse. On the first of two sweeps, the contents of the register are stored for the existing mirror alignment. On the next sweep one of the mirrors is tilted a small amount about one of two orthogonal axes such that the distance between the centers of the interferometer mirrors remains unchanged. A comparison via logic circuitry of the counts accumulated during the two sweeps establishes which direction for tilting about this axis will increase the number of counts in the window and therefore the peak height and finesse. Appropriate correction voltages, chosen to be smaller than the test steps, are then applied to the piezoelectric element to make a correction about this axis before the next sequence of sweeps. During the next two sweeps the alignment is tested and corrected about the other axis. This procedure not only maintains optimum finesse but also maximizes

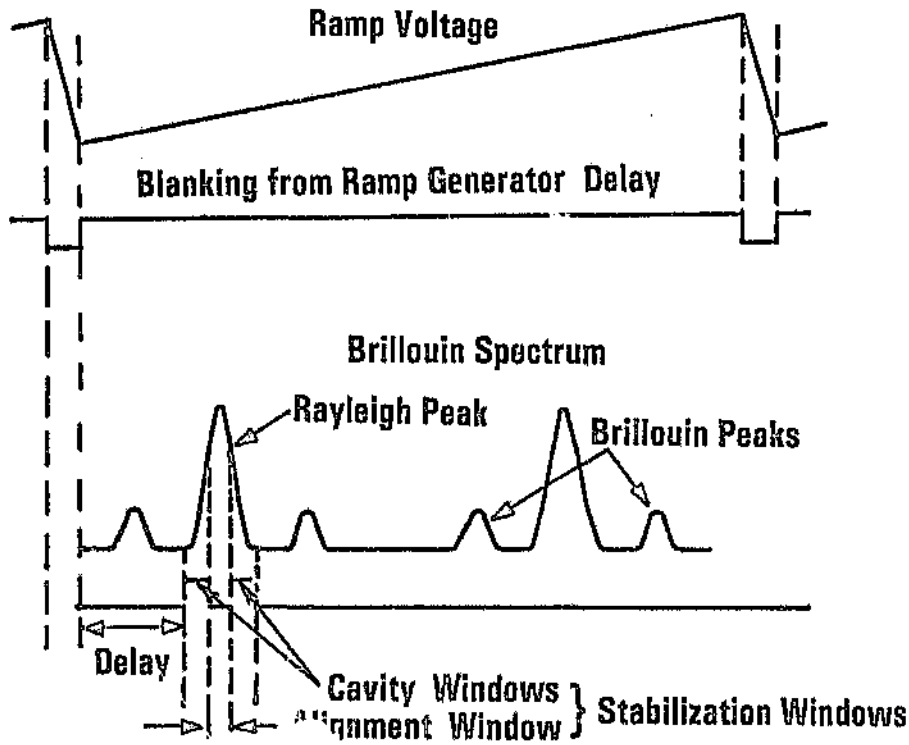

Figure 3.6: A diagram indicating the electronical procedure of acquiring a Brillouin spectrum during one scan provided by a ramp voltage.
(Courtesy of Burleigh Instruments)

In the case of the Burleigh instrument, pulses from a digital clock incorporated in a Burleigh RC 44 ramp generator are accumulated in a scalar. The scalar output is converted from digital-to-analog to produce a voltage ramp, as shown in Figure 3.6, which is applied simultaneously to the three piezoelectric elements on which one of the mirror plates is mounted. The zero-level of the scalar is controlled by drift compensation logic circuitry. The clock is also used to address sequentially the MCA channels of a 4096 channel memory via DAS-10 stabilization module. Therefore, assuming a linear relation between piezoelectric extension and applied voltage, the channel number is directly proportional to the frequency shift. The output of the photon counting apparatus is accumulated directly in the appropriate channel. Furthermore, changes in the clock rate during a sweep affect only the signal amplitude in a given section of the memory and not the frequency shift-channel number relationship. The alignment voltages applied to the three symmetrically placed piezoelectric elements are adjustable independently and controlled partially by the DAS-10 finesse stabilizer logic circuitry to optimize interferometer alignment. An oscilloscope is incorporated into the system in order to display the full spectrum as a result of applying a sawtooth scanning voltage to the interferometer. Stabilization against drift is achieved by referencing the Rayleigh scattered light as a prominent spectral feature to a selected memory channel N. This procedure actually locks the laser frequency to channel N. The spectral line is brought initially into coincidence with channel N by adjusting the zero-level of the ramp scaler. On sweeps 1, 3, 5, *etc.*, two DAS-10 digital registers accumulate counts in channel windows located from channel N-ΔN to N (register A) and from N to N+ΔN (register B). The window width is selectable digitally, and

Chapter 4

Thermal disorder in pure and doped LaF_3

4.1 Introduction

In this chapter, the onset of disorder in tysonite-structured superionic conductor with mobile fluorine ions is analysed. Pure lanthanum fluoride (LaF_3) and LaF_3 doped with BaF_2 in 2.5 and 5 mol % concentrations have been investigated. A comparative study of the effects of intrinsic and extrinsic defects on the elastic constants as determined by Brillouin scattering and on the Raman frequency shift and linewidth is conducted on these materials.

The high temperature behaviour of the measured physical properties are ex-

up in steps of 30^0 to 50^0 and stabilized for each selected temperature before collecting data. Fine adjustments of the furnace were sometimes necessary due to thermal expansion of the furnace components. Spectra were taken before and after every realignment and the evacuation of the furnace near 1000 K and checked for consistency.

The deterioration of crystal surfaces and the thermal background were the two limiting factors for these experiments. An intense Rayleigh peak appeared as a result of surfaces deterioration in the Brillouin spectrum. This can be reduced by using a gelatine filter. High quality Heraeus HLQ-210-V40 fused quartz tubes with OH-content less than 0.5 *ppm* were used for all capsules in order to minimise the high reactivity of LaF_3 with water at high temperatures.

As the thermal background was increasing when the temperature increased, a relative reduction in the intensity of the Brillouin and Raman peaks with respect to ba. ground occurred because of a decreasing in signal to noise ratio. Although the filters for Brillouin and the chopper for Raman measurements suppressed a part of the thermal background, it remained prominent at high temperatures. The collection of data was terminated when the spectrum base-line was distorted and the Brillouin and Raman pe'ks were not clearly defined.

end and so was protected from being heated significantly during the sealing. This final capsule (Fig. 3.10) was mounted in the furnace.

3.4 Experimental procedures

The experimental procedures followed in high temperature Brillouin and Raman experiments will be outlined in this section. The alignment of the sample and furnace and methods of eliminating high temperature effects will be emphasised.

Since the principal goal of the light scattering experiments was to detect changes in the frequency of the Brillouin and Raman components and the Raman linewidths, it was essential to record the spectra carefully in order to measure the frequency shifts and linewidths as accurately as possible. Accurate measurements depend on the sample alignment. In order to obtain consistent results, successive spectra were recorded for a crystal before and after encapsulation and inside the optical furnace. All these spectra need be identical. The sample was aligned in such a way that the incident and reflected laser beam co-incided on the mirror which is placed in front of the focussing lens **L1** as shown in Figures 3.1, 3.2 and 3.3.

After clamping the furnace to the table the thermocouple was mounted and the furnace was pumped down to a pressure better than 3×10^{-5} Torr and then filled with pure argon gas to a pressure of about 100 Torr. The furnace was heated

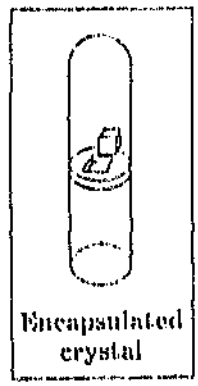

Figure 3.10: A finished capsule with a crystal next to a drilled recess

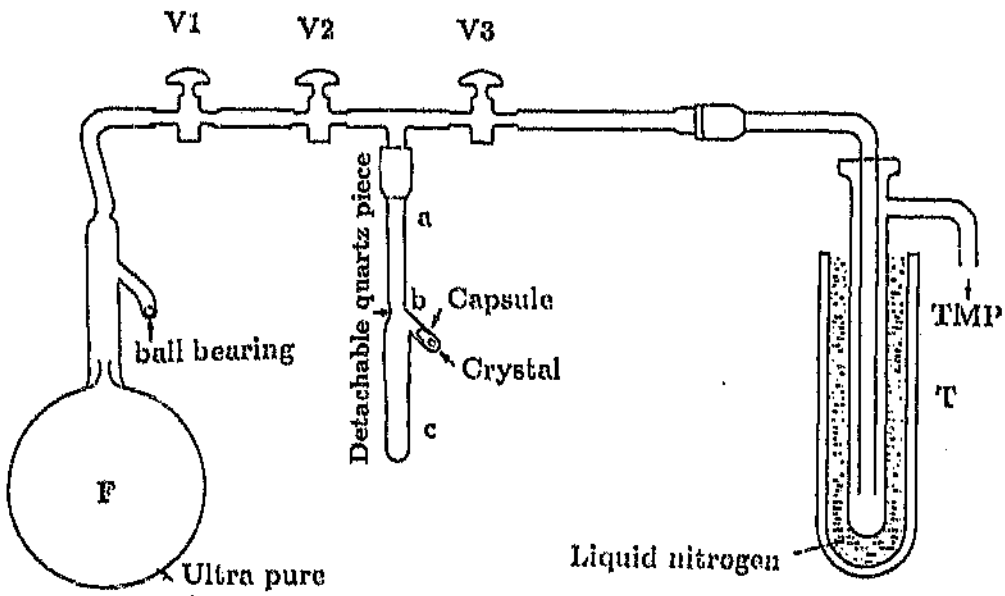

V1-V3	stopcocks		Detachable quartz piece parts:
F	argon gas flask	a	thick-walled fused quartz tube
T	liquid nitrogen trap	b	side leg
TMP	turbo molecular pump	c	10 mm fused quartz tube

Figure 3.11: Crystal encapsulation system

There are experimental problems with LaF_3 due to its reactivity with oxygen and water at high temperatures (Chadwick *et al.* 1979). In order to avoid deterioration of the sample faces, the crystals were encapsulated in fused quartz capsules filled with ultra pure argon gas. A capsule consists of a cylindrical quartz support tube of length 15 mm and diameter 8 mm. One end of the support tube was closed with a flat quartz disc and the opposite end was left open. A shallow recess was ultrasonically drilled on the flat end of this tube using a brass tool which had the dimensions of the crystal to be encapsulated. This tube is introduced together with the crystal into the side leg of the special quartz piece especially designed for this operation (Figure 3.11). Prior to this, all the quartz parts were cleaned ultrasonically in de-ionized water and pure alcohol.

An outline of the entire encapsulation system is presented in Figure 3.11. The system was evacuated by a Pfeiffer turbo-molecular pumping station type TV 250 which had the advantage of ultra clean operation. A vacuum of $3x10^{-6}$ Torr was obtained with all stopcocks opened and after that the capsule system was filled with ultra high purity argon gas from the flask. The pressure inside the capsule was calculated to be atmospheric at 2000 K which is above the highest temperature achieved in this experiment. The detachable quartz part was then sealed at the point where it was necked down. The crystal and the support tube were gently pushed back to the 10 mm OD quartz tube of the special quartz piece. The final sealing of these tubes was done in the Glassblowing Department using a special technique which allows cooling of one end of the outside quartz tube by fitting this end in a copper cup and shaft which was immersed in liquid nitrogen. The crystal was kept at this cooled

mounted on the saw goniometer with one orientated face secured to the supporting plate. The remaining two pairs of faces were chosen to be perpendicular to the directions [110] and [1$\bar{1}$0] as explained in Chapter 4. For this reason, Laue back-reflection pictures were taken to identify one of the two high symmetry spots, i.e. (100) or (010). Once a high symmetry spot was found, the crystal was rotated by 90^0 in order to find the second high symmetry spot. Only after that, the crystal was rotated by 45^0 and cut perpendicular to this direction. The resulting crystal had (110) and (1$\bar{1}$0) type faces. The diagonals of this crystal are [100] and [010] directions. A bevel was made between 6-fold planes to identify these faces.

Samples were fixed on a horizontal plate of a three stage Anshaw model 3 goniometer which was transferred directly from the x-ray track to an Anshaw model 7 saw. This saw makes vertical cuts on the sample. In order to correct small misorientations of crystal faces after cutting, a two stage Polaroid goniometer was necessary to be used. Crystal polishing is essential in order to make crystals transparent to the laser beam and to minimise parasitic light scattering. Emery paper (400, 600, 800, 1000, 1200) was employed for hand polishing. Medicinal paraffin was used as lubricant between the crystal and the paper. Kent Mark II and Mark III automatic polishing machines were used for the final polishing. A special polishing pad, 6 μ Hyprez diamond polishing spray and Hyprez polishing lubricant were employed as abrasive. Alcohol of purity 9.1 % was used to clean the crystal between these successive operations. The final cleaning was done by slowly boiling the crystal in methylated spirit and after that leaving the crystal in a bath of 99 % pure alcohol for ultrasonic cleaning.

tube operated at 35 kV and 20 mA was employed to obtain an x-ray beam. Agfa x-ray film was used to detect the Laue spots. The exposure times were between 3 and 5 hours. In order to facilitate a good alignment of the crystal with the x-ray beam, a fluorescent screen was used to convert the x-rays to visible light.

A hexagonal LaF_3 crystal with a random orientation was mounted on a flat plate of the Anshaw goniometer using Cottrell dentistry modelling wax. The heating was made slowly during the mounting procedure to prevent the crystal from being shocked thermally. The arcs of the goniometer were set at 0^0. The goniometer was then attached to the mounting track on the Philips x-ray generator. A Laue back-reflection picture was taken. The six-fold direction was identified first by the appearance of the x-ray picture which must contain 6 adjacent axes separated by 60^0, in accordance with the standard stereographic projection.

For all the crystals used in this study, the top and the bottom faces were planes cut perpendicular to the 6-fold axis. Once these faces were identified and cut, they were checked for misorientation which usually had occurred during cutting. Brass correction rods were used in order to rectify slight misorientations. The rods were machined such that the inclinations of lower ends were between 1^0 and 3.5^0 with increments of 0.5^0. If the face orientation was correct the sample was polished directly on the rod. The final face orientation is accurate to 0.5^0.

To determine the orientation of the next pair of faces, the sample was re-

3.3 Crystal preparation

As was presented in Chapter 2, the phonon propagation direction must be known precisely in order to conduct Brillouin scattering measurements. This is not as important for the Raman experiments. The technique used to prepare an encapsulated and orientated crystal sample for Brillouin and Raman experiments will be outlined in this section.

The present samples used for Brillouin and Raman scattering were prepared in the form of oriented parallelepipeds. For Brillouin scattering the phonon propagation directions are the diagonals of these bodies.

The back reflection Laue x-ray method was used for the orientation of the crystals in the present work. This method uses a "white" beam of x-rays to obtain diffraction maxima (spots) from a single crystal placed behind a flat photographic film. This technique enables one to determine the required crystallographic direction for a given unoriented crystal. The technique is most efficient for determining the orientation of cubic crystals; hexagonal crystal systems give more complex patterns and relationships between interplanar angles and Miller indices. Thus, the task of finding the orientation of the main crystallographic axes is not straightforward. The vertical and horizontal deviations of the Laue spot from the center of x-ray picture were determined by the polar angles θ and δ of the spots which were calculated from the Cartesian coordinates (x,y) according to Preuss (1979).

A Philips generator model PW 1008 using a conventional molybdenum target

rent transformer. An RKC Proportional, Integral and Derivative temperature controller model PF-62 was used to stabilize automatically a preset temperature to better than ± 1 K. An important advantage of this system is that large current changes can be preprogrammed to occur slowly and so thermal shocks are avoided through the low resistance furnace element.

To ensure temperature homogeneity in the sample region the furnace is backfilled with pure argon to a pressure of 34.5 kPa (259 Torr). This provides efficient heat transfer between furnace element and crystal capsule at temperatures $T \leq 1000$ K. Above 1000 K where radiative heat transfer becomes very efficient the furnace is evacuated completely. The vacuum inside the furnace is kept around 4×10^{-4} Torr by a combination of an Edwards diffusion pump and a two-stage Edwards rotary pump via a 2 m long flexible metal tube. A special gas supply system was used in connection with the pumps to evacuate the furnace and fill it with the pure argon gas from a low pressure reservoir through a needle valve in order to avoid over-pressurization.

The central core of the furnace is an alumina tube **D** (3.2 cm x 11 cm) around which the heater wire is wound inside a spiral groove 0.6 mm deep and with a 2 mm pitch; the resulting heater coil has 40 turns with a total wire length about 4 m. Molybdenum 99.99 % purity wire was used with a diameter of 0.25 mm and resistance about 7 Ω at room temperature. Radiation losses are minimised by shielding the heating element. The furnace tube is surrounded by two coaxial cylindrical radiation shields **F** and **H** made of tantalum foil with the apertures determined by the solid angle requirements of the external optics. Support for the shields is provided by two pairs of alumina discs **E** and **G** such that the ends of the tube and shields fit firmly. Holes **H2** in this tube accommodate the sample capsule. This heating element is supported by a water-cooled brass flange **N** which is O-ring-sealed to the quartz cylinder **K**. The flange carries pumping ports **Q** and electrical leadthroughs **P** via glass to metal seals.

Sample temperature was monitored by a platinum-platinum 13% rhodium thermocouple with the junction placed immediate next to the encapsulated crystal. It is led through double-hole alumina tubing which is sealed with an O-ring to the concentric alumina tube **L** of the furnace element.

At the elevated temperatures reached, radiation is the major source of heat loss and so the shielding is the limiting factor of the design. Nevertheless, this furnace operated at temperatures up to 1500 K during the Brillouin experiments, and 1400 K during the Raman measurements, respectively.

The furnace is powered by AC currents up to 4 A supplied through a heavy cur-

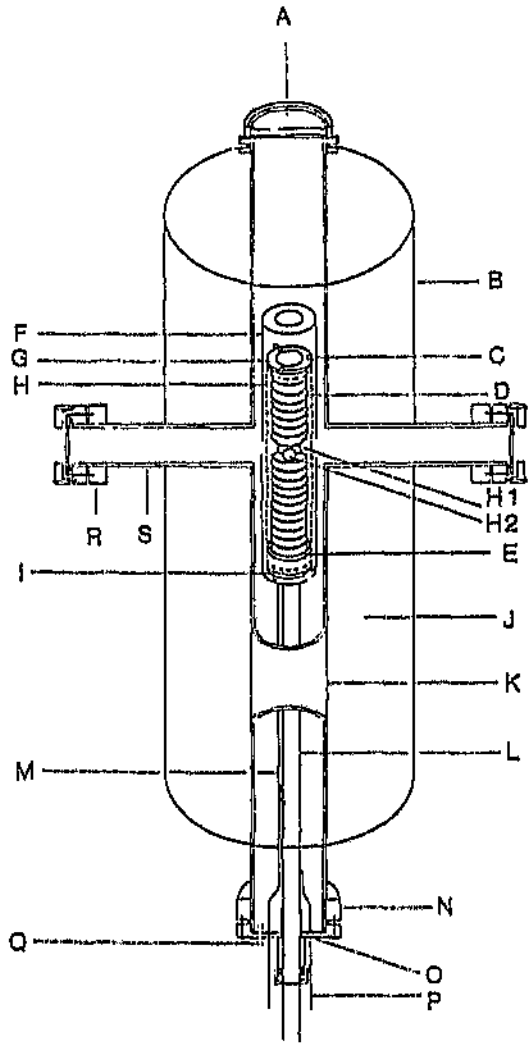

A	large end window	**J**	Kao wool
B	outer stainless steel casing	**K**	thick-walled quartz tube
C	bisected piece of alumina rod	**L**	hollow alumina tube
D	molybdenum heating element and hollow alumina tube	**M**	dual hole alumina guide for molybdenum heating element
E	back alumina disc	**N**	water cooled back flange
F	outer tantalum radiation shield	**O**	glass to metal seal
G	front alumina disc	**P**	lead for the heating element
H	inner tantalum radiation shield	**Q**	vacuum pumping port
H1	holes for the passage of light	**R**	side window mount
H2	holes to accommodate a capsule	**S**	side arm of the quartz tube
I	sliding alumina disc		

Figure 3.9: Vacuum optical furnace

3.2 Vacuum optical furnace

A special furnace was employed in order to conduct light scattering experiments at high-temperature. This furnace is similar to that described by Harley *et al.* (1978) and Ngoepe (1987). The furnace is evacuable and allows for back-filling with argon gas. All windows can be removed for cleaning. Figure 3.9 shows the essential features of the furnace. The inner quartz cylinder **K** (5.5 cm x 33 cm) and the side-arms **S** (2 cm x 8 cm) form a cross-piece. Fused quartz windows are sealed with rubber O-rings in brass mounts **R** which also carry O-ring seals to the quartz tube. Air cooling for the side-arms was sufficient to prevent deterioration of the O-rings, but the large end window **A** requires water cooling. The inner quartz tube is surrounded with Kao insulating wool **J** and contained in a stainless steel cylinder **B** of 13 cm diameter. The steel container did not require water cooling. The whole assembly was held by two brass collars with brass rods which fit in short cylinders mounted on steel plates. The rods are threaded to allow for the vertical adjustment of the furnace. The base plate assembly provides fine horizontal adjustments along and orthogonal to the length of the furnace. All moving parts of this system may be locked into position. In the normal mode of operation the laser beam is incident through a side-arm window **R** and scattered light is collected through the large end window **A**.

The principle of operation is to produce direct radiative heating of the sample in order to increase the temperature, and to minimise temperature gradients by placing the sample in the interior of the heating coil.

Measurement of Brillouin spect a

Due to inhomogeneity caused by doping, there was very intense elastically scattered light from the doped crystals. Using the Burleigh 3-pass FPI discussed in section 3.1, it was possible to collect Brillouin spectra at high temperature only for LaF_3 (2.5 % mol BaF_2). In order to observe the extremely weak Brillouin signals from these crystals, the Sandercock tandem interferometer (section 3.1) with a contrast of 10^{12} was employed. Using this instrument, two runs on LaF_3 doped with 2.5 and 5 mol % BaF_2 were performed. The two runs on LaF_3 (2.5 mol % BaF_2) using the different interferometers gave similar results. A 90^0 scattering geometry was used for all these measurements.

As described in Chapter 3, the encapsulated crystals were placed in the optical furnace and aligned using the same procedure for both interferometers.

In the case of LaF_3 (2.5 mol % BaF_2), free spectral range of 54.18 GHz was found adequate for the measurement of the frequency shifts along the [100] phonon propagation direction, using the Burleigh interferometer. For the tandem interferometer, the free spectral range was chosen to be 61.47 GHz.

The 514.5 nm laser line was used to excite the Brillouin spectra obtained f om the tandem interferometer, the 488 nm laser line being used for the same purpose with the Burleigh interferometer. Laser output powers of approximately 500 mW were found to be adequate for LaF_3 (2.5 mol % BaF_2) on the Burleigh interferometer, while approximately 250 mW was sufficient using the Sandercock tandem instrument.

4.3.2 High temperature studies using Brillouin scattering

In this section detailed experimental procedures followed in the Brillouin study of the doped LaF_3 crystals are outlined.

Birefringence aspects of Brillouin scattering

The birefringence of uniaxial crystals is a well-known aspect of the theory of light. The splitting of the refracted ray into ordinary and extra-ordinary rays change the Brillouin spectrum; each Brillouin scattered component can be split into four lines (Chandrasekharan 1965).

It was shown by Keller and Sondergaard (1974) that in hexagonal crystals no effects of birefringence are observed in a plane perpendicular to the c-axis [001], while in a plane containing c-axis this effect is very strong for crystals with large differences in refractive indices.

Previous Brillouin studies (Lailho *et al.* 1983a, Ngoepe *et al.* 1986, Mjwara *et al.* 1991) have shown that in practice no splitting of the Brillouin components could be observed for light lanthanide trifluorides. This optical isotropy was expected since the refractive indices n_o and n_e differ by only 0.44 % (Lailho *et al.* 1983b).

faces oriented parallel with the principal crystallographic planes (100), (010), (001) and was used only for Raman measurements. The base of this sample was chosen to be a plane perpendicular to the c axis [001].

Two crystals of LaF_3 (2.5 mol % BaF_2) and one of LaF_3 (5 mol % BaF_2) were cut with the intention of extracting C_{11} elastic constants. The sixfold symmetry plane, normal to the c axis served as the bases of these samples. For this case, in the scattering plane, phonon propagation directions [100] and [010] are equivalent. To obtain these propagation directions, the two pairs of side faces were cut perpendicular to the directions $[110]/\sqrt{2}$ and $[110]/\sqrt{2}$.

All the oriented crystals were polished into cubes with average dimensions of 3 x 3 x 3 mm and subsequently encapsulated in high purity, OH free, silica capsules in which the oriented crystal was inserted in a matched recess drilled in the capsule base as shown in Figure 3.9.

data, it was shown that a divalent cationic dopant (e.g. BaF_2) appears to increase, and a tetravalent cationic dopant (e.g. ThF_4) appears to decrease the ionic conductivity of LaF_3 and CeF_3 with respect to the nominally pure materials (Roos *et al.* 1984c, Takahashi *et al.* 1977).

4.3 Experimental procedures

In this section specific aspects pertaining to the preparation of the pure and doped LaF_3 crystals for the Brillouin and Raman experiments will be discussed. Some aspects of crystal preparation and the analysis of the Brillouin and Raman spectra were described in detail in chapters 2 and 3 and will be referred to as appropriate.

4.3.1 Crystal preparation

Four crystals were prepared in order to carry out Brillouin and Raman measurements. A high purity LaF_3 crystal boule with a random orientation was bought from Atomergic Chemetal Corp (USA), being the same as that used by Ngoepe *et al.* (1986) to produce samples for their Brillouin scattering studies. LaF_3 crystals doped with BaF_2 in 2 different concentrations (2.5 and 5 mol %) were obtained from Prof. A.V. Chadwick from University of Kent (UK).

The pure LaF_3 sample was prepared in the form of a parallelepiped with the

that of Goldman and Shen (1966) where the ratio of fast to slow moving ions was 2:1.

Aalders *et al.* (1983) and Roos *et al.* (1984) proposed another model in which at low temperatures anion vacancies preferentially reside on the B sublattice where they exhibit the faster motion in the c direction. Thus the ratio of sites allowing fast motion to those involved in the slower migration is 1:2. It is only above 400 K that vacancies start to populate the A sublattice. This model was invalidated by the computer simulation of Jordan and Catlow which shows that on average the jumps with the lowest activation energies are nearest neighbour $\alpha \longrightarrow \alpha$ jumps in the a - b plane.

Following the recent work using computational simulation of ion transport in pure LaF_3 (Jordan and Catlow 1987) it was shown that the formation energy for Frenkel defects is lower than for Schottky defects at temperatures below 1000 K. These results together with the computational simulations of the elastic constants obtained from Brillouin scattering studies (Ngoepe *et al.* 1990) are consistent with assuming that an estimated 2 mole % Frenkel disorder occurs on the fluorine sublattice in the superionic phase. However, the presence of limited Schottky disorder cannot be ruled out on the basis of lattice parameter and dilatation results (Sher *et al.* 1966).

In previous models (Sher *et al.* 1965, Chadwick *et al.* 1979), the mechanism of disorder in pure LaF_3 was based on the generation of Schottky defects. For doped fluorides with a tysonite structure Roos *et al.* (1984c) suggested the same Schottky vacancy mechanism for anion conduction. From experimental

evidence ...ning the detailed mechanisms.

Whatever model or technique was involved, at ambient temperature the conductivity parallel to the c-axis was found to be twice as large as the conductivity perpendicular to it (Chadwick *et al.* 1979, Schoonman *et al.* 1980). This anisotropy reduced from 2 at room temperature to 1.4 at 650 K.

The ionic conductivity is affected by the motion of fluorine vacancies. The possible F^- motions are described in Table 4.2 and illustrated in Figure 4.2.

Nearest neighbour jumps of ≈ 2.7 Å involve $\alpha \longleftrightarrow \alpha$, $\alpha \leftrightarrow \beta$ and $\alpha \longleftrightarrow \gamma$ motions and are predominantly in the a-b plane with a small component in the c direction. A second $\alpha \longleftrightarrow \alpha$ type motion of ≈ 2.5 Å is a single jump along the c direction, further motion being blocked by the presence of lanthanum ions. Continuous motion in the c direction can, however, be achieved by $\beta \longleftrightarrow \beta$ or $\gamma \longleftrightarrow \gamma$ motions of ≈ 3.7 Å. These are the most probable types of jumps and have been the subject of numerous studies.

Chadwick *et al.* (1979) and Jaroszkiewicz and Strange (1985) using NMR and conductivity techniques established a model in which between 300-500 K the faster F^- migration occurs in the a - b plane between sites on the A sublattice. According to this model, an activation energy of 0.27 eV was measured, which was in good agreement with that determined from conductivity data, namely 0.28 eV. NMR data show that the exchange between A and B sites was slow enough to allow the two species to be distinguished until higher temperatures when the exchange become too rapid. This model is in good agreement with

Elastic Constants	C_{11}	C_{12}	C_{13}
Laiho *et al.* 1983a	180 GPa	88 GPa	59 GPa
	C_{14}	C_{33}	C_{44}
	0.5 GPa	222 GPa	34 GPa
Phonon velocities	$v_{[100]}$	$v_{[010]}$	
Krescher 1968	$2788 \pm 2\ m/s$	$2785 \pm 2\ m/s$	
Laiho *et al.* 1983a	$2784 \pm 3\ m/s$	$2783 \pm 3\ m/s$	
Refractive indices	n_o	n_e	
Laiho *et al.* 1983b	1.6073	1.6002	
Lattice parameters	a	c	
Mansmann 1965	7.190 Å	7.367 Å	
Density	$5940\ kg/m^3$		
Melting temperature	1493 K		

Table 4.1: Properties of LaF_3

Sites	Distance Å	Saddle point energy (eV)	E_{Act} (eV)
$\beta \leftrightarrow \beta$ $\uparrow c$	3.68	4.68	1.41
$\gamma \leftrightarrow \gamma$ $\uparrow c$	3.68	5.24	2.26
$\beta \leftrightarrow \beta$ (a-b)	4.15	7.05	3.78
$\gamma \leftrightarrow \gamma$ (a-b)	7.14	5.72	2.74
$\alpha \leftrightarrow \alpha'$ $\uparrow c$	2.56	2.59	~ 0
$\alpha \leftrightarrow \alpha'$	2.73	2.68	0.08
$\alpha \leftrightarrow \alpha'$	2.70	2.72	0.12
$\beta \leftrightarrow \alpha$	2.78	3.26	~ 0
$\alpha \leftrightarrow \beta$			0.66
$\beta \leftrightarrow \alpha'$	2.70	3.27	~ 0
$\alpha' \leftrightarrow \beta$			0.67
$\beta \leftrightarrow \gamma$	4.22	6.81	3.54
$\gamma \leftrightarrow \beta$			3.83
$\gamma \leftrightarrow \alpha$	2.81	3.45	0.47
$\alpha \leftrightarrow \gamma$			0.85
$\gamma \leftrightarrow \alpha$	2.71	3.04	0.06
$\alpha \leftrightarrow \gamma$			0.44
$\gamma \leftrightarrow \alpha'$	2.77	3.30	0.32
$\alpha' \leftrightarrow \gamma$			0.70

Table 4.2: Migration energies (After Jordan and Catlow 1987)

this model there are two kinds of fluorine ions: some of them lie in the La-F layers (β and γ), and the remainder lie between the La-F layers (α). This structure can be approximated by two sublattices A and B with multiplicities 12 and 6, because the β and γ sublattices are not easily distinguishable. A is identified with the α-sublattice and B with β- and γ- sublattices together. In this model the A fluorines can move predominantly in the (a-b) plane while B fluorines can move perpendicular to this. There is ample scope for exchange between these two sublattices.

In determining the elastic properties for the purpose of this work, the hexagonal approximation to the trigonal structure is sufficient because in previous ultrasonic (Krischer 1968) and Brillouin scattering studies of LaF_3 (Laiho *et al.* 1983a, Ngoepe *et al.* 1986), CeF_3 (Ngoepe and Comins 1988), and NdF_3 (Mjwara *et al.* 1991) it was found that the elastic constant $C_{14} \simeq 0$, and the velocity of acoustic phonons is virtually constant in a plane perpendicular to the optic axis, i.e. the x-y plane. The properties of LaF_3 are presented in Table 4.1.

4.2.2 Transport properties

The conductivity properties of tysonite materials are rather complex and in some respects an open problem. LaF_3 is one of the first crystals identified as showing transport between inequivalent lattice sites. Interpretation of transport data is, however, the subject of debate, with conflicting experimental

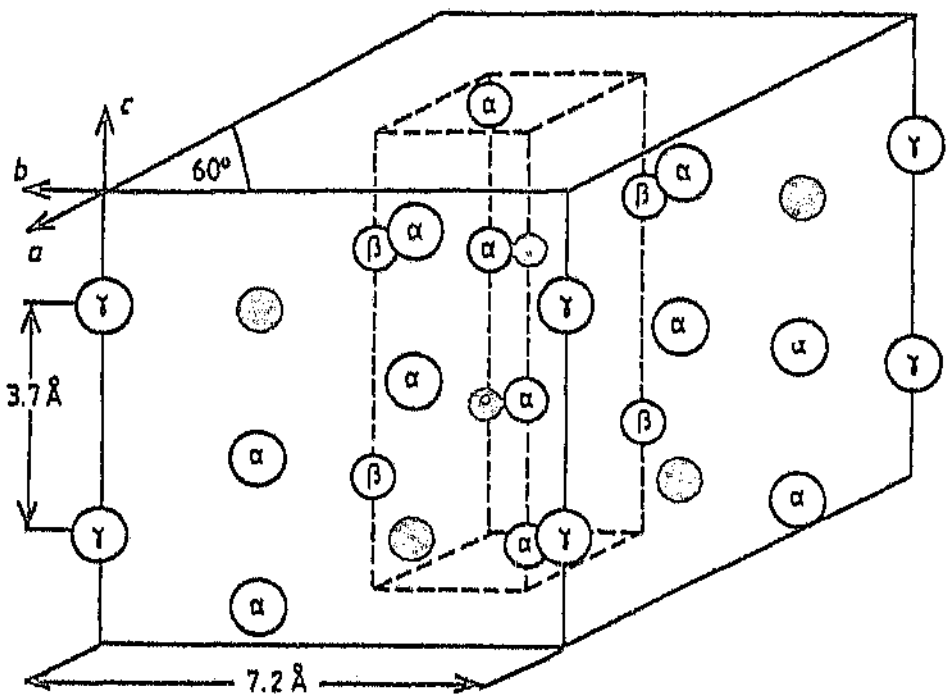

Figure 4.2: Simplified structure of LaF_3 (After Jaroszkiewicz and Strange 1985)

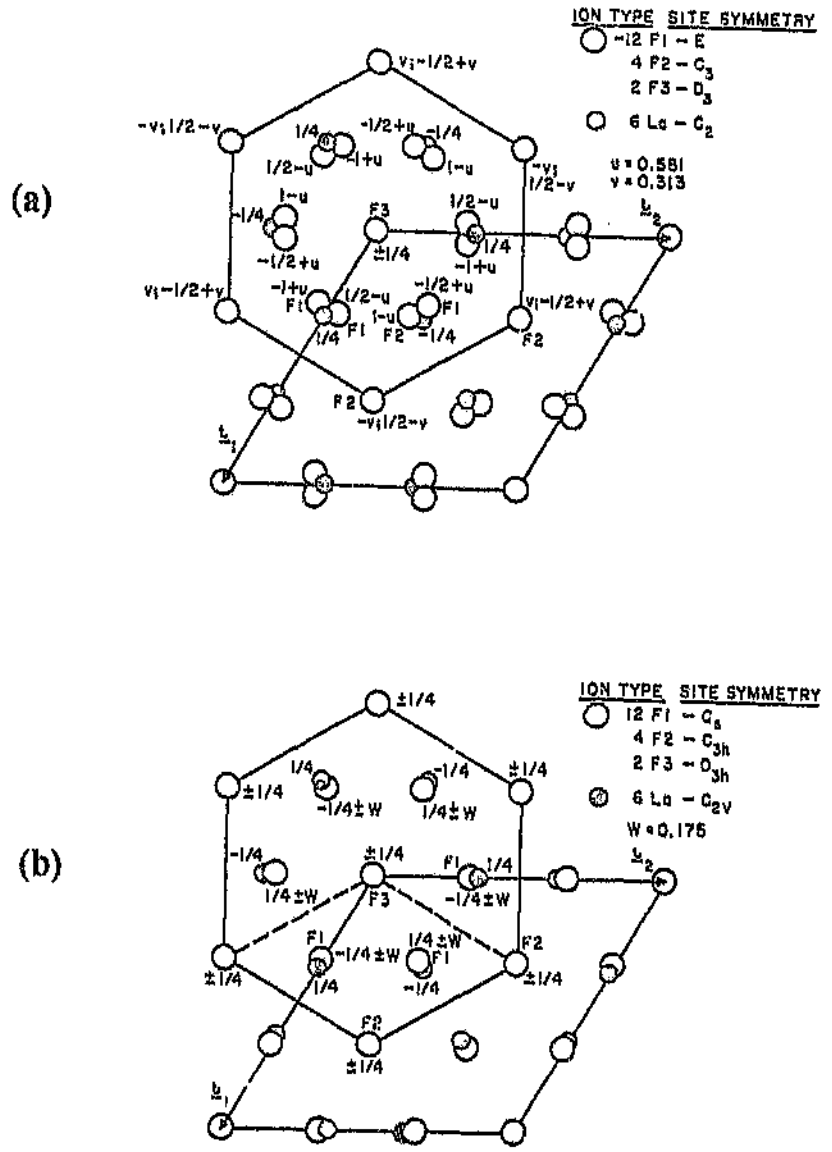

Figure 4.1: Possible LaF_3 hexagonal cells: (a) P$\bar{3}$c1 crystal structure of LaF_3. (b) P6_3cm crystal structure of LaF_3. The projection of particles in the hexagonal cell are shown on the plane perpendicular to crystal c axis and passing through the origin. (After Rast *et al.* 1968)

Excess specific heat capacity measurements have been conducted on LaF_3 by Spedding *et al.* (1974) and Lyon *et al.* (1978). Above 1150 K there is a substantial increase in C_p which is very well correlated with reduction in elastic constants measured using Brillouin scattering. It is noted that the heat capacity of LaF_3 is much higher than that reported for CeF_3, PrF_3, and NdF_3 and their temperatures of onset are less well defined (Lyon *et al.* 1978).

At this moment, it seems reasonable to attribute this diffuse transition to the generation of anion Frenkel disorder on one of the fluorine sublattices as will be outlined in the following sections.

4.2.1 Structural properties

LaF_3 is representative of the ionic trivalent halides with the tysonite structure. This structure has been the subject of much controversy, with different space groups being predicted, the most probable being $P\bar{3}c1$ or $P6_3cm$. Whichever of these is used, the structure is heximolecular with six formula units per unit cell as shown in Figure 4.1.

At this moment, however, from crystallographic (Mansman 1965, Zalkin *et al.* 1966, Cheetham *et al.* 1976), Raman (Bauman and Porto 1967) and NMR (Goldman and Shen 1966, Jaroszkiewicz and Strange 1985) data from LaF_3, CeF_3, NdF_3 and PrF_3 the experimental evidence favours the trigonal structure $P\bar{3}c1$. In essence, $P\bar{3}c1$ is characterized by three fluorine sublattices α, β, and γ with site multiplicities 12, 4 and 2 per unit cell, respectively (Figure 4.2). In

plained in terms of current theories. These models are based on NMR, static lattice computer simulations, Brillouin, Raman and ionic conductivity studies.

4.2 Literature review on LaF_3

Lanthanum fluoride has been the subject of many studies during the last 25 years. The reason for such prolonged investigations, apart from the potential technological applications already mentioned in Chapter 1, is disagreement concerning the crystalline structure and the mechanism of ionic conductivity which appears even at ambient temperature (*Gmelin Handbuch der Anorganischen Chemie* 1976).

A great deal of information is already available on structure, transport and defect properties of pure and doped LaF_3 and will be briefly reviewed.

According to previous measurements of elastic constants and refractive index (Laiho *et al.* 1983a, 1983b) of the tysonite series LaF_3, CeF_3, PrF_3, NdF_3, one can conclude that there is a great similarity in the optical and elastic properties of these compounds.

Recent Brillouin scattering (Ngoepe *et al.* 1986, Mjwara *et al.* 1991), computational modelling (Jordan and Catlow 1987) and a combination of these techniques (Ngoepe *et al.* 1990) have identified a diffuse phase transition above 1100 K in these kinds of materials.

compared with the pure LaF_3 (T_C=1150 K) is remarkably large.

Figure 4.8 shows the results for C_{11} as a function of temperature in LaF_3 (5 mol % BaF_2). For this crystal T_C is 750 K and the quasi-linear reduction in C_{11} appears below and above T_C, this behaviour being in good agreement with the quasi-harmonic theory of Garber and Granato (1975).

In the case of LaF_3 (5 mol % BaF_2) the final temperature reached (1519 K) was higher than the melting temperature (1493 K) of pure LaF_3, but less than T_M for BaF_2 (1553 K). No melting phenomena were observed which itself is remarkable taking into account the small concentration of BaF_2 dopant.

The temperatures at which substantial changes in the linewidth occur will be discussed in the following sections in relation to the Raman scattering studies.

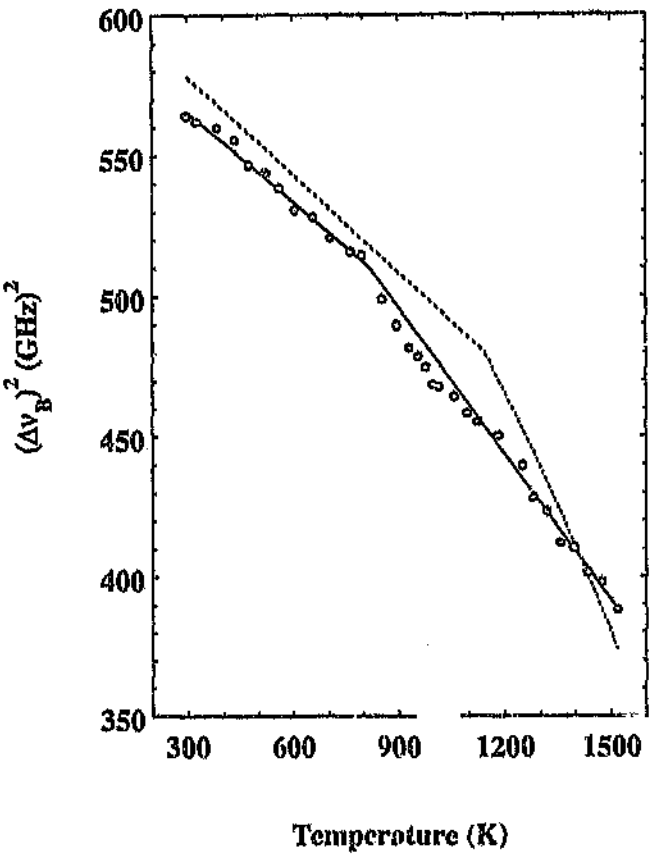

Figure 4.8: The behaviour of C_{11} as a function of temperature for LaF_3 (5 mol % BaF_2). The dashed line represents a fit of C_{11} according to the experimental data of Ngoepe *et al.* 1986.

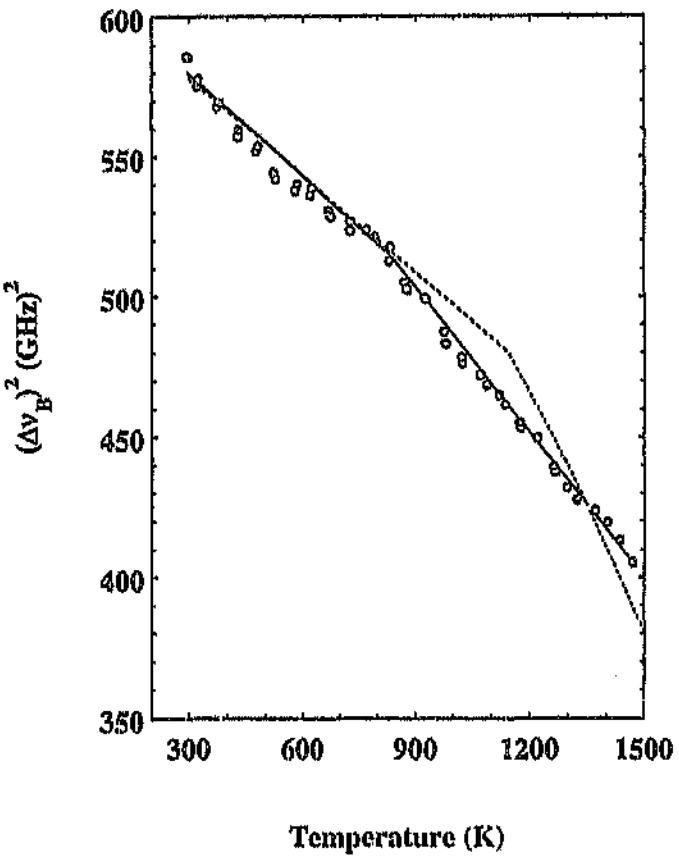

Figure 4.7: The behaviour of C_{11} as a function of temperature for LaF_3 (2.5 mol % BaF_2). The solid circles are results obtained using the Burleigh interferometer and the circle are results using the Sandercock interferometer.The dashed line represents a fit of C_{11} according to the experimental data of Ngoepe *et al.* 1986.

Since the task of these Brillouin experiments was to measure only the elastic constants, the peak positions were important and not their intensities. Basically, Brillouin peaks increase in the intensity with the temperature; this normal pattern was altered in Figures 4.5 and 4.6 by using different accumulation times.

The slight asymmetry which appears in the Rayleigh peaks of LaF_3 (5 mol % BaF_2) spectra occurred because the window which had defined the Rayleigh peak position during the interferometer scan was not centered exactly on this peak. As already explained in Section 3.1 this has no effect on the Brillouin peak positions.

Figure 4.7 shows the square of the Brillouin frequency shift $(\Delta\nu_B)^2$ as a function of temperature for LaF_3 (2.5 mol % BaF_2). On the assumption that ρ/n^2 is constant, the results indicate the behaviour of the elastic constant C_{11}. These results show a decrease of C_{11} with temperature from 300 K to 880 K. A slight departure from the theoretically predicted quasi-linear decrease with temperature (Garber and Granato, 1975) is present in this range and is not explained by the present theories. For this crystal, a slight curvature is observed for the Raman FWHM in the same temperature range and will be analysed after the discussion of the Raman results.

Above 880 K a substantial quasi-linear decrease in C_{11} occurs which continues until 1471 K, the final measured temperature. It is customary in the case of Brillouin scattering experiments (Comins *et al.* 1990) to label T_c the transition temperature at which the decreasing of C_{11} occurs. Taking into account the relatively small concentration of BaF_2, the reduction of 300 K in T_c as

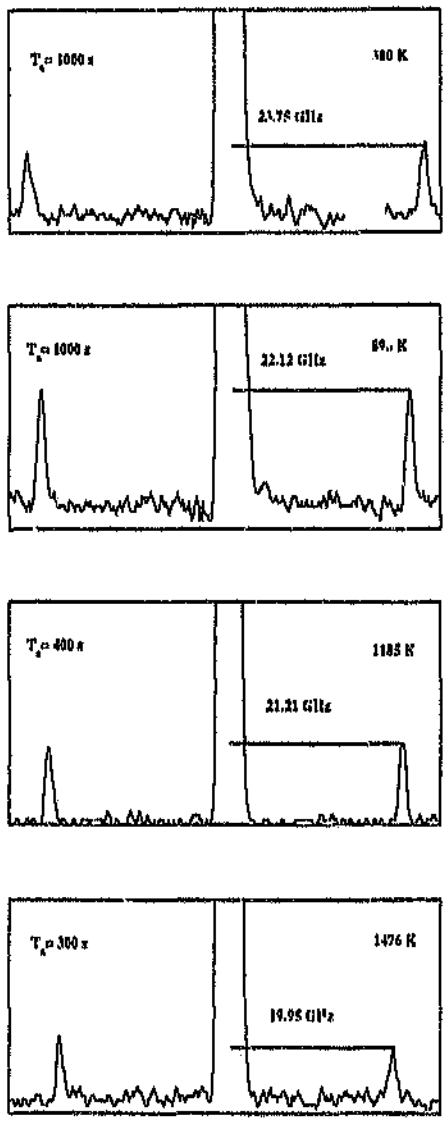

Figure 4.6: Brillouin spectra of LaF_3 (5 mol % BaF_2) at various temperatures, in the [100] phonon propagation direction.T_a refers to the accumulation time.

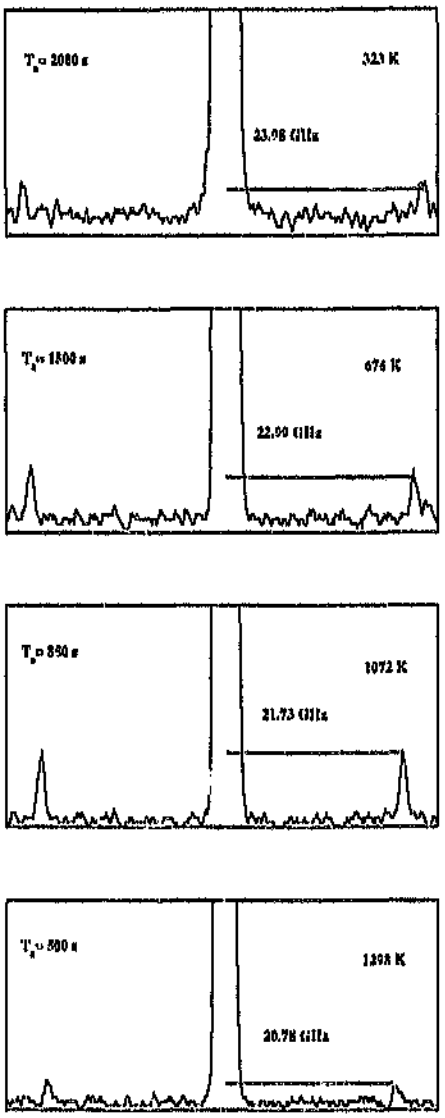

Figure 4.5: Brillouin spectra of LaF_3 (2.5 mol % BaF_2) at various temperatures, in the [100] phonon propagation direction. T_a refers to the accumulation time. Spectra were taken using the Sandercock tandem interferometer.

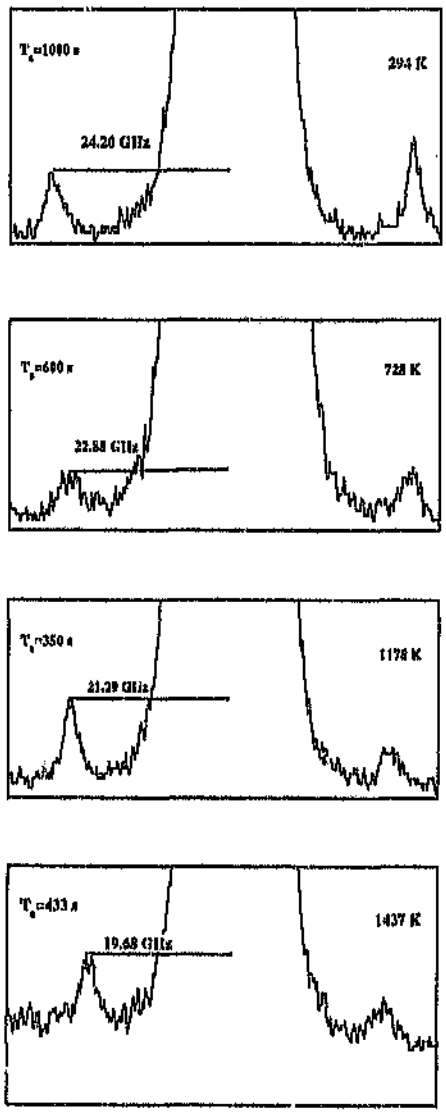

Figure 4.4: Brillouin spectra of LaF_3 (2.5 mol % BaF_2) at various temperatures, in the [100] phonon propagation direction. T_a refers to the accumulation time. Spectra were taken using the Burleigh interferometer.

the scattering geometries characteristic to the present experiment as shown in Figure 4.3.

The Brillouin tensors appropriate to this experiment were obtained from Cummins and Schoen (1972) and Vacher and Boyer (1972) and are shown in Table 4.3. The Rayleigh ratios calculated using equation 2.21 are shown in Table 4.4. The Brillouin peaks were assigned using these results and were consistent with the previous results of Ngoepe *et al.* (1986, 1990) on pure LaF_3.

4.3.3 Results and discussion

Typical Brillouin spectra at different temperatures for 2.5 and 5 mol % BaF_2 dopant concentrations are presented in Figures 4.4-4.6 to illustrate their characteristic features.

In the [100] phonon propagation direction, although only one peak was observed, the Rayleigh ratios in Table 4.4 suggest that 2 peaks are expected. The transverse peak in this direction is extremely weak and was not observed. The only measured peak is associated with the elastic constant C_{11}.

A comparison of Figure 4.4 and 4.5 shows the advantage of using the Sandercock interferometer which has a much higher contrast ($\approx 10^{12}$). As is shown in Figure 4.5 and 4.6, the Brillouin peaks are narrower and much better resolved. The same particularities are noted for the Rayleigh peaks.

$\hat{\mathbf{K}}$=[100]

L: $\hat{u}$=[100] ; $\rho v^2 = C_{11}$ $\mathbf{T}^{(1)} = \begin{pmatrix} \epsilon_0^2 p_{11} & 0 & 0 \\ 0 & \epsilon_0^2 p_{12} & 0 \\ 0 & 0 & \epsilon_e^2 p_{31} \end{pmatrix}$

T1: $\hat{u}$=[010] ; $\rho v^2 = C_{66}$ $\mathbf{T}^{(2)} = \begin{pmatrix} 0 & \epsilon_0^2 p_{66} & 0 \\ \epsilon_0^2 p_{66} & 0 & 0 \\ 0 & 0 & 0 \end{pmatrix}$

T2: $\hat{u}$=[001] ; $\rho v^2 = C_{44}$ $\mathbf{T}^{(3)} = \begin{pmatrix} 0 & 0 & 0 \\ 0 & 0 & \epsilon_0 \epsilon_e p_{44} \\ 0 & \epsilon_0 \epsilon_e p_{44} & 0 \end{pmatrix}$

Table 4.3: Brillouin tensors for a hexagonal crystal for phonon propagation direction [100].

$\hat{K}$:	$R_{VV}^{(1)}$	$R_{VH}^{(1)}$	$R_{VV}^{(2)}$	$R_{VH}^{(2)}$	$R_{VV}^{(3)}$	$R_{VH}^{(3)}$
[1 0 0]	$\frac{Ae_0^4 \lvert p_{11} \rvert^2}{C_{11}} (\frac{n_e}{n_0})^3$	0	0	0	0	$\frac{Ae_0^2 e_e^2 \lvert p_{44} \rvert^2}{2C_{44}} (\frac{n_e}{n_0})^2$

Table 4.4: Rayleigh ratios appropriate to this experiment

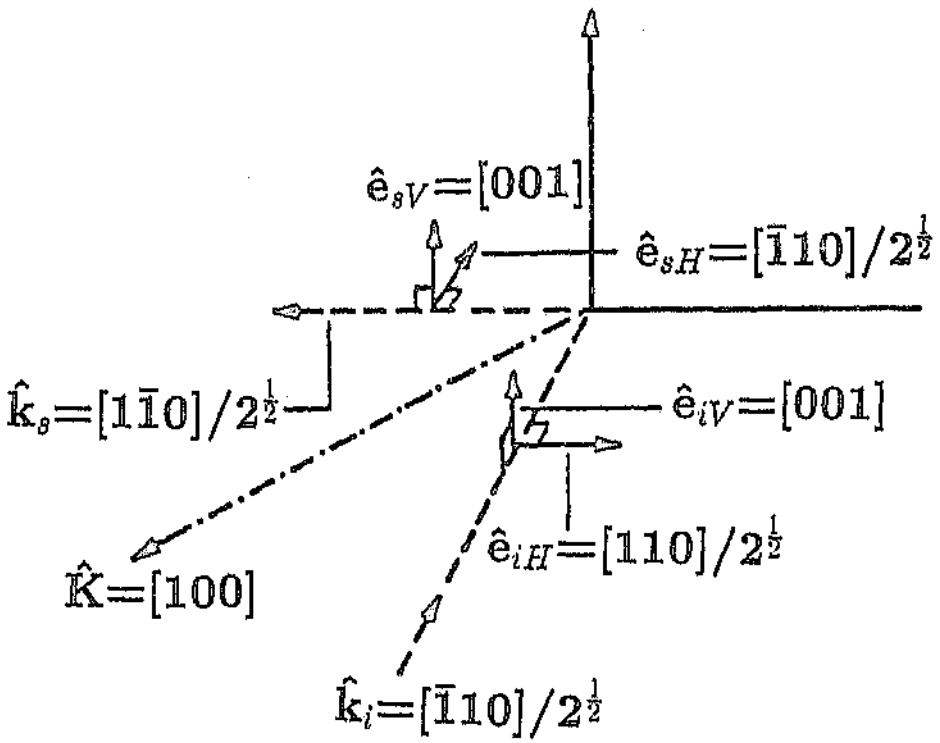

Figure 4.3: Scattering geometries for the LaF_3 samples in the [100] phonon propagation direction. $\hat{e}_{iV}$ and $\hat{e}_{sH}$ represent the polarization direction of the vertically polarized incident light and the horizontally polarized scattered light respectively. Other symbols have similar meanings. $\hat{k}_i$ is the wavevector of the incident light.

tion by the following expression:

$$\gamma_{ij} = \frac{\lambda_0^2}{4\sin^2\frac{\theta}{2}}(\Delta\nu_B)^2\frac{\rho}{n^2}. \tag{4.3}$$

Details for the particular case used in this study are presented in Figure 4.3 and Table 4.3.

The Brillouin scattering measurements were reported by determining $(\Delta\nu_B)^2$ as a function of temperature and assuming that this represents the behaviour of the appropriate elastic constant combination γ_{ij}. This is valid provided that the change in ρ/n^2 is not significant. Experimental determinations made in a few cases, e.g. Catlow *et al.* (1978) on fluorites and Botha *et al.* (1993) on cubic zirconias show that this approximation holds quite well, but further studies would be valuable.

The centre frequency of each mode was determined by a least-squares fitting procedure. The Brillouin line shapes are strictly Voigt functions. In the present analysis, the deconvolution became simple since the Brillouin lines were found to be Lorentzians. Similar conclusions were drawn by Abdul and Cummins (1985) on salol. The peak height, the full width at half-maximum and the centre frequency of each of the modes has to be estimated as input to the fitting program.

Since the intensities of the Brillouin peaks are related to the elasto-optic coefficients, the Rayleigh ratios have to be known for the scattering geometry. This was achieved by evaluating the Rayleigh ratio using Equation 2.21 for

The experiments were terminated at approximately 1400 K because of mechanical or electrical breakdowns and not due to lack of resolution. This emphasizes that the high purity quartz capsules with OH-content less than 0.5 ppm adopted in this project were improving the quality of the Brillouin spectra at high temperatures as compared with previous work using an inferior grade of quartz for this purpose.

Analysis of Brillouin spectra

Brillouin spectral analysis was done using the results of section 2.3. Because n_0 and n_e have very close values and using the conclusions of the previous Brillouin studies on light tysonite trifluorides (Laiho *et al.* 1983a, Ngoepe *et al.* 1986, Mjwara *et al.* 1991), the Brillouin frequency shifts in anisotropic media (Chandrasekharan 1965)

$$\Delta\nu_B = \frac{v_a\nu_0}{c}(n_o^2 + n_e^2 - 2n_0n_e\cos\theta)^{\frac{1}{2}} \tag{4.1}$$

can be written in a simpler form:

$$\Delta\nu_B = \frac{2nv_a}{\lambda_0}\sin\frac{\theta}{2}, \tag{4.2}$$

where n is the average of n_o and n_e.

The Brillouin shifts $\Delta\nu_B$ are related to the elastic constants or their combina-

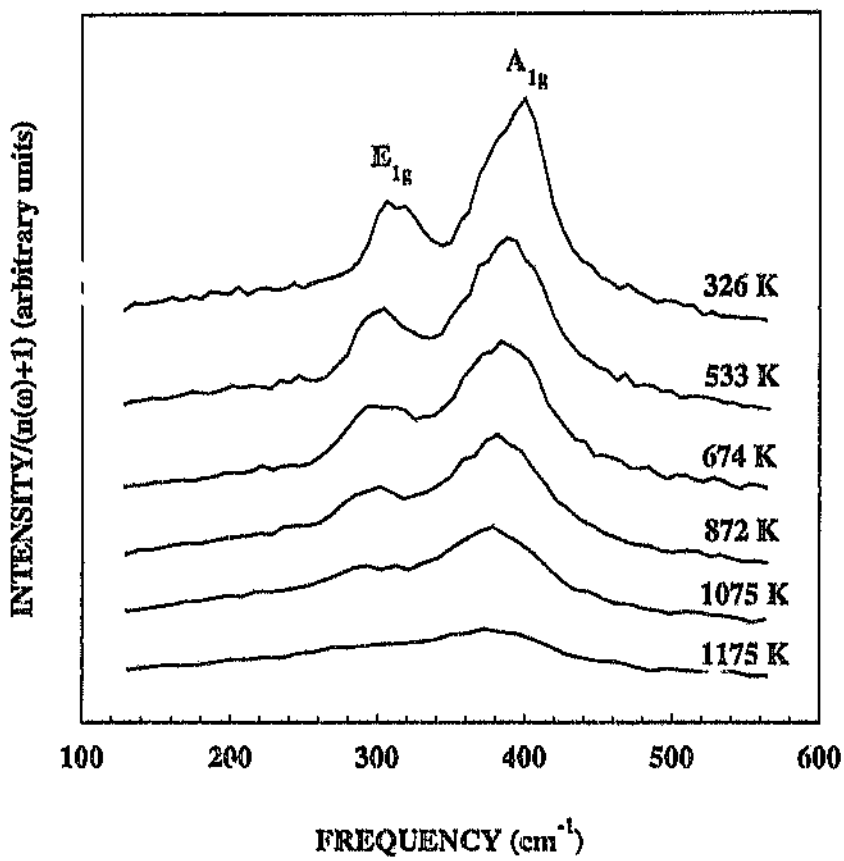

Figure 4.13: Raman spectra LaF_3(2.5 mol % BaF_2) at various temperatures corrected for thermal population effect by dividing the observed scattering intensity by $n(\omega,T)+1$, where $n(\omega,T)$ is the Bose-Einstein factor.

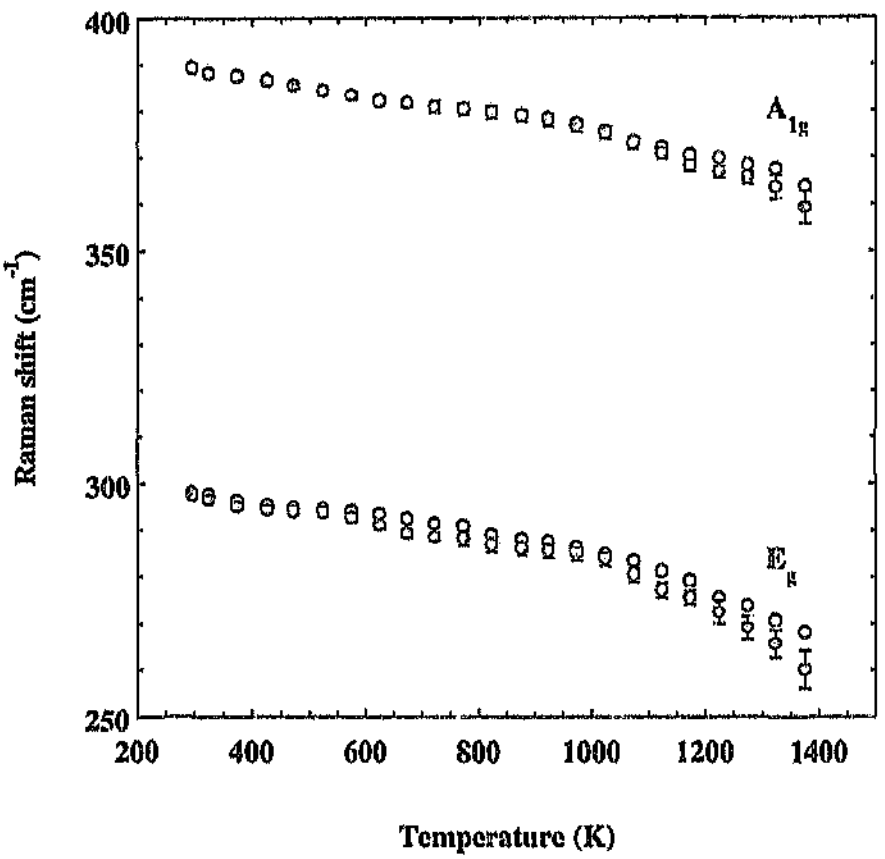

Figure 4.12: Temperature dependence of the E_g-mode and A_{1g}-mode band maxima in pure LaF_3. The circles are the maxima in the observed Raman intensities, while the solid circles denote frequency maxima of I_{red} according to Eq. 4.5.

Figure 4.12 shows that for pure LaF_3 a complex mechanism is involved. Since the presence of defects changes completely the analysis based on Equation 4.8, the damping and softening of modes for LaF_3 should be treated with extreme caution.

In order to examine the data above T_c, an alternative analysis can be used in which the temperature dependence of the bandwidth is written in the Arrhenius form:

$$\Gamma = A + B\exp(-\frac{E_a}{kT}), \tag{4.9}$$

The dynamic processes implied by this model are quite different to those described by the Klemens model. In this approach the bandwidth consists of a constant vibrational part A and a dynamical contribution described by the second term. Generally, the E_a corresponds to the activation energy necessary for the dynamic process involved. Rakov (1964) proposes this model in order to explain the extra broadening due to rotational motion of the sulfate ions in different anorganic complexes. Abdul and Cummins (1985) have used a similar approach in order to explain the extra broadening of the Brillouin peaks in salol. Following these models, E_a might be attributed to the activation energy. The fit to the data above T_c according to this model is also shown in Figure 4.11. The activation energy of pure LaF_3 was found to be 0.32 eV.

Typical Raman spectra for LaF_3 (2.5 % mol BaF_2) are presented in Figure 4.13. The same kind of changes in linewidth and frequency shift as for LaF_3 are noted for the doped crystal. The computer-fitted spectra are also shown in Figure 4.14.

the high temperature approximation the factors multiplying A and B vary as T and T^2, respectively. Using a least-squares fit for FWHM of pure LaF_3, the constants are found to be A=19.3 cm^{-1}, B=0.17 cm^{-1}, and γ_0=0, respectively.

Since the work of Liarokapis *et al.* 1985 reported values for A (13 cm^{-1}) and B (1.2 cm^{-1}) in the range 300-800 K, a fit of the same type in this range was performed on the present results for consistency and gave A=13.5 cm^{-1} and B=1.3 cm^{-1} corresponding closely with the results of this previous study.

At temperatures above 1150 K the Raman lines are broadened by an additional mechanism, which is temperature dependent and cannot be described by Klemens-Balkanski equation.

The use of I_{Red} defined as

$$I_{red} = \frac{\omega}{n(\omega)+1} I_{Ram} = \frac{A\omega^2\gamma(T)}{(\omega_0(T)^2-\omega^2)^2+\omega^2\gamma^2(T)}, \qquad (4.8)$$

was found useful in several studies of superionic conductors (Delaney and Ushiodo 1976, Habbal *et al.* 1978, Teeters and Frech 1982). It is easy to show that $dI_{red}/d\omega = 0$ for ω=0 and $\omega = \pm\omega_0$. Therefore, I_{red} is a maximum at frequency ω_0 regardless of the size of γ. On the other hand, a maximum in I_{Ram} is function of ω_0 and γ.

If a mode is overdamped the peak positions are different in I_{Ram} and I_{red} spectra. If only softening mechanism occurs, the same peak positions are found in both I_{Ram} and I_{red} spectra.

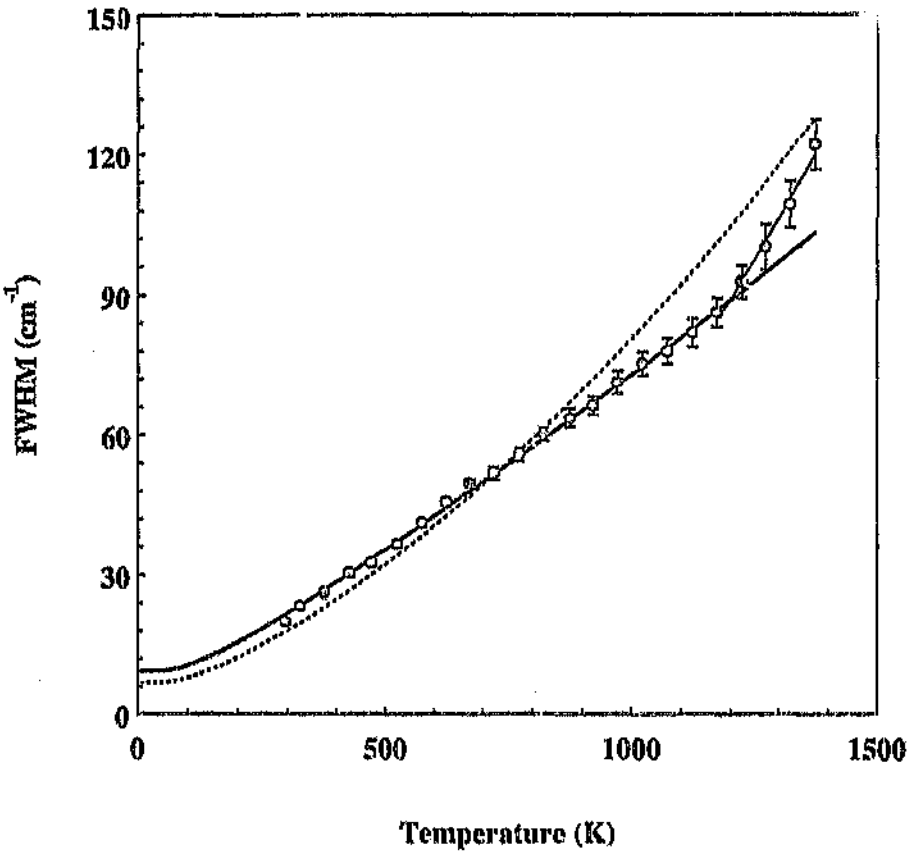

Figure 4.11: Linewidths of the 392 cm^{-1} phonon as a function of temperature for pure LaF_3. The thick solid line is the fit of the data using Klemens model of anharmonic decay; the thin line above 1150 K is another fit of the data using an Arrhenius model, and the dash line represents an extrapolated fit according to the experimental data of Lierokapis *et al.* 1985, which were measured over the temperature range 300 to 800 K.

discussed in Chapter 2. Equation 2.24 is a classical result of the thermal expansion and may be obtained by rewriting the Raman scattering tensor in terms of the one-phonon Green function.

Another possible way to analyse the defect contribution in doped fluorite crystals was suggested by van der Marel and den Hartog (1982). They calculated theoretically the difference between FWHMs in pure and doped cubic fluorites and found the following expression:

$$\Delta\Gamma = AT^2 exp(-\frac{E_a}{k_B T}), \tag{4.6}$$

where E_a is the defect activation energy. Due to the nature of the present Raman results for doped LaF_3 in which A_{1g} (392 cm^{-1}) and E_{2g} (366 cm^{-1}) modes overlapped, this formula could not be used for analysis.

The results for the FWHM are presented following the most frequently used models which appear in the literature and involve either anharmonic or defect contributions reflecting various theoretical approaches.

The variation in the FWHM with temperature is shown in Figure 4.11. Also shown in Figure 4.11 is the fit to the data (thin solid curve) given by Klemens-Balkanski equation, previously discussed in Chapter 2, namely

$$\gamma(T) = \gamma_0 + A(n_2 + 1) + B[(n_3 + 1)^2 + \frac{1}{12}]. \tag{4.7}$$

The best fit was obtained by taking into account only the points below T_c. In

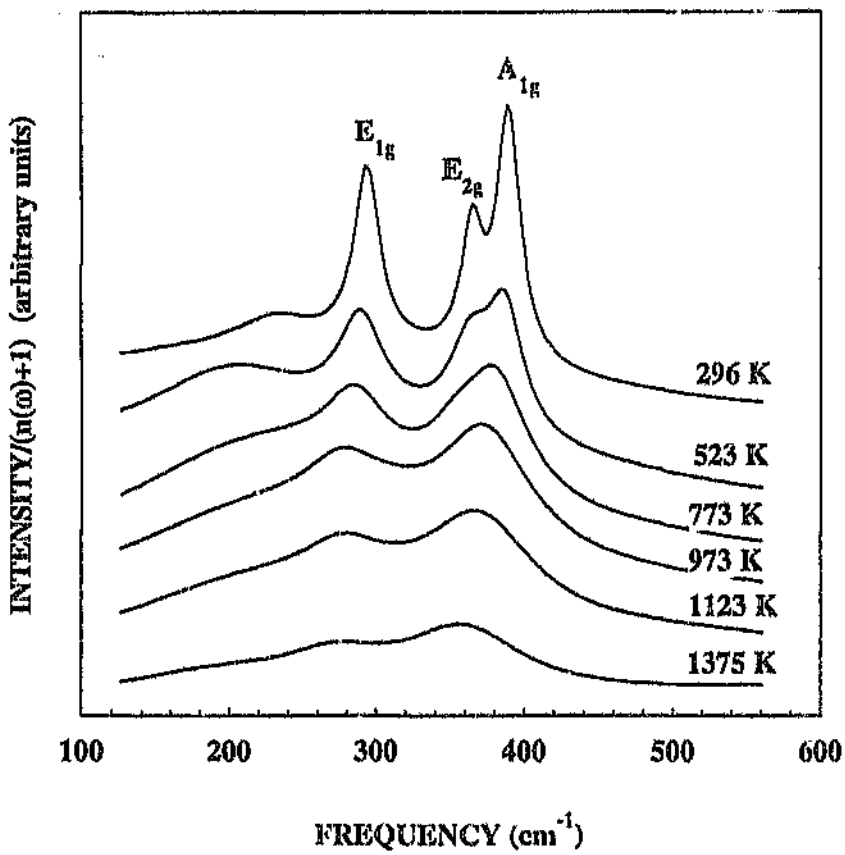

Figure 4.10: Simulated Raman spectra for pure LaF_3

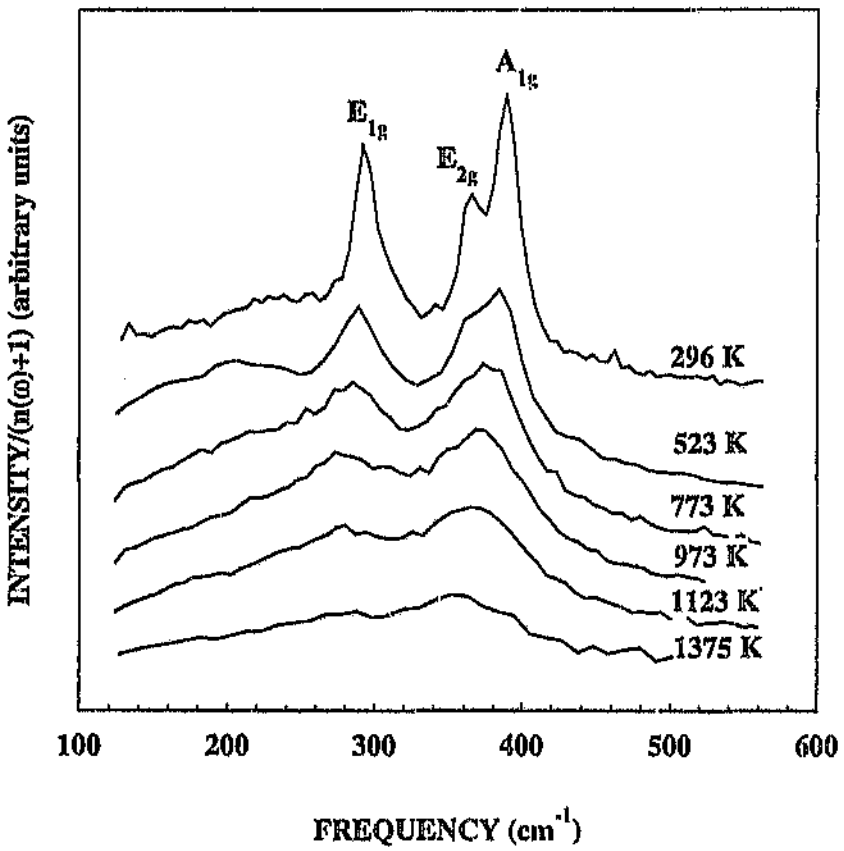

Figure 4.9: Raman spectra of pure LaF_3 at various temperatures corrected for thermal population effect by dividing the observed scattering intensity by $n(\omega,T)+1$, where $n(\omega,T)$ is the Bose-Einstein factor. Scattering geometry is $x(yy)x$.

For simplic ty of computation, the experimental peaks were computer-fitted with Lorentzians instead of the Voigt profiles since the signal to noise ratio and the relatively small Gaussian instrumental contribution were such as to make the distinction between Voigt and Lorentzian curves indeterminate. The FWHM so obtained was assumed to be equal to FWHM that one would find by fitting the experimental intensity with a Voigt profile. The thermal background at each temperature was added as a power function in order to resolve these spectra properly.

4.3.5 Results and discussion

Typical Raman spectra of pure LaF_3 at different temperatures are presented in Figures 4.9 to illustrate their characteristic features. The changes in linewidth and shift are clearly evident. The computer-fitted spectra are also shown in Figures 4.10.

Analysing the FWHM in the case of crystals in which partial disorder is present at high temperatures becomes a very elaborate task (Elliott *et al.* 1978). When only anharmonicity is involved, the Raman intensity is given by:

$$I_{Ram} = \frac{A(n(\omega)+1)\omega\gamma(T)}{(\omega_0^2(T)-\omega^2)^2+\omega^2\gamma^2(T)}, \tag{4.5}$$

where ω_0 is the harmonic frequency and γ is the damping constant.

Below T_C, γ can be properly analysed using Klemens-Balkanski model already

where A is a constant containing the selection rules and the Raman matrix elements, $n(\omega)$ is the Bose-Einstein occupation number and $S(\omega)$ is the spectral density function of the dielectric constant fluctuations at $K \simeq 0$. Relation 4.4 results from statistical averaging of fluctuations and holds regardless of the nature of the excitation causing scattering. Since the nature of the spectral density function $S(\omega)$ is relevant in this study and ultimately the nature of fluctuations, the Raman intensities presented in this work were divided by $(n(\omega)+1)$.

The true experimental peaks must be extracted from the convoluted spectrum measured experimentally. It is common in all spectroscopic studies that the observed spectrum is a convolution of the true spectrum, characteristic of the processes that take place in the system under study, in this case a Lorentzian, and the instrumental function arising from the finite slit width of the spectrometer. The instrumental function can well be approximated by a Gaussian when the resolution is limited by aberrations and diffractions of various optical components in the optical system. This kind of convoluted spectrum is known as a Voigt profile. A deviation of the observed spectrum from the true spectrum is small only when the full width at half maximum of the instrumental function is small compared with that of the true spectrum. This case is applied to this Raman study, 3.4 cm^{-1} being the spectrometer resolution with an observed minimum Raman width of 20 cm^{-1}. Knowing the spectral bandpass and the measured FWHM, it is possible to find the true FWHM for a Voigt profile using Posener's tables (1959). For this reason, small corrections for the finite resolution of the spectrometer were done before reporting FWHM.

at ambient temperature in order to test their quality for Raman spectroscopy. The surface quality of the LaF_3(5 mol % BaF_2) was poor after the previous Brillouin high temperature run, only LaF_3(2.5 mol % BaF_2) being found good enough for new high temperature measurements. This crystal was repolished and encapsulated again in order to minimize the effects of the previous run.

The background thermal radiation was the major limiting factor on Raman data accumulation at high temperatures; nevertheless the highest temperature reached for the pure LaF_3 crystal was 1400 K while 1200 K was attained for LaF_3 (2.5 mol % BaF_2).

Analysis of the Raman spectra

In this Raman study, the development of disorder is indicated by changes in the broadening of the E_g and A_{1g} modes and by changes of the Raman frequencies as will outlined below.

The first step in the analysis of a Raman spectrum was to establish the assignment of Raman peaks to their appropriate irreducible modes. Following the information already available in the literature (Bauman and Porto 1967, Cerdeira *et al.* 1979, Liarokapis *et al.* 1985) this first step was straightforward.

According to the fluctuation dissipation theorem (Landau and Lifshitz, 1980), the Stokes Raman spectrum can be written:

$$I_{Ram} = A(n(\omega) + 1)S(\omega) \qquad (4.4)$$

4.3.4 High temperature studies using Raman scattering

The features which were noted during the Raman high temperature runs are discussed in this section.

For each experiment performed, the furnace was aligned according to the procedure described previously. The Raman shift and broadening of the first order Raman E_g and A_{1g}- modes over the temperature range 300-1400 K were measured. In this experiment, only most energetic modes with a nominal frequency of 293 and 392 cm^{-1} could be observed and monitored; the weak modes could not be measured.

The Raman spectra were excited by the 488 nm laser line, a right-angle scattering geometry being used. A laser power of about 35 mW on the sample with a Jarrell Ash slit combination of $\approx 100/100/100\ \mu m$ was found appropriate to record the spectra with reasonably good signal to noise ratio. No polarizers were used for the data presented in this work.

Two samples were used for Raman measurements: pure LaF_3 and LaF_3 doped with 2.5 mol % BaF_2. The latter sample was previously used for Brillouin measurements. Due to an absence of any previous Raman measurements on doped LaF_3 it was considered important to measure all the doped crystals by means of Raman spectroscopy. However, owing to the unavailability of further doped crystal material, the crystals previously employed for Brillouin measurements were utilised. As a precaution, these doped crystals were examined

be bound to the extrinsic structures. If this work can be pursued successfully, then the present Brillouin and Raman results can supply valuable confirmation for these defect clusters. Therefore, computational simulations are required to further study and understand these experimental results.

Further theoretical work is necessary to be done in order to obtain a theoretical expression for Raman FWHM. The Green function formalism can be used to calculate the additional broadening due to disorder. This technique was used by Elliott *et al.* (1978) to explain the same effect in cubic fluorite crystals. This elaborate theoretical calculation has not been done yet for the tysonite crystals.

Extending the study to the whole tysonite family will provide a better insight into this class of compounds.

In conclusion, the present work has provided new and useful data on pure and doped superionic LaF_3. These data are in very good agreement with the previous studies on pure LaF_3. New very interesting features have been noted for doped LaF_3.

Further work suggested in this section may lead to a better understanding of the fast ion conductors with the tysonite structure.

5.2 Recommendations

The following suggestions for further work are intended to provide more clarity on the role of the various components of the combined Brillouin - Raman techniques.

The measurement of the all elastic constants for LaF_3 doped with 2.5 mol %, and 5 mol % BaF_2 should be undertaken. These experiments would provide a clear picture of the dependence of elastic constants on the temperature and concentration. Furthermore, a study of the influence of dopant cation size should provide valuable information, as was found in analogous experiments on the CaF_2 (ReF_3) systems; Re stands fore rare earth. Raman scattering studies on this kind of crystal should also be performed and correlated with the Brillouin measurements.

On the other hand, a complementary study of LaF_3 doped with tetravalent halides (e.g. ThF_4 or UF_4) will confirm if these dopants decrease the superionic properties of tysonite materials as reported by Roos *et al.* (1984c) and Takahashi *et al.* (1977).

Lattice parameter and refractive index measurements similar to those done on ZrO_2 (Botha *et al.* 1993) and YAG (Stoddart *et al.* 1993) will assist in obtaining the elastic constants instead of simply the acoustic mode frequencies.

Computational simulation studies might provide a cluster model, similar to those found for cubic crystals, in which thermally generated interstitials can

A comparison of the results of the doped and pure LaF_3 shows that there is a significant reduction in the transition temperatures T_c for all doped crystals.

The rate of change of the elastic constants in pure and doped LaF_3 above T_c and the activation energies obtained from the Raman measurements in the superionic range would suggest that the same defect conduction mechanism occurs in the superionic phase for pure and doped crystals.

A slight deviation from a quasi-linear decrease of the measured values of $\Delta(\nu_B)^2$ in the Brillouin experiments was noted for LaF_3 (2.5 mol % BaF_2) crystal below T_c, a classical behaviour for C_{11} being measured for LaF_3 (5 mol % BaF_2) crystal.

The elastic constants, as already seen at numerous places in the literature, have proved to be very sensitive to the change of phase transition temperature, as previously noted in the case of the fluorite compounds.

The fitting procedures employed have proved to be useful in the analysis of Brillouin and Raman experimental data.

A very important conclusion of the present study is that a small doping implies a decrease in superionic phase temperatures. A self-consistent explanation involves a co-operative generation of disorder on the fluorine sublattice(s). However motional effects of a limited number of defects could be responsible for these effects.

Chapter 5

Conclusions and recommendations

Since a detailed discussion has followed the presentation of results in Chapter 4, only some of the prominent features noted in the present study will be outlined. Finally suggestions will be made which might assist in further work.

5.1 Conclusions

The combined use of Brillouin and Raman techniques has provided a great deal of information about the structural disorder which developed in the high temperature superionic phase of pure and doped LaF_3. The present Raman study is the first one which covers the range of the phase transition.

Using the Rakov approach, similar values for activation energy are obtained above phase transition, 0.32 eV and 0.36 eV, respectively. This would suggest that the same kind of conduction mechanism is applying to pure and doped crystals in the superionic phase. The Rakov model provides values for activation energies similar to those obtained for migration energies of $\gamma \leftrightarrow \alpha'$ fluorine type motion at ambient temperature by Jordan and Catlow (1987).

The most important effect introduced by disorder in fluorides is that defects can lead to changes in both polarizabilities and Green function, whereas anharmonicity changes only the Green function. The change in the Green function arises from a change of the force constants to the neighbours. Polarizability is changed, because the electronic environment of the neighbours is changed, and hence their polarizability. The analysis of polarization is in itself a difficult task since short range (Hartley *et al.* 1971) or long range (Chase *et al.* 1973) descriptions can be assumed for modelling. In addition to this, interstitial and vacancy contributions are different in the Green function; therefore their calculations differ.

Light spectroscopy itself cannot distinguish between effects due to anharmonicity and defects. A possible way to obtain these separate contributions is to study only the effect of anharmonicity by elaborate quantum mechanics techniques and to compare these results with the experimental values of FWHM as was done for cubic fluorite crystals by Elliott *et al.* 1978. The defect contribution to FWHM can be also theoretically calculated using the same approach. No study of this kind for LaF_3 appears in the literature at the present moment.

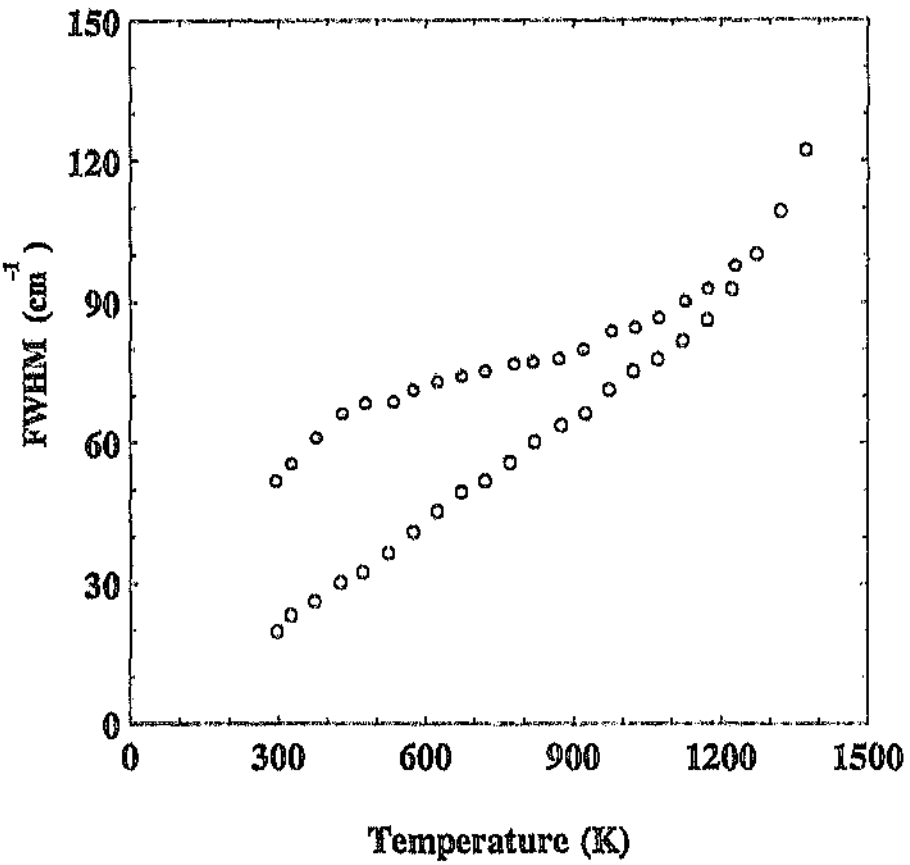

Figure 4.19: FWHM for A_{1g} modes in pure LaF_3 and LaF_3 (2.5 mol % BaF_2). The solid circles are FWHM for doped LaF_3, while the circles denote FWHM for pure LaF_3.

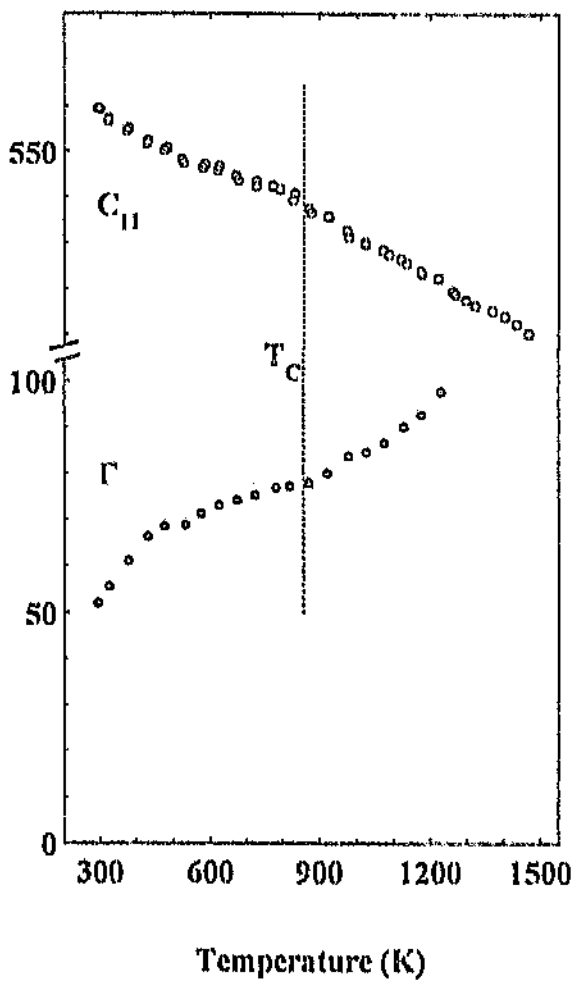

Figure 4.18: Results of Raman and Brillouin experiments for LaF_3 (2.5 mol % BaF_2)

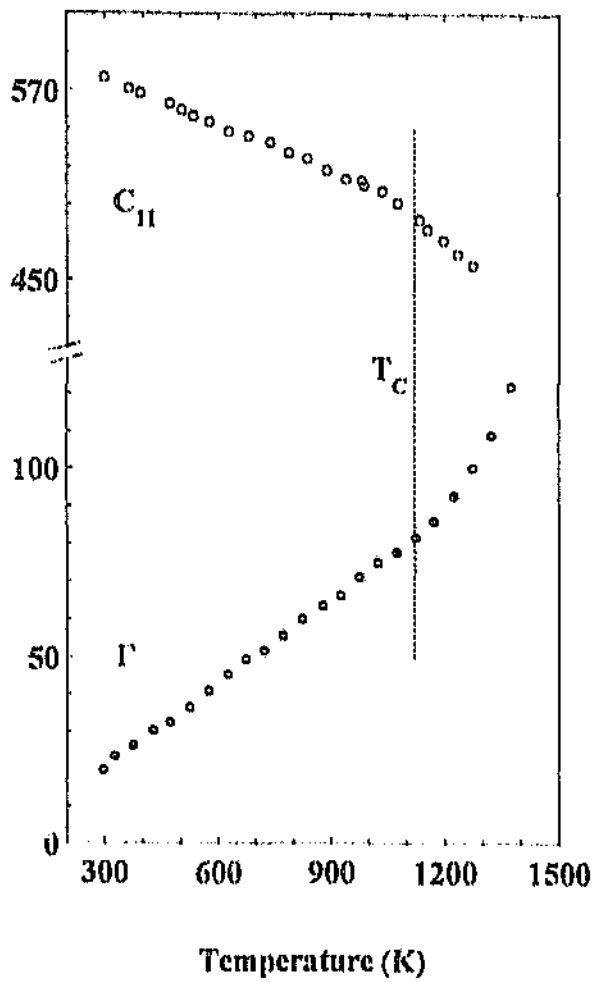

Figure 4.17: Results of Raman and Brillouin experiments for pure LaF_3

In the case of LaF_3 (2.5 mol % BaF_2), only the behaviour of A_{1g} (392 cm^{-1}) could be monitored, the errors in fitting the other two modes E_{1g} and E_{2g} being too large. Figure 4.15 shows the shift of A_{1g} mode with the temperature.

The variations in the FWHM for the A_{1g} mode in the case of doped LaF_3 is shown in Figure 4.16. Another type of behaviour is noted which cannot be described by Klemens-Balkanski equation. A fit based on the Arrhenius model above 860 K gave an activation energy of 0.36 eV.

4.3.6 Comparison of Brillouin and Raman results

The agreement between the temperature at which FWHM of the A_{1g} Raman mode starts to rise and the temperature at which substantial decrease in C_{11} elastic constant occurs is very good in the case of pure LaF_3 and LaF_3 doped with 2.5 mol % BaF_2. The combination of Raman and Brillouin techniques provides a straightforward method to determine T_c as it is shown in Figures 4.17 and 4.18. The information obtained from both techniques is complementary, the combined data providing a better evaluation of the phase transition temperature.

The abnormal slight curvatures which occurred in the behaviour of the elastic constant C_{11} and FWHM observed in LaF_3 (2.5 mol % BaF_2) compared to pure LaF_3 (Figures 4.7 and 4.19) corroborated with the behaviour of I_{red} Raman peaks would suggest that an additional contribution (very possibly a defect effect) appears to be starting from ambient temperature.

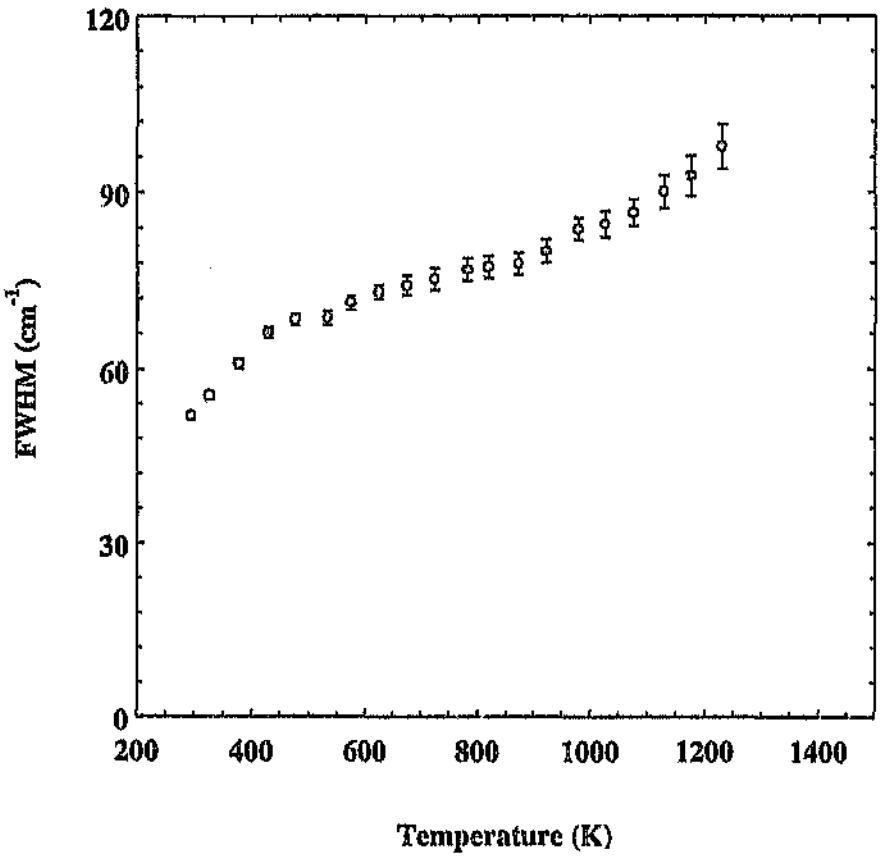

Figure 4.16: Linewidths of the 392 cm^{-1} phonon as a function of temperature for LaF_3 (2.5 mol % BaF_2).

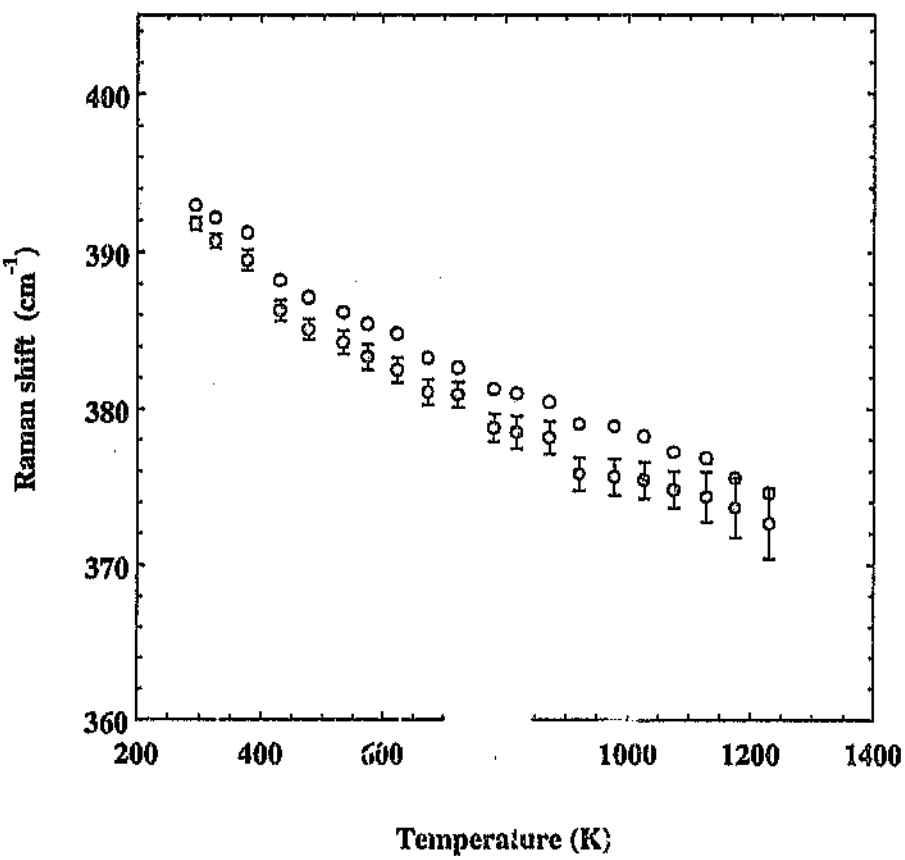

Figure 4.15: Temperature dependence of the A_{1g}-mode band maxima in LaF_3 (2.5 mol % BaF_2). The circles are the maxima in the observed Raman intensities, while the solid circles denote frequency maxima of I_{red} according to Eq. 4.5.

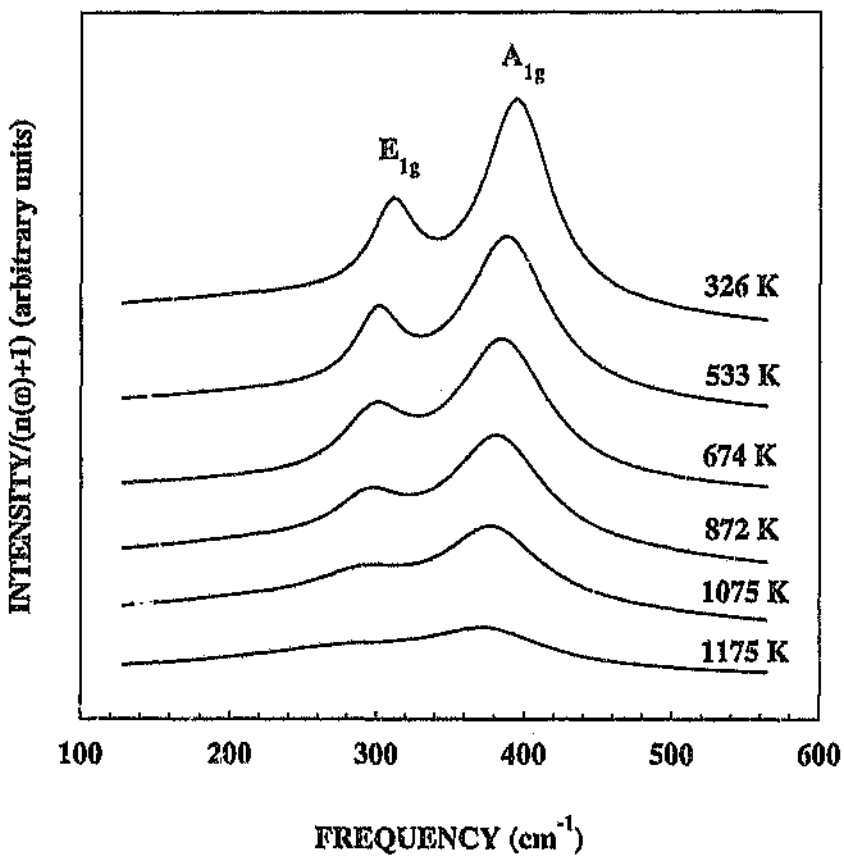

Figure 4.14: Simulated Raman spectra for LaF_3 (2.5 mol % BaF_2)

Stoddart P.R., Ngoepe P.E., Mjwara P.M., Comins J.D., and Saunders G.A. 1993, *J. Appl. Phys.* **73**, 7298.

Takahashi T., Iwahara H. and Ishihawa T. 1977, *J. Electrochem. Soc.* **124**, 280.

Takahashi T. 1989, *Superionic Solids and Solid Electrolytes: recent trends*, eds. Laskar A.L. and Chandra S., Elsevier, North Holland.

Teeters D. and Frech R. 1982, *Phys. Rev. B* **26**, 5897.

Temple P.A. and Hathaway C.E. 1973, *Phys. Rev. B* **7**, 3685.

Truell R., Elbaum C. and Chick B.B. 1969, *Ultrasonic Methods in Solid State Physics*, Academic Press, New York.

Vacher R. and Boyer L. 1972, *Phys. Rev. B* **6**, 639.

Vallean J.P. and Torrie G.M. 1977, *Modern Theoretical Chemistry, Equilibrium Statistical Mechanics of Fluids*, Vol. 5, ed. Berne B.J., Plenum, New York.

Vashishta P. and Rahman A. 1978, *Phys. Rev. Letters* **40**, 1337.

Vashishta P., Mundy J.N. and Shenoy G.K. 1979, *Fast ion transport in solids*, North Holland, Amsterdam.

Vineyard G.H. 1957, *J. Phys. Chem. Solids* **3**, 121.

Whittingham M.S. and Silbernagel B.G. 1977, *Solid Electrolytes: General Principles, Characterization, Materials, Applications*, eds. Hagenmuller P. and van Gool W., Academic Press, New York.

Williams J. and Lamb J. 1958, *J. Acoust. Soc. Am.* **30**, 308.

Wood W.W. and Erpenbeck J.J. 1976, *Ann. Rev. Phys. Chem.* **27**, 319.

Zalkin A., Templeton D.H. and Hopkins T.E. 1966, *Inorg. Chem.* **5**, 1466.

Richards P.M. 1979, *Physics of Superionic Conductors*, ed. Salomon M.B., Springer-Verlag, New York.

Roos A., Aalders A.F., Schoonman J., Arts A.F.M. and de Wijn H.W. 1983, *Solid State Ionics* **9&10**, 571.

Roos A., Franceschetti D.R. and Schoonman J. 1984a, *Solid State Ionics* **12**, 485.

Roos A., van de Pol F.C.M., Keins R. and Schoonman J. 1984b, *Solid State Ionics* **13**, 191.

Roos A. and Schoonman J. 1984c, *Solid State Ionics***13**, 205.

Sandercock J.R. 1971, *2nd Int. Conf. on Light Scattering in Solids*, ed. Balkanski M., Flammarion, Paris.

Sandercock J.R. 1975, *RCA Review* **36**, 89.

Sandercock J.R. 1976, *J. Phys. E* **9**, 566.

Sandercock J.R. 1982, *Light Scattering in Solids III, Recent Results*, eds. Cardona M. and Güntherodt G., Topics Appl. Phys.**51**, Springer-Verlag.

Sandercock J.R. 1994, *Operator manual for tandem interferometer.*

Sangster M.J.L. and Dixon M. 1976, *Adv. Phys.* **25**, 247.

Schoonman J., Overshuizen G., and Wapenaar D.E.D. 1980, *Solid State Ionics* **1**, 211.

Schroter W. and Nolting J. 1980, *J. Phys.* (Paris) **41**, C6-20.

Sher A., Solomon R., Lee K., and Muller M.W. 1966, *Phys. Rev.* **144**, 593.

Shuker R. and Gammon R.W. 1970, *Phys. Rev. Lett.* **25**, 222.

Spedding F.H., Beaudry B.J., Henderson D.C. and Moorman J. 1974, *J. Chem. Phys.* **60**, 1578.

Musgrave M.J.P. 1970, *Crystal Acoustics*, 288.

Ngoepe P.E., Comins J.D., and Every A.G. 1986, *Phys. Rev. B* **34**, 8153.

Ngoepe P.E. 1987, *PhD*, University of the Witwatersrand, unpublished.

Ngoepe P.E. and Comins J.D. 1988, *Phys. Rev. Letters* **61**, 978.

Ngoepe P.E., Jordan W.M., Catlow C.R.A., and Comins J.D. 1990, *Phys. Rev. B* **41**, 3815.

Nizzoli F. and Sandercock J.R. 1991, *Dynamical Properties of Solids*, eds. Horton G.R. and Maradudin A.A., Elsevier, Amsterdam.

Norgett M.J. 1974, UKAEA report, AERE-R7650.

Nye J.F. 1960, *Physical Properties of Crystals*, Oxford University Press.

Pardee W.J. and Mahan G.D. 1975, *J. Solid State Chem.* **15**, 310.

Pollard H.F. 1977, *Sound Waves in Solids*, Pion, London.

Posener D.W. 1959, *Aust. J. Phys.* **12**, 184.

Preuss E. 1979, *Compul. Phys. Commun.* **18**, 261.

Puls M.P. and Norgett M.J. 1976, *J. Appl. Phys.* **47**, 466.

Rahman C.V. 1928, *Ind. J. Phys.* **2**, 387.

Rahman A. 1964, *Phys. Rev. A* **136**, 405.

Rakov A.V. 1964, *Tr. Fiz. Ins Akad. Nauk SSSR* **27**, 111.

Rango C. de, Tsoucaris G. and Zawer C. 1966, *C.R. Acad. Sci. Paris C* **263**, 64.

Reissland J.A. 1973, *The Physics of Phonons*, Wiley, New York.

Rice M.J. and Roth W.L. 1972, *J. Solid State Chem.* **4**, 294.

Lidiard A.B. 1974, *Crystals with fluorite structure*, ed. Hayes W., Clarendon Press, Oxford.

Love A.E.H. 1944, *A Treatise on the Mathematical Theory of Elasticity*, Dover, New York.

Loudon R. 1964, *Advances in Phys.* **13**, 423.

Loudon R. 1965, *Advances in Phys.* **14**, 621.

Loudon R. 1973, *The quantum theory of light*, Clarendon Press, Oxford.

Mackrodt W.C. and Steward R.F. 1979, *J. Phys. C* **12**, 431.

Manasreh M.O. and Pederson D.O 1984, *Phys. Rev. B* **30**, 3482.

Manasreh M.O. and Pederson D.O 1985, *Phys. Rev. B* **31**, 3960.

Mansmann M. 1965, *Z. kristallogr.* **122**, 375.

Maradudin A.A. and Fein E.E. 1962, *Phys. Rev.* **128**, 2579.

van der Marel D. and den Hartog H.W. 1982, *Phys. Rev. B* **25**, 6602.

McSkimin H.J. 1961, *J. Acoust. Soc. Am.* **33**, 12.

Mead D.G. and Wilkinson G.R. 1977, *J. Phys. C* **10**, 1063.

Mendik M., Sathish S., Kulik A., Gremaud G., and Waenter P. 1992, *J. Appl. Phys.* **71**, 2830.

Metropolis N.A., Rosenbluth A.W., Rosenbluth M.N., Teller A.H., and Teller E. 1953, *J. Chem. Phys.* **21**, 1087.

Mjwara P.M., Comins J.D., Ngoepe P.E., and Chadwick A.V. 1991, *Radiation Effects and Defects in Solids*, Vol. 119-121, 237.

Mock R., Hillebrands B. and Sandercock R. 1987, *J. Phys. E* **20**, 656.

Mott N.F. and Littleton M.J. 1938, *Trans. Farad. Soc.* **34**, 485.

Hooper A. 1978, *Cont. Phys.* **19**, 147.

Hutchings M.T., Clausen K., Dickens M.H., Hayes W., Kjems J.K., Schnabel P.G. and Smith C. 1984, *J. Phys. C***17**, 3903.

Jacquinot P. 1960, *Rep. Prog. Phys.* **23**, 267.

Jordan W.M. and Catlow C.R.A. 1987, *Cryst. Latt. Def. and Amorph. Mat.* **15**, 81.

Jaroszkiewicz G.A. and Strange J.M. 1985, *J. Phys. C: Solid St. Phys.* **18**, 2331.

Keller O. and Sondergaard C. 1974, *Japan J. Appl. Phys.* **13**, 1765.

Kim Y.S. and Gordon R.G. 1974, *J. Chem. Phys.* **60**, 4332.

Klemens P.G. 1966, *Phys. Rev.* **148**, 845.

Krischer C. 1968, *Appl. Phys. Lett.* **13**, 310.

Kunc K., *Ann. Phys.* (Paris), **8**, 319.

Laiho R., Lakkisto M. and Levola T 1983a, *Phil. Mag. A.* **47**, 235.

Laiho R. and Lakkisto M. 1983b, *Phil. Mag. B.* **48**, 203.

Landau L.D. and Lifshitz E.M. 1960, *Theory of Elasticity*, Pergamon Press.

Landau L.D. and Lifshitz E.M. 1980, *Statistical Physics*, Pergamon Press.

LeClaire A.D. 1970, in *Treatise on Physical Chemistry*, Vol. 10, eds. Eyring H., Henderson D. and Jost W., Academic Press, New York.

Leslie M. 1983, *Solid State Ionics* **8**, 243.

Liarokapis E., Anastassakis E., and Kourouklis G.A. 1988, *Phys. Rev. B* **32**, 8346.

Lidiard A.B. 1957, *Handbuch der Physik*, Vol. 20, Springer-Verlag, Berlin.

Garber J.A. and Granato A.V. 1975, *Phys. Rev. B* **11**, 3990.

Gmelin Handbuch der Anorganischen Chemie 1976, Seltenerdelente, Teil C3. Sc, Y, La und Lanthanide, Springer, Berlin.

Goldman M. and Shen L. 1966, *Phys. Rev.* **144**, 321.

Gordon R.E. and Strange J.H. 1978, *J. Phys.* C11, 3213.

Gross E.F. 1930, *J. Physik* **63**, 685.

Hobbs F., Zvirgzd J.A., and J.F. Scott 1978, . *Chem. Phys.* **69**, 4984.

Hamermesh M. 1962, *Group theory and its application to physical problems*, Eddison-Wesley.

Harley R.T., Page J.B. and Walker C.T. 1971, *Phys. Rev. B***3**, 1365.

Harley R.T., Manning D.I., and Ryan J.F. 1978, *J. Phys. E* **11**, 517.

Haven Y. 1978, *Solid Electrolytes - General Principles, Characterization, Materials, Applications*, eds. Hagenmuller P. and W. Van Gool, Academic Press, New York.

Hayes W. 1978, *Contemp. Phys.* **19**, 469.

Hayes W. and Loudon R. 1978, *Scattering of light by crystals*, John Wiley & Sons.

Hayes W. 1982, *Light scattering in solids III: Recent results*, eds. Cardona M. and Güntherodt G., Springer-Verlag, Berlin.

Heine V. 1960, *Group Theory in Quantum mechanics, New York.*

Herzberg G. 1945, *Infrared and Raman Spectra*, New York.

Heyns A.M. and de Waal D. 1992, *J. Chem. Phys.* **97**, 8086.

Hogg R.D., Vernon S.P., and Jaccarino V. 1977, *Phys. Rev. Letters* **39**, 481.

Cheetham A.K., Fender B.E.F., Fuess H and Wright A.W. 1976, *Acta crystallogr. B* **32**, 94.

Chu B. 1974, *Laser Light Scattering*, Academic Press, New York.

Collin G. and Boilot J.P. 1989, *Superionic Solids and Solid Electrolytes: recent trends*, eds. Laskar A.L. and Chandra S., Elsevier, North Holland.

Comins J.D., Ngoepe P.E. and Catlow C.R.A. 1990, *J. Chem. Soc. Farad. Trans.* **86**, 1183.

Cowley R.A. 1965, *J. Phys.*(Paris) , Vol. 26, 659.

Cummins H.Z. 1969, *Proceedings of the International School of Physics "Enrico Fermi", Quantum Optics*, ed. Glauber R.J.

Cummins H.Z. and Schoen P.E. 1972, *Laser Handbook*, eds. Arecchi F.T. and Schulz-BuBois E.O., North-Holland, Amsterdam.

Delaney M.J. and Ushioda S. 1976, *Solid Stat. Comm.* **19**, 297.

Dick B.G. and Overhauser A.W. 1958, *Phys. Rev.* **112**, 90.

Dil J.G. 1982, *Rep. Prog. Phys.* **45**, 285.

Elliot R.J., Hayes W., Rushworth A.J. and Ryan J.F. 1978, *Proc. R. Soc. Lond. A*, 317.

Erpenbeck J.J. and Wood W.W. 1977, *Modern Theoretical Chemistry*, Vol. 5, *Equilibrium Statistical Mechanics of Fluids*, ed. Berne B.J., Plenum, New York.

Evarestov R.A., Leko A.V., Murin I.V., and Veryazov V.A. 1992, *Phys. Stat. Sol. B* **170**, 145.

Every A. G. 1980, *Phys. Rev. B* **22**, 1746.

Every A. G. 1994, *NDT&E International*, Vol. 27, 3.

Catlow C.R.A. and Norgett M.J. 1978, UKAEA report, AERE M-2763.

Catlow C.R.A. 1980, *J. Phys. (Paris)* **41**, C6-53.

Catlow C.R.A. and Mackrodt W.C. (eds.) 1982, *Computer Simulations on solids, Lectures Notes in Physics*, Vol. 166, Springer-Verlag, New York.

Catlow C.R.A. 1984, *Solid State Ionics* **12**, 67.

Catlow C.R.A., Chadwick A.V., Greaves G.N. and Moroney L.M. 1985, *Cryst. Latt. Def. and Amorph. Mat.* **12**, 193

Catlow C.R.A. 1989, *Superionic Solids and Solid Electrolytes: recent trends*, eds. Laskar A.L. and Chandra S., Elsevier, North Holland.

Catlow C.R.A. (ed.) 1994, *Defects and Disorder in Crystalline and Amorphous Solids*, NATO ASI Series, Vol. 418, Kluwer Academic Publishers.

Cerdeira F., Lemos V., and Katiyar R.S. 1979, *Phys. Rev. B* **19**, 5413.

Chadwick A.V. and Glyde H.R. 1977, *Rare gas Solids*, Vol. 2, eds. Klein M.L. and Venables J.A., Academic Press, New York.

Chadwick A.V., Hope D.S., Jaroszkiewicz G.A., and Strange J.H. 1979, *Fast ion transport in solids*, eds. Vashishta P., Mundy J.N. and Shenoy G.K., North Holland, Amsterdam, pp. 683.

Chadwick A.V. 1983, *Solid State Ionics* **8**, 209.

Chadwick A.V. 1994, *Defects and Disorder in Crystalline and Amorphous Solids*, ed. Catlow C.R.A., NATO ASI Series, Vol. 418, Kluwer Academic Publishers.

Chandra S. 1981, *Superionic Solids*, North-Holland, Amsterdam.

Chandrasekharan V. 1965, *J. Phys.(Paris)* **26**, 665.

Chase L.L., Kuhner D. and Bron W.E. 1973, *Phys. Rev. B7*, 3892.

Bibliography

Aalders A. F., Polman A., Arts A.F.M., and de Wyn H.W.1983, *Solid State Ionics* **9**, 539.

Abdul M. and Cummins H.Z. 1985, *J. Phys. Chem. Solids* **46**, 1037.

Agullo-Lopez F., Catlow C.R.A., Townsend P.D. 1988, *Point Defects in Materials*, Academic Press, London.

Aliev A.E., Fershtat L.N. and Khabibullaev P.K. 1984, *High Temp (USSR)* **22**, 381.

Balkanski M., Wallis R.F., and Haro E. 1983, *Phys. Rev. B* **28**, 1928.

Bauman R.P. and Porto S.P.S. 1967, *Phys. Rev.* **161**, 842.

Benedek G.B. and Fritsch K. 1966 , *Phys. Rev.* **149**, 647.

Birnbaum G. (editor) 1985, *Phenomena Induced by Intermolecular Interactions*, New York, Plenum.

Born M. and Huang K. 1962, *Dynamical theory of crystal lattices*, Oxford University Press, London.

Botha P.J., Chiang J.C.H., Comins J.D., Mjwara P.M., and Ngoepe P.E. 1993, *J. Appl. Phys.* **73**, 7268.

Boyce J.B. and Huberman B.A. 1979, *Phys. Rep.* **51**, 189.

Brillouin L. 1922, *Ann. de Phys.* **17**, 88.

Cardona M.(ed) 1975, *Light Scattering in Solids*, Springer-Verlag.

Catlow C.R.A., Norgett M.J., and Ross T.A. 1977, *J. Phys. C* **10**, 1677.

Catlow C.R.A., Comins J.D., Germano F.A., Hartley R.T., and Hayes W. 1978, *J. Phys. C* **11**, 3197.

Author: Anghel Catalin Anton Marion.
Name of thesis: Light scattering by superionic LaF3 and LaF3(BaF2) compounds.

PUBLISHER:
University of the Witwatersrand, Johannesburg
©2015

LEGALNOTICES:

Copyright Notice: All materials on the University of the Witwatersrand, Johannesburg Library website are protected by South African copyright law and may not be distributed, transmitted, displayed or otherwise published in any format, without the prior written permission of the copyright owner.

Disclaimer and Terms of Use: Provided that you maintain all copyright and other notices contained therein, you may download material (one machine readable copy and one print copy per page)for your personal and/or educational non-commercial use only.

The University of the Witwatersrand, Johannesburg, is not responsible for any errors or omissions and excludes any and all liability for any errors in or omissions from the information on the Library website.